University of California
Santa Barbara

Hierarchical crystallographic transformations and thermodynamic and kinetic analysis of spinel electrode materials

A dissertation submitted in partial satisfaction
of the requirements for the degree

Doctor of Philosophy
in
Materials

by

Sanjeev Krishna Kolli

Committee in charge:

Professor Anton Van der Ven, Chair
Professor Chris Van de Walle
Professor Glenn Frederickson
Professor John Harter

June 2021

The Dissertation of Sanjeev Krishna Kolli is approved.

Professor Chris Van de Walle

Professor Glenn Frederickson

Professor John Harter

Professor Anton Van der Ven, Committee Chair

May 2021

Hierarchical crystallographic transformations and thermodynamic and kinetic analysis of spinel electrode materials

by

Sanjeev Krishna Kolli

Acknowledgements

The author would like to thank all members of the Van der Ven research group for their advice, input, and camaraderie throughout the years. The author would also like to thank all funding sources (listed in each relevant chapter) for their financial support.

Curriculum Vitæ

Sanjeev Krishna Kolli

Education

2016-2021	Ph.D. in Materials (Expected), University of California, Santa Barbara.
2012-2016	B.S. in Materials Science and Engineering, Cornell University.

Publications

2020	Kolli, S. K., Natarajan, A. R., Thomas, J. C., Pollock, T. M., & Van der Ven, A. (2020). Discovering hierarchies among intermetallic crystal structures. Physical Review Materials, 4(11). https://doi.org/10.1103/physrevmaterials.4.113604
2018	Kolli, S. K., & Van der Ven, A. (2018). Controlling the Electrochemical Properties of Spinel Intercalation Compounds. ACS Applied Energy Materials, 1(12), 6833–6839. https://doi.org/10.1021/acsaem.8b01080
2018	Kolli, S. K., & Van der Ven, A. (2018b). First-Principles Study of Spinel MgTiS2 as a Cathode Material. Chemistry of Materials, 30(7), 2436–2442. https://doi.org/10.1021/acs.chemmater.8b00552

Abstract

Hierarchical crystallographic transformations and thermodynamic and kinetic analysis of spinel electrode materials

by

Sanjeev Krishna Kolli

Modern engineering applications use alloys with up to 10 different elements to meet performance requirements. Designing new alloys in such a vast multicomponent space is difficult. Even with first-principles methods to expedite the quest for new alloys, improvements to materials search algorithms are required to fully sift through the multidimensional chemical space. One possible search strategy is to exploit the natural hierarchy between crystal structures. Many crystal structures are related to a high symmetry parent crystal structure via a group/subgroup symmetry relationship. While many ordered structures are traditionally viewed as distinct crystals, they can be thought of as derivative structures of a parent crystal. The first half of this dissertation describes a framework for alloy design that is based on a parent-derivative crystal structure hierarchy. Chemical trends in this hierarchy are illuminated and new structural transformation pathways between important parent crystals are described.

The second half of this dissertation uses a similar philosophy to explore a different set of materials; it examines the effects of chemical trends on the electrochemical properties of materials used for energy storage. To meet rising energy demands with intermittent renewable energy sources such as solar and wind power, society needs to create high performance secondary batteries for energy storage. Li-ion batteries have quickly risen to be a prime candidate to meet energy storage needs, and new advances are being made to promote sustainable earth-abundant materials, higher charge rates, and larger

capacities. Some of these new advances include the investigation of Na-ion and Mg-ion batteries. Spinel intercalation compounds are well-known to facilitate high rate and high voltage Li-ion batteries, but less is known about their Na-ion and Mg-ion counterparts. When exploring new materials, it helps to have a strong fundamental understanding of how changes in chemistry or structure affect electrochemical performance of battery materials. This dissertation uses a combination of electronic structure calculations and statistical mechanics methods to study the thermodynamic and kinetic properties of a wide range of spinel intercalation compounds.

The identification of a crystal structure hierarchy was achieved by analyzing existing crystal structure databases using a crystallographic mapping algorithm to find representative parent crystal structures from which many derivative structures are formed. We found that 73% of binary intermetallic compounds found on the ICSD to be derived from only 20 unique parent crystal structures. There are important crystallographical relationships, such as the Bain path and the Burgers path, that connect parent crystals within our hierarchy. These crystallographic relationships facilitate structural phase transformations which are important for shape-memory alloys, magnetocalorics, or self-assembling block co-polymers. A crystal structure mapping algorithm was used to show the existence of 7 new structural transformation pathways between orderings on simple parent crystal structures to others belonging to the top 20 most common parent crystal structures. We use high-throughput density functional theory (DFT) to probe which elemental combinations are most likely to cause spontaneous structural transformations without an energy barrier. We find multiple chemical combinations that lead to barrierless transformation pathways. These barrierless transformations suggest a nucleation mechanism that does not require large structural fluctuations that are often energetically costly.

In our investigation of electrochemical properties of energy storage materials, we

examine the spinel structure which has a general formula AMX_2 where A is a guest cation, M is a transition metal and X is a chalcogenide. The electrochemical properties of spinel can be affected by many factors including (i) ionicity of the MX_2 framework, (ii) guest cation radius, and (iii) guest cation oxidation state. We conducted a systematic study and determined that guest cation radius and MX_2 ionicity play a significant role in guest cation site preference which, in turn, affects the electrochemical properties of spinel. The insights of this study suggest that large cations in an oxide spinel creates a desirable energy landscape for high-rate capable batteries. Using kinetic Monte Carlo simulations and a model cluster expansion Hamiltonian, we identify a topological pitfall that makes spinel prone to highly correlated cation diffusion at intermediate to high guest cation concentrations. This undesirable property is dependent on the strength of the nearest-neighbor repulsion of diffusing cations within spinel. A strong repulsion results in a dependence on large vacancy clusters to mediate diffusion. This dependence indicates that a percolating network of large vacancy clusters is necessary to facilitate long range diffusion. Our results show that the detrimental effects can be mitigated by reducing the strength of the repulsion or increasing the connectivity of the percolating network. Although our focus is on the fully-ordered spinel structure, the conclusions drawn from this study apply to other close-packed anion hosts such as disordered rocksalt electrodes and partially ordered spinels.

Contents

Chapter 1

Introduction

1.1 Crystallographic intuition

Technological revolutions have been marked by the materials that cause them to arise (e.g. stone, bronze, iron, and silicon age) [1]. As each new technology enhances our ability to discover more and push our limits of exploration further, it also increases the desire for even more advanced technology. Large companies are quickly showing that frequent space travel doesn't seem centuries or millenia away anymore. The ability to fly anywhere in the world is possible and the cost is only getting cheaper. In order for these technologies to push their limits, new materials that can withstand higher temperatures, extreme environments, large stress loads, and remain lightweight need to be discovered. The materials that have been discovered thus far are largely in existence due to thorough experimental studies. The composition space of these complex alloys is already quite large often containing various amounts of 10 different elements. In order to expedite the exploration of this vast space of alloy, we need to leverage the power of today's computational methods and data mining techniques to revisit the fundamental reasons for what makes an alloy have desirable properties. Examining existing databases

of compiled crystallographic data like the Inorganic Crystal Structure Database (ICSD) [2], the Materials Project [3], and the Pearson's Crystal Data (PCD), is an important step in leveraging computational power for materials research. We can use these databases to draw connections between the works of many past researchers that would normally be difficult or impossible to do with out the assistance of a computer. Classifying and organizing these connections between past works helps distill a vast pool of information into a more manageable list of fundamental concepts. Future researchers with a strong set of fundamental crystallographic knowledge can make organized attempts to design new materials with the backing of thousands of past works distilled down into a concentrated tool set. With the help of high performance computing and fundamentals, the navigation of a vast composition space where the combinatorics seems functionally infinite, doesn't seem so daunting. In this thesis, we describe a framework that helps distill large crystallographic databases into the most important structures and how those structures are related to each other. This framework will help fuel organized high throughput density functional theory calculations to enhance the predictive component of alloy design.

1.2 The importance of electrochemical storage

A switch from fossil fuels to renewable energy sources such as wind and solar power is a widely accepted solution to combat the concern of human induced climate change [4]. In order for intermittent power sources like solar and wind to meet energy demands at all hours of the day, they must be coupled with robust energy storage technology. Rechargeable Li-ion batteries are the largest growing technology that addresses the energy storage problem. Li-ion batteries are used across all levels of energy storage from personal electronics to hybrid and fully electric vehicles [5]. The dominant Li-ion battery technology is driven by a layered transition metal oxide containing nickel, manganese,

and cobalt, aptly named NMC cathodes [6]. As the electric vehicle market explodes in the next decade, demand for lithium and cobalt in the global market will rise to insatiable levels. Anticipating this, a large research effort has been put forth to finding alternate cathode chemistries to create energy dense batteries from more sustainable elements. Disordered rocksalt (DRX) based cathodes are a 3D alternative to traditional layered transition metal cathodes [7].

DRX cathode materials are promising because they are stabilized by the same principle that is thought to be most detrimental to layered transition metal cathodes, cation site disorder [8]. In layered transition metal cathodes, as the lithium is added and removed from the structure, it is often the case that the transition metals migrate to the sites that lithium occupied within the structure. This site swapping results in structural transformations causing an irreversible capacity loss. In DRX cathodes, site disorder is present from synthesis and charging cycles do not change the amount of disorder. It is also the case that there is minimal volume change upon cycling of DRX cathodes compared to layered cathodes, which is seen as beneficial for battery longevity. Recent work has shown the presence of high rate capability DRX electrodes allowing for the production of ultra-fast charging batteries [9, 10, 11]. Due to DRX materials only recently becoming popular as potential replacements for traditional layered transition metal oxides, they have yet to be optimized to commercial standards [12]. Researchers would strongly benefit from a thorough fundamental understanding of thermodynamic and kinetic properties of these materials while optimizing these chemistries to become commercially viable. First-principles analyses often expedite the fundamental understanding of what aspects of cathode materials govern their electrochemical properties. The disordered nature of DRX materials makes it inherently difficult to study using first-principles techniques due to the large configurational space. Luckily, the spinel structure is an ordered subspace in DRX based materials that has been more widely studied. As a

first step into studying the governing principles of the electrochemical properties of DRX materials, in this thesis we perform thorough thermodynamic and kinetic analysis on a wide range of potential spinel based cathodes using first-principles techniques. This work lays the foundation of understanding for DRX materials by explaining key fundamental insights of the analogous spinel intercalation compounds.

Chapter 2

Computational Methods

This chapter focuses on techniques that are essential to produce the results discussed is subsequent chapters. The methods include a description of density functional theory, cluster expansion methods, fitting procedures, and Monte Carlo methods. These four things together allow thermodynamic and kinetic property prediction at non-zero temperatures. The output of these methods are employed in Chapters 5-6 to study intercalation behavior of cathode materials. There is an additional section of this chapter that describes the details of a crystal mapping algorithm that is particularly helpful for comparing crystal structures. These methods along with density functional theory are used in Chapters 3 and 4 to group crystal structures by similarity.

2.1 Density Functional Theory

The energy of the quantum state of a material is essential for any analysis from first principles. The energy of the quantum state is given most rigorously by the Schrodinger equation. Solving the Schrodinger equation analytically for a multi electron system is impossible, due to electron-electron interaction terms. Since the 1960s, the approach to

approximating the solution to the Schrodinger equation for generic materials systems has been the use of density functional theory which transforms the problem to solve the energy of the system as a function of the electron density in the material. The energy contributions in density functional theory can be distilled into four categories: kinetic energy of the electrons, the effect of the nucleic potential on the electrons in the system, the Hartree energy (Coulombic effects between electrons) and the exchange-correlation energy. The approximation of the exchange-correlation term is what largely allows modern computers to perform first-principles calculations on materials. There are a growing number of ways to make these approximation, but in this thesis we use a pseudopotential based approximation. The calculations in this thesis use density functional theory as implemented in the Vienna Ab-initio Software Package (VASP) [13, 14] using projector augmented wave (PAW) theory as defined by Perdew-Burke-Ernzerhof (PBE) [15, 16]. No additional corrections to the energies were added to those obtained from VASP.

2.2 Cluster Expansion Methods

While DFT calculations can determine the formation energy of a given alloy composition quite accurately, they are quite slow for configurations with 100 atoms and prohibitively long for configurations with 1000-10000 atoms. For prediction of finite temperature thermodynamic and kinetic quantities, Monte Carlo methods described in the following section require rapid evaluation of formation energies of thousands of configurations with 1000-30000 atoms. A cluster expansion model can evaluate the formation energy of a large configuration (30000 atoms) in fractions of a second. The cluster expansion method constructs an effective Hamiltonian from the allowed degrees of freedom on a crystalline lattice. Degrees of freedom can include occupational, strain, displacement, magnetic, and orbital degrees of freedom. In this work, all cluster expansions only

include occupational degrees of freedom in a binary alloy. This indicates the energy of the system is solely based on the arrangement of atoms on a crystalline lattice. If atomic displacements are not large, atoms do not stray far from an identified site within the crystal; we define our cluster expansion Hamiltonian based on the occupants of these ideal crystal sites.

In order to construct an expression for the cluster expansion Hamiltonian, each crystal site, i, must be assigned a variable, σ_i, that represents the occupant of that site. The value assigned to σ_i is 0 if the site is vacant or 1 if the site contains atom A (typically Li^+, Na^+, or Mg^{2+} in this work). The configurational state of the crystal can be represented by a collection of all σ_i i.e. $\vec{\sigma} = \{\sigma_1, \sigma_2, ..., \sigma_N\}$ in a crystal with N atoms [17, 18].

We can then build clusters by collecting various amounts of nearby sites in the crystal. A point, pair, triplet, and quadruplet cluster has 1, 2, 3, and 4 crystal sites respectively. A cluster basis function, ϕ_α that represents the occupation of a given cluster,α, can be constructed by taking the product of all the site occupation variables, σ_i, in the cluster, α. This is formally written as:

$$\phi_\alpha(\vec{\sigma}) = \prod_{i \in \alpha} \sigma_i \tag{2.1}$$

If cluster basis functions are constructed using this method, they form a complete orthonormal basis. All composition dependent properties of these crystal can be written as a linear combination of this orthonormal basis, including the energy, as follows:

$$E(\vec{\sigma}) = \sum_\alpha V_\alpha \phi_\alpha(\vec{\sigma}) \tag{2.2}$$

The V_α are called effective cluster interactions (ECIs) and represent a weighted contribution to the energy for each cluster of sites. Ideally, Equation (2.2) sums over clusters of all shapes and sizes, but, in practice, the amount of ECIs used to approximate the energy must be truncated. This often means discarding clusters that have sites that are

far from each other or contain more than 4 sites. For most systems, this truncation is accurate as simple local interactions tend to dominate energy contributions to a system.

2.2.1 Fitting the coefficients of the cluster expansion

The assignment of cluster expansion coefficients, V_α, is a standard regression problem. The coefficients can be assigned by finding the best solution to the approximate matrix equation

$$\vec{E} = \vec{\vec{\Phi}}\vec{v} \tag{2.3}$$

where $\vec{E}$ is the set of energies for the various configurations used as training data, $\vec{\vec{\Phi}}$ is the correlation matrix (each row is the value of all basis functions,ϕ_α, for each configuration in the training data) and $\vec{v}$ is the set of fitting coefficients or ECIs, V_α. It is expected that the solution $\vec{v}$ is sparse and underdetermined. There are selection protocols to mitigate the number of non-zero ECI used in the resulting cluster expansion Hamiltonian. Some methods include LASSO regression (L1 regularization), ridge regression (L2 regularization), recursive feature elimination (RFE), and the genetic algorithm. Informing the regularization and priors to the fitting procedures can ensure that the cluster expansion model accurately matches the physics of the alloy system. This prior information includes giving low-energy configurations and ground states a higher weight during error calculation to ensure the most important configurations are predicted most accurately.

2.3 Monte Carlo Methods

At its core, thermodynamics is a statistical science. This means any thermodynamic quantity of a system can be determined by taking a statistical average of all of the possible

arrangements the system could adopt. Each of these arrangements is called a microstate. The system is constantly fluctuating between accessible microstates at finite temperature. The accessibility of each microstate, σ is determined by its energy, $\Omega(\sigma)$. The definition of $\Omega(\sigma)$ depends on the fixed (controlled) variables of the system. For example in the Grand Canonical ensemble where the fixed quantities are chemical potential, volume, and temperature, $\Omega(\sigma) = E(\sigma) - \sum_i \mu_i N_i$ If each microstate σ has a given probability $P(\sigma)$ and value for the property of interest $X(\sigma)$ the ensemble average of the property over all microstates can be calculated by

$$X = \sum_{\sigma} X(\sigma) P(\sigma) \tag{2.4}$$

The probability of a thermodynamic microstate, $P(\sigma)$,is determined by:

$$P(\sigma) = \frac{1}{Z} e^{-\Omega(\sigma)/k_B T} \tag{2.5}$$

where k_B is the Boltzmann constant, T is the temperature, and Z is the distribution of microstates also known as the partition function defined below.

$$Z = \sum_{\sigma} e^{-\Omega(\sigma)/k_B T} \tag{2.6}$$

The exact calculation of the partition function becomes intractable very quickly which is why we employ Monte Carlo methods to sample microstates from the distribution instead. Each microstate is sampled with the probability it would have from the probability distribution according to the Boltzmann distribution that governs the system. Over time, the Monte Carlo averaged property matches the averaging from the full partition function. The statistical sampling is driven by a Metropolis selection method that compares the energy of the transition from one microstate, σ_1, to another, σ_2. If $\Delta\Omega^{1\to 2} < 0$, the second

microstate is adopted with $P^{1\to2} = 1$. Otherwise the second microstate is adopted with a Boltzmann probability of:

$$P^{1\to2} = e^{-\Delta\Omega^{1\to2}/k_BT} \tag{2.7}$$

Most thermodynamic quantities can be sampled from the evolving Monte Carlo system with the exception of the entropy, S. To determine the entropy and quantities dependent on S like the Grand Canonical free energy, Φ, we must employ integration techniques.

2.3.1 Integration of the Gibbs free energy

The Grand Canonical free energy is defined by:

$$\Phi = G - \sum_i \mu_i N_i = E - TS + PV - \sum_i \mu_i N_i \tag{2.8}$$

$$d\Phi = -SdT - \sum_i N_i d\mu_i \tag{2.9}$$

With this definition and the substitution of $\beta = 1/k_BT$ we can examine the quantity $d(\beta\Phi)$ to see two ways to integrate the Grand Canonical free energy.

$$d(\beta\Phi) = Ed\beta - \sum_i \mu_i N_i d\beta - \beta \sum_i N_i d\mu_i \tag{2.10}$$

If we fix temperature ($d\beta = dT = 0$) the integration is over the chemical potential and simplifies Equation (2.10) to:

$$\int_I^F d\beta\Phi = \int_I^F \beta \sum_i N_i d\mu_i \tag{2.11}$$

$$\beta(\Phi^F - \Phi^I) = -\int_{\mu^I}^{\mu^F} \beta \sum_i N_i d\mu_i \tag{2.12}$$

$$(\Phi^F - \Phi^I) = -\int_{\mu^I}^{\mu^F} \sum_i N_i d\mu_i \tag{2.13}$$

If we fix chemical potential the integration is over temperature

$$\int_I^F d\beta\Phi = \int_{\beta^I}^{\beta^F} E d\beta - \sum_i \mu_i N_i d\beta = \int_{\beta^I}^{\beta^F} (E - \sum_i \mu_i N_i) d\beta \tag{2.14}$$

$$\beta^F\Phi^F - \beta^I\Phi^I = \int_{\beta^I}^{\beta^F} \Omega d\beta \tag{2.15}$$

$$\Phi^F = \frac{1}{\beta^F}(\int_{\beta^I}^{\beta^F} \Omega d\beta + \beta^I\Phi^I) \tag{2.16}$$

Both of these simplified formulas require an intial value for the grand canonical free energy Φ^I. These initial values can be determined at very low entropic states such as extreme values of chemical potential or very low temperatures where $\Phi \approx \Omega$. Once integrated, the Grand Canonical free energy can be used to help determine the chemical potential and composition at the edges of two-phase regions for accurate voltage curve construction.

2.3.2 Kinetic Monte Carlo

Macroscopic kinetic quantities can be determined using Monte Carlo methods as well. This can be done by tracking atomic trajectories through a simulation cell while recording the amount of time it takes for these trajectories to run their course. Atoms move through the simulation cell by vacancy-atom exchanges that happen at various frequencies. The

frequency, Γ, of a given vacancy-atom exchange (diffusion event) is determined by the following formula:

$$\Gamma = \nu^* e^{\Delta E_b / k_B T} \tag{2.17}$$

The frequency has an Arrhenius relationship with the energy barrier between an initial and a final state of the diffusion event, ΔE_b. ν^* is a vibrational prefactor determined by Vineyard's formula.

In spinel intercalation compounds, diffusion occurs between octahedral and tetrahedral sites. Both sites are local minima in the energy landscape for guest cations. Energy barriers typically look like the one shown in Figure 2.1.

The exact height of the energy barrier depends on the local arrangement of atoms around the moving atom and the modulation of the global chemical ordering caused by the diffusion event. The height of the barrier can be predicted using local cluster expansion methods similar to the methods described in Section 2.2.

The transition from one Monte Carlo step to the next is determined by a rejection-free kinetic Monte Carlo selection process. This process is carried out by calculating the frequencies of all possible diffusion events and creating a selection pool of events. An event, i, is selected with probability, P_i, according to

$$P_i = \frac{\Gamma_i}{\sum_j \Gamma_j} \tag{2.18}$$

where j sums over all the possible events from the starting configuration. An event is picked using a random number on the unit distribution. This event is applied to the starting configuration and tracked quantities, e.g. atomic trajectories, potential new events, and barrier heights, are updated. The amount of time elapsed for the event to

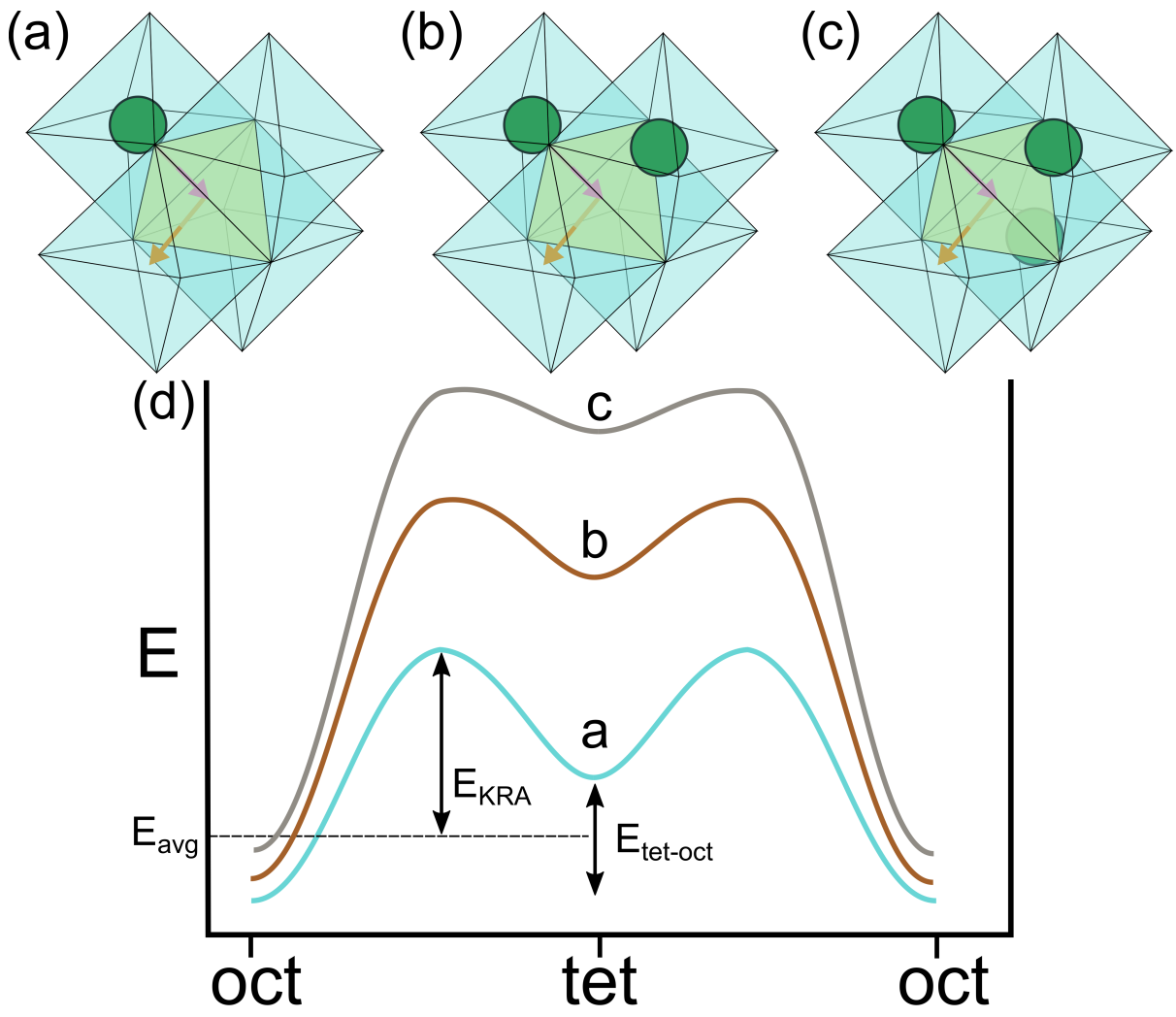

Figure 2.1: The diffusion path for a cation on an octahedral site via a (a) triple vacancy, (b) divacancy, and (c) single vacancy mechanism. (d) Hypothetical energy landscapes for these diffusion mechanisms. The ion first moves to the tetrahedral site via the magenta arrow.

have occurred is then calculated via the following formula:

$$\Delta t = \frac{\ln(1/u)}{\sum_j \Gamma_j} \tag{2.19}$$

where u is the random number chosen on the unit distribution. Once all updates are complete, the process is repeated. As more events are selected, the atomic trajectories grow larger. After a significant amount of events, kinetic properties such as Onsager coefficients, self diffusion coefficients, and correlation factors can be calculated. Each time these kinetic quantities are calculated the tracked time and trajectories are reset to zero and the process is repeated. This allows the kinetic quantities to converge over averages similar to grand canonical Monte Carlo.

The kinetic properties that are most relevant in this study are the Onsager transport coefficients, self-diffusion coefficients and the correlation factor. The flux of an ion through an interstitial alloy is defined by:

$$\vec{J} = -L\nabla\mu \tag{2.20}$$

where L is the Onsager transport coefficient and μ is the chemical potential of the diffusing species. The Kubo-Green equation relates the Onsager coefficient to the local fluctuations of ions in the material at equilibrium. For a crystalline solid [19, 20],

$$L = \frac{1}{\Omega k_B T} \frac{\langle (\sum_\xi \Delta\vec{R}^\xi(t))(\sum_\xi \Delta\vec{R}^\xi(t)) \rangle}{2dtM} \tag{2.21}$$

where Ω is the volume per site, M is the number of sites in the crystal, and d is the dimensionality of the interstitial network. The vectors $\Delta R^\xi(t)$ connect the end points of the trajectory of atom ξ after the elapse of a time t. The brackets $\langle\rangle$ denote equilibrium ensemble averages.

The correlation factor can also be related to the local trajectories of atoms via [21, 22]:

$$f = \frac{\langle \Delta \vec{R}^2 \rangle}{N \Delta \vec{r}^2} \tag{2.22}$$

where N is the number of total hops and $\Delta \vec{r}^2$ is the elementary hop distance squared. In this work, it represents the distance between octahedral and tetrahedral sites. $N\langle \Delta \vec{r}^2 \rangle$ represents the $\langle \Delta \vec{R}^2 \rangle$ of a particle on a random walk. The correlation factor is a ratio that represents deviation from the ideal random walk.

The chemical diffusion coefficient, D, can be related to the Onsager transport coefficient, L via the derivation below:

$$D \nabla c = L \nabla \mu \tag{2.23}$$

$$D \frac{1}{\Omega} \nabla x = L \frac{\partial \mu}{\partial x} \nabla x \tag{2.24}$$

$$D = L \Omega k_B T \frac{\partial (\mu / k_B T)}{\partial x} \tag{2.25}$$

$$D = L \frac{\Omega k_B T}{x} \frac{\partial (\mu / k_B T)}{\partial \ln x} \tag{2.26}$$

$$D = L \frac{\Omega k_B T}{x} \Theta = D_J \Theta \tag{2.27}$$

The equation also defines the self-diffusion coefficient, D_J. The self-diffusion coefficient can be calculated directly from atomic trajectories during kinetic Monte Carlo. This along with the thermodynamic factor can be used to estimate the chemical diffusion coefficient, D. The thermodynamic factor, Θ, can be calculated from composition fluc-

tuations in the Monte Carlo using a Grand Canonical ensemble [19].

$$\Theta = \frac{\langle N \rangle}{\langle (\langle N \rangle - N)^2 \rangle} \tag{2.28}$$

These averages of these kinetic quantities throughout the kinetic Monte Carlo simulations allow us to examine the effects of long and short-range ordering on diffusion in intercalation compounds and other alloy materials.

2.4 Crystal Mapping

The similarity between a reference and a test crystal can be measured with a mapping score that is zero when the two crystals are identical and large when the two crystals are qualitatively very different. A crystal structure is made of a lattice and a basis (set of atomic positions). The primitive cell is the smallest unit that upon translation can fill the infinite crystal. A structure similarity metric between two crystals can be constructed by comparing the lattices and the atomic positions of their unit cells. The similarity between the *lattice vectors* of a reference crystal and a test crystal can be assessed with a metric that is a function of the strain, ϵ, needed to deform the lattice vectors of the reference crystal to those of the test crystal. The comparison between the *atomic positions* of the reference crystal and the test crystal needs to be performed with care in periodic crystals. The approach adopted here first strains the lattice vectors of the test crystal until they match those of the reference crystal and then determines atomic displacements between the atoms of the reference and the strained test crystal. The metric of similarity in atomic positions is defined as the sum of the square of the displacements normalized by the number of atoms in the unit cell. A good mapping score must take symmetry into consideration. For example, two HCP crystal structures having very different c/a

ratios will differ by a large strain tensor. Nevertheless, the two structures are qualitatively identical. To ensure that symmetry permitted deformations do not penalize the mapping score, only the components of the strain and atomic displacements that break the symmetry of the reference crystal are used to calculate the mapping score.

The sections below describe the mapping algorithm used in this study.

2.4.1 Lattice mapping

The lattice vectors of a crystal can be represented as a column vector matrix $L = [\vec{a}, \vec{b}, \vec{c}]$. The deformation matrix, F, transforms the lattice of a reference structure, L_1, to the lattice of a test structure, L_2, according to $FL_1 = L_2$. F can be decomposed into a symmetric stretch tensor, U, and an orthogonal rotation matrix, R, by $F = RU$. The stretch matrix U can be extracted from F using the following expression:

$$U = \sqrt{F^\top F}$$

The Biot strain tensor for the lattice deformation is $\epsilon = U - I$.

To obtain a single mapping score to measure similarity between two lattices, we need to transform the Biot strain tensor, ϵ, into a single value. Our metric is motivated by considering a homogeneous deformation of a sphere with a radius r. The displacement of any point on the surface of the sphere is $\vec{d} = \epsilon\vec{r}$. The average of the squared displacement of all the points on the sphere can be evaluated according to:

$$\langle d^2 \rangle = \frac{1}{4\pi r^2} \int_\omega r^2 d\omega (\vec{r}^\top \epsilon^2 \vec{r}) = \frac{1}{3} r^2 \mathrm{tr}(\epsilon^2)$$

We use the Wigner-Seitz radius, $r = (6v_1/\pi)^{1/3}$, where $v_1 = V_1/N_1$, V_1 is the volume of the lattice L_1 and N_1 is the number of sites in the basis of the reference crystal. This

yields the following expression for the lattice score:

$$\text{lattice score} = \langle d^2 \rangle = \frac{1}{3}(6v_1/\pi)^{(2/3)}\text{tr}(\epsilon^2)$$

The test structure often has a much larger unit cell than the reference structure. For example, $L1_2$ is a supercell ordering of FCC and contains four basis atoms in its unit cell. In order to get a 1-to-1 assignment of basis sites between FCC and the $L1_2$ ordering, a supercell of FCC containing four primitive unit cells must be constructed. There are many symmetrically distinct supercells that need to be enumerated and tested to identify favorable mappings. An additional subtlety is that there are a multitude of ways to represent the same lattice, each expressible as an integer linear combination of the vectors of a reference lattice vectors, L_1, according to L_1'=$L_1 N_u$, where N_u is a 3×3 matrix of integers having a determinant of $\pm$ 1(i.e. a unimodular matrix). The mapping algorithm of this study, first enumerates all symmetrically distinct supercells of the primitive reference crystal followed by a systematic enumeration over unimodular N_u matrices to identify optimal lattice mappings. The approach we follow is very similar to that described by Trinkle *et al.* [23].

2.4.2 Basis mapping

A basis of a crystal consists of the coordinates of the atomic positions within the unit cell. The first task in mapping the basis sites of a reference structure onto those of a test structure, is to identify a suitable supercell of the reference structure such that it has the same number, N, of atomic positions as the test structure. The test structure is then 'unstrained' by applying F^{-1} to all the basis coordinates and lattice of the test structure. In this state, it is possible to construct a 3 x N displacement matrix, D, that takes the basis of the reference structure to that of the strained test structure.

The basis score depends on the assignment of sites in the first structure to sites in the second structure and a rigid translation used for alignment of the two structures. The basis sites of the reference structure are assigned to those of the test structure using the Hungarian algorithm to minimize the mean-squared-distance between the test basis and the reference basis [24, 25]. Once the displacement matrix is identified, the basis score is the averaged magnitude of the displacement vectors at each site. This can be determined directly by:

$$\text{basis score} = \langle d^2 \rangle = \frac{1}{N}(\text{tr}(D^\top D))$$

where D is the 3 x N displacement matrix. This concept is shown schematically in Figure 2.2.

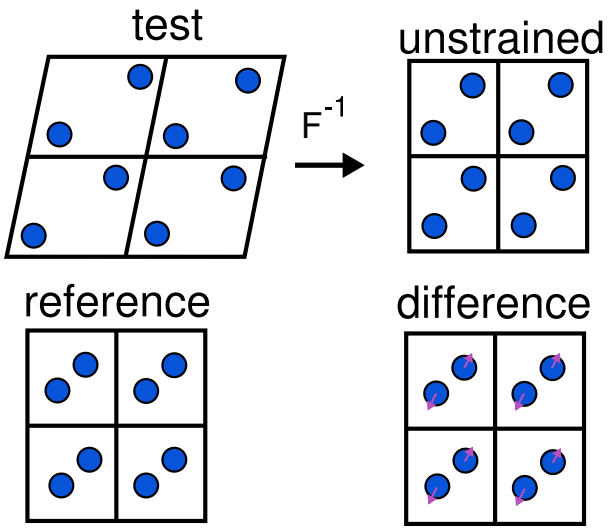

Figure 2.2: A visual representation of the distances that are averaged to create the basis score.

Occasionally, the test structure has fewer basis sites than the primitive cell of the reference structure. We allow virtual sites to the basis of the test structure which effectively allow vacancies to replace the basis sites of the reference basis. The addition of virtual sites makes both structures have a compatible number of basis sites for use of the Hungarian algorithm. The assignment of virtual sites to any site in the reference basis

incur zero penalty during optimization.

2.4.3 Optimizing over both lattice and basis scores

There is no way to optimize two scalar quantities simultaneously without specifying their relative importance. The free parameter w represents this trade-off of importance according to: $s = wl + (1-w)b$ where s, l, and b, are the total structure score, the lattice score and the basis score respectively. By favoring the importance of the lattice score, mappings will be selected that have a larger basis score. Likewise, by weighting the basis score more, mappings will be selected that have larger lattice scores. In this work, we weigh the lattice and basis scores equally with $w = 1/2$.

2.4.4 Symmetry Breaking Mapping Score

Here, we outline a method to remove the parts of the mapping score that preserve the symmetry of the reference structure. After obtaining the strain tensor, ϵ, and the displacement matrix, D, from the initial comparison, we can utilize the symmetry group of the reference crystal structure to extract the parts of ϵ and D that preserve the symmetry of the reference crystal. We accomplish this by applying the Reynolds operator to both ϵ and D. Application of the Reynolds operator to the strain ϵ takes the form:

$$\epsilon_{sym} = \sum_{S \in G} \frac{\hat{S}[\epsilon]}{|G|}$$

where ϵ_{sym} is the component of the strain that leaves the symmetry of the reference crystal unchanged, $\hat{S}$ is a symmetry operation in the symmetry group, G, of the reference crystal. $|G|$ is the number of elements in group G. The Reynolds operator can analogously be applied to D to obtain D_{sym}. We subtract ϵ_{sym} and D_{sym} from ϵ and D and recalculate

the mapping score using the symmetry breaking portions of ϵ and D.

Chapter 3

Hierarchical relationships in crystallographic prototypes

[1]

3.1 Introduction

A materials designer is often eager to identify the chemical composition space in which a desired crystal structure is stable [1, 27, 28]. This requires the calculation of the phase diagrams of many candidate alloy systems by minimizing over the free energies of all crystal structures competing for stability [29]. While the free energy of a phase can be calculated with remarkable accuracy using first-principles statistical mechanics approaches [18, 30, 31, 32, 33, 34, 35, 36, 37, 38, 39], these calculations are expensive and the number of candidate crystal structures is vast. A major challenge, therefore, is to identify a small list of likely crystal structures to consider in a first-principles analysis of phase stability.

[1] This chapter is largely reproduced from previously published work [26].

The task of establishing phase stability in a multicomponent composition space is made easier upon recognizing a natural hierarchy among crystal structures: many compound crystal structures are related to a more manageable number of higher symmetry *parent* crystal structures through a group/subgroup symmetry relation. A solid solution of an fcc crystal structure, for example, may undergo an ordering transition at low temperatures to form an intermetallic compound whereby different chemical species adopt a periodic arrangement over the sites of the fcc lattice. While an ordered phase is usually treated as a distinct crystal structure in most crystal structure databases, they can also be viewed as a derivative of a higher symmetry parent crystal structure. This has been the general philosophy of alloy theorists [40, 41, 42, 43, 44, 18, 45, 46], who have traditionally viewed phase stability as a competition between a variety of high symmetry parent crystal structures that each can form a solid solution along with several derivative ordered phases at particular compositions and temperatures.

There are several advantages to analyzing phase stability within a framework that recognizes the hierarchical relationship between parent crystal structures and their derivative ordered phases. Given a parent crystal structure, there are systematic approaches with which to rapidly enumerate derivative orderings [47]. Furthermore, well-established statistical mechanics schemes based on the cluster expansion approach exist to treat the configurational contributions to the free energy of parent and derivative crystal structures [48, 18, 34, 39]. A recognition that a particular compound may be a derivative ordering of a higher symmetry parent phase also provides insights about the nature of possible phase transformations and the likelihood that a compound may coexist coherently within a disordered matrix phase. In this context, it is often advantageous to measure the degree of symmetry lowering of a compound crystal structure relative to a simpler parent crystal structure with symmetry adapted order parameters that can be generated algorithmically [49, 50, 51] and that can be used to construct generalized free

energy descriptions [32, 52].

While the organization of compound crystal structures within a hierarchical framework is appealing for many purposes, the extent with which such hierarchical relationships exist has not yet been established. Furthermore, if such hierarchical relationships do exist among the majority of compounds, it is not evident which parent crystal structures are most common. Among those that are the most common, which ones host the largest number of distinct ordered phases and which ones are truly unique compound crystal structures that host only one ordering? Are there strong correlations between the occurrence of different parent crystal structures within the same alloy system? Having prior knowledge about one parent crystal structure can then be used to anticipate the occurrence of other parent crystal structures in a particular alloy system.

In this work, we set out to answer these questions. We organize the crystal structures of multicomponent compounds into parent crystal structures and derivative ordered structures using a robust mapping algorithm to compare the similarity between crystal structures. We demonstrate the approach for binary intermetallic structures and show that many intermetallic compounds map onto simple parent crystal structures such as bcc and fcc, but that an even larger number map onto more complex parent crystal structures, including those that belong to the family of topologically close-packed phases. A large number of intermetallic compounds are found to be orderings on parent crystal structures that differ from those of the constituent elements in their pure state. We also find strong correlations between the occurrence of pairs of parent crystal structures in the same binary alloy system. The results of this study suggest the utility of a hierarchical cataloguing of crystal structures for first-principles databases [53, 54, 3, 55] and for the rapid prediction of phase stability in uncharted composition spaces.

3.2 Establishing a hierarchy of crystal structures

Periodic crystals in multicomponent composition spaces can be complex. It is, nevertheless, possible to organize compound crystal structures hierarchically by viewing each compound as a particular decoration of different chemical species over the sites of a high symmetry *parent* crystal structure. An important example is the B2 crystal structure (as designated within the Strukturbericht classification scheme) adopted by CsCl and NiAl. Figure 3.1(a) shows that B2 is a simple chemical ordering over the sites of a bcc parent crystal structure. Similarly, the common $L1_2$ and $L1_0$ crystal structures formed by Ni_3Al and TiAl, respectively, correspond to periodic orderings of two chemical species over the sites of an fcc parent crystal structure (Figure 3.1(b)). Other intermetallic compounds can be mapped onto more complex parent crystal structures. Figure 3.1(c), for example, shows that C32 and $B8_2$ correspond to chemical decorations of an ω parent crystal structure.

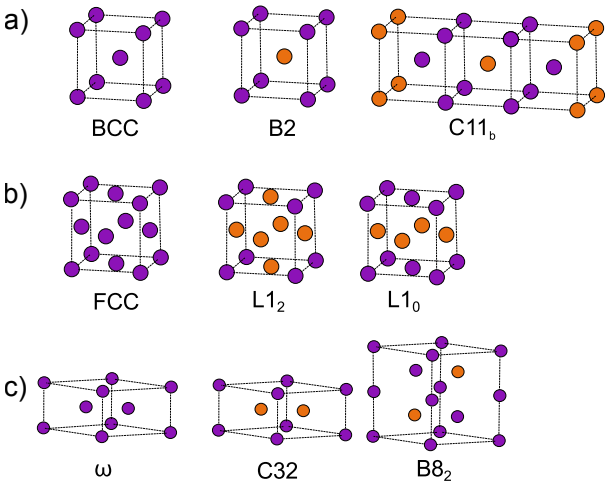

Figure 3.1: Illustrations of basic (parent) crystal structures and decorations that occur on them that are commonly seen intermetallics.

The identification of the parent crystal structure of a particular compound is not always trivial. This is especially true when the chemical ordering of the compound has

a symmetry that is lower than that of the undecorated parent crystal structure. For example, while the ordering of $L1_2$ preserves the cubic symmetry of the underlying fcc lattice, the layered ordering of $L1_0$ does not, and compounds adopting this structure often undergo a slight tetragonal distortion of their unit cell vectors. Eliminating the distinction between Ti and Al in $L1_0$ TiAl, for instance, produces an undecorated crystal that is not perfect fcc, but rather a face centered tetragonal crystal. Nevertheless, the tetragonal distortion is sufficiently small in most $L1_0$ forming compounds that they can still be considered as having an fcc parent crystal structure. Other common crystals that can be viewed as a symmetry-breaking ordering of a parent crystal structure include $C11_b$, which has a lower symmetry than undecorated bcc (Figure 3.1(a)), and $B8_2$, which lowers the symmetry of undecorated ω (Figure 3.1(c)).

The examples of $L1_0$, $C11_b$ and $B8_2$ demonstrate the need for a robust method of establishing similarity between any pair of crystal structures when attempting to identify the parent crystal structure of a compound. In comparing two crystal structures it is necessary to determine the similarity between (i) the lattice vectors and (ii) the atomic positions of both structures. The similarity between two crystal structures can be measured with a mapping score that is zero when the two crystals are identical and large when the two crystals are qualitatively very different. Section 2.4 describes a robust approach to measure the dissimilarity of two crystal structures. The approach differs from other structure comparison algorithms that rely on comparing crystal invariants, pair distribution functions or symmetry features such as space group and Wyckoff positions [56, 57, 58, 59, 60]. Instead, the approach is similar in spirit to those that measure geometric similarity by identifying an affine mapping between a pair of crystal structures [61, 62]. It measures crystal similarity with a cost function that depends on the symmetry breaking strains and atomic displacements along different paths that convert one crystal structure into the other. In this sense, care is taken to remove strains and distortions

that preserve the symmetry of the reference structure being mapped onto. For example, two hcp crystals may have very different c/a ratios and, therefore, require a large strain to convert one into the other. Nevertheless, this strain preserves the symmetry of the hcp crystal and should not contribute to any metric that is used to determine if two crystal structures are qualitatively identical. The mapping of one crystal onto the other relies on a lattice mapping algorithm similar to that described by Trinkle *et al.* [23] and a basis mapping that relies on the Hungarian algorithm [24, 25].

3.3 Hierarchy among intermetallic crystal structures

The organization of compound crystal structures into *parent* crystals and derivative *ordered* structures can be performed for any class of compounds, including intermetallics, oxides, sulfides, nitrides etc. Here we limit the analysis to binary intermetallic compounds. To this end, we collected elemental and intermetallic crystal structures from the Materials Project [3] and the International Crystallography Structure Database (ICSD) [63]. Only single component and binary crystal structures containing the metallic elements highlighted in blue in Figure 3.2 and containing less than 60 atoms in their unit cells were considered.

The structures extracted from the Materials Project were restricted to those with an ICSD identification number. Structures with partial occupancies and up to two of the elements shown in Figure 3.2 were collected from the ICSD. Structures with partial occupancies were converted to stoichiometric compounds by filling each partially occupied site by the majority element of that site. A total of 4335 elements and compounds were collected in this manner. It is important to recognize that crystal structures from the ICSD database are ones that have been observed experimentally. However, not all of these crystal structures correspond to equilibrium phases and our analysis is, therefore,

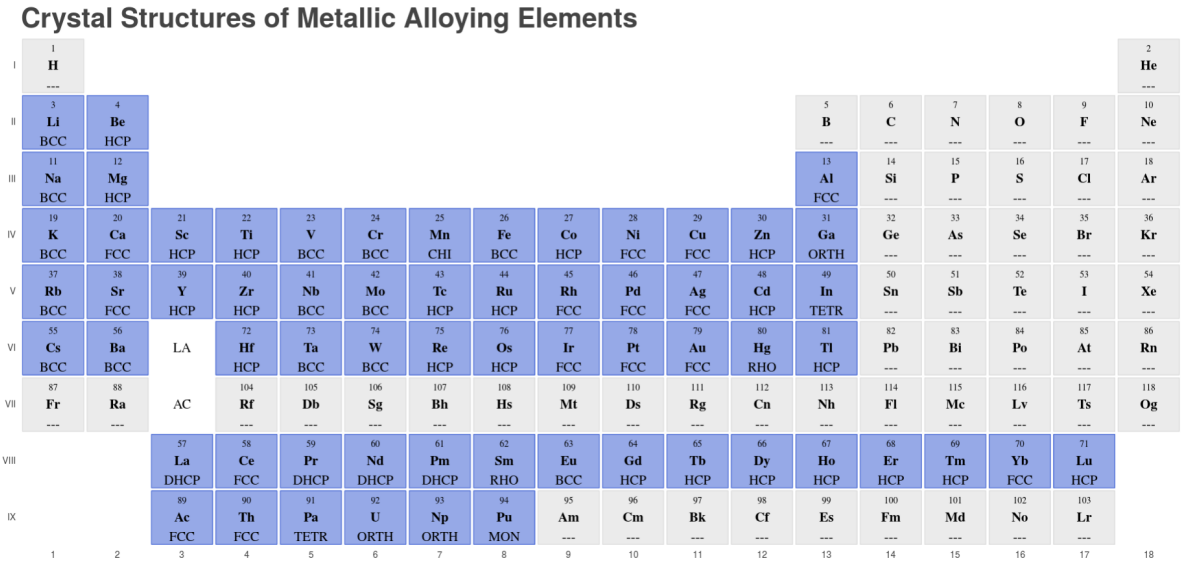

Figure 3.2: The crystal structures of elemental compounds. Elements marked with no crystal structure were not considered as a potential alloying element in this study.

not necessarily reflective of trends displayed by thermodynamically stable phases. Other biases are also likely present in this data set. For example, complex crystal structures with large unit cells tend to be more difficult to refine than simpler ones and may, therefore, be under reported. The relative frequencies and crystal structure rankings extracted from this data set should consequently only be viewed as a qualitative indication of the likelihood of encountering those phases in a particular alloy.

The mapping algorithm described in the Section 2.4 was applied to all 4335 elements and compounds, resulting in the identification of 455 unique crystal structures. This list still included crystal structures that can be viewed as a particular chemical ordering over a higher symmetry parent crystal structure. To identify unique parent crystal structures, each of the 455 unique crystal structures was undecorated and mapped on the remaining set of entries. If a particular crystal structure was able to map onto a simpler structure having the same or higher symmetry with a mapping score below a predefined threshold, it was considered a derivative ordered phase, while the structure it mapped onto was made a

candidate for a parent crystal structure. This led to the identification of 267 unique parent crystal structures. All parent crystal structures and their derivative ordered structures have been deposited in an interactive online database [64].

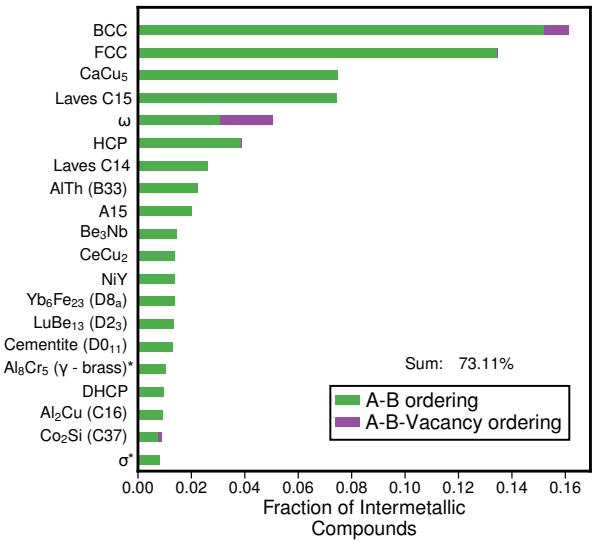

Figure 3.3: The distribution of compounds across the top 20 most common parent crystal structures for binary metallic alloys. The purple represents ordered phases that contain vacancies. Parent crystals marked with a star have a large portion of compounds with partial occupancies.

3.3.1 The top twenty parent crystal structures

Figure 3.3 shows a histogram for the top twenty most common parent crystal structures. The horizontal bar for bcc, for example, represents the fraction of binary compounds that are a particular ordering on bcc. The bar also includes all the elements highlighted in blue in Figure 3.2 that have been reported as bcc. When assigning a particular compound crystal to a higher symmetry parent crystal, we allowed for the presence of vacancies and simple clusters of atoms such as dumbbells on a subset of sites of the parent crystal. The fraction of compounds that contain vacancies when mapped onto a particular parent crystal structure are shown in purple. Crystallographic information about each of the top twenty parent crystal structures is listed in Table 3.1.

Parent Crystal	# of Atoms in Primitive Cell	# of Distinct Crystallographic Sites	Layering Pattern	# of Distinct Orderings
bcc	1	1	-	44
fcc	1	1	ABC	32
$CaCu_5$	6	3	Aα	5
Laves C15	6	2	α[acb]β[bac]γ[cba]	3
ω	3	2	aH_a	8
hcp	2	1	ABAB	14
Laves C14	12	3	α[acb]β[bca]	6
AlTh	4	2	AlTh	1
A15	8	2	-	2
Be_3Nb	12	5	Aα[abc]γAβ[bca]αAγ[cab]β	1
$CeCu_2$	6	2	$CeCu_2$	1
NiY	8	2	NiY	1
Yb_6Fe_{23}	29	29	-	1
$LuBe_{13}$	28	12	-	1
Cementite	16	3	Cementite	1
Al_8Cr_5	26	9	-	12
dhcp	4	2	ABAC	7
Al_2Cu	6	2	Sθ_aSθ_b	1
Co_2Si	12	3	Co_2Si	4
σ	30	5	$\theta_a\sigma_0\theta_a\sigma_\pi$	4

Table 3.1: The primitive cell size, number of distinct crystallographic sites, layering patterns and number of chemical orderings of the top 20 most common parent crystal structures. The notation used to describe each two-dimensional layer is described in Appendix A.

The top twenty parent crystal structures account for almost 75% of the 4335 elements and intermetallic compounds analyzed in this study. 158 of the remaining 247 parent crystal structures only have one or two compounds that map onto them. Figure 3.3 shows that a large fraction of intermetallic compounds are orderings on bcc and fcc. These constitute approximately 30% of all the compounds considered in this study. Perhaps a surprising outcome is the high frequency of complex parent crystal structures such as $CaCu_5$, Laves C15 and ω. Each one of these parent crystals appear with a higher frequency than hcp-derived orderings.

Table 3.1 summarizes crystallographic information about each of the top twenty parent crystals. The second column lists the number of atoms per primitive unit cell. Only bcc and fcc have simple parent crystal structures with one atom in their primitive unit cells. The majority of other parent crystal structures are much more complex and have large unit cells. Nevertheless, fifteen of the top twenty parent crystals can be described as a particular stacking sequence of simpler two-dimensional motifs. Appendix A describes the two-dimensional building blocks and their naming convention. The stacking sequences of the layered parent crystals is listed in the third column of Table 3.1.

While our analysis has yielded 267 distinct parent crystal structures, the fourth column of Table 3.1 shows that only a few among the top twenty host multiple chemical orderings. The parent crystal structures that support more than one chemical ordering also tend to occur with a higher frequency. Furthermore, Table 3.1 shows that the simpler parent crystal structures such as bcc, fcc and hcp have the largest number of chemical orderings. Figure 3.4 breaks down the histogram bars of the top six parent crystal structures of Figure 3.3 by the frequency with which different orderings occur. The bar for bcc in Figure 3.4 shows that B2 is the most common ordering on bcc. It is in fact the most common derivative ordered structure among all the compounds considered in this work. The $L1_2$ ordering dominates on fcc, while other well known fcc orderings such as $L1_0$ occur much less frequently. The ω parent crystal structure also hosts several different orderings. Two of these have already been discussed and are shown in Figure 3.1(c). Overall, most of the ordered compounds occur at simple stoichiometric compositions such as 1/2, 1/3, 1/4, and 1/6.

An interesting result that emerges from our analysis is that some intermetallic compounds can tolerate high concentrations of vacancies. B2 NiAl, for example, accommodates an excess of Al by introducing vacancies on its Ni sublattice [65]. These vacancies, which can reach concentrations as high as 15%, tend to order over the Ni-sublattice sites

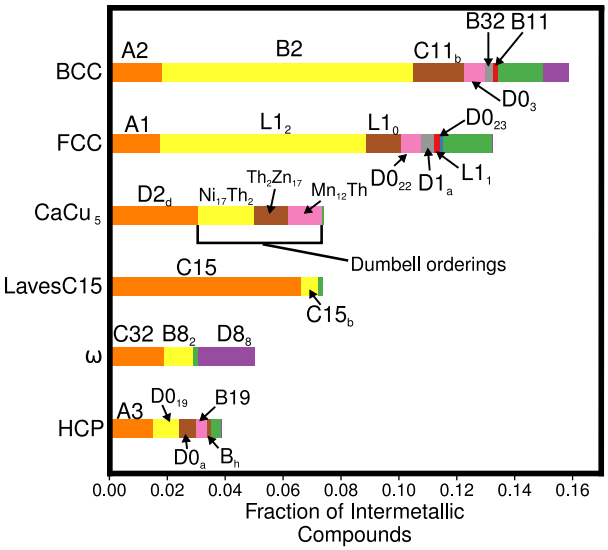

Figure 3.4: The break down of ordered compounds among the top 6 most common parent crystal structures for binary metallic alloys. Each ordering is labelled by its Strukturbericht prototype name. Orderings that do not have a Strukturbericht prototype name are pooled together and represented with the green blocks. The purple blocks represent orderings that contain vacancies.

at low temperatures, thereby forming lower symmetry intermetallic compounds [66]. The $D8_8$ compound was found to map onto the ω parent crystal structure if one third of the sites in every triangular layer are vacant. The histograms of Figure 3.3 and Figure 3.4 account for these vacancy ordered compounds, with the fraction of compounds containing vacancies shown in purple. A striking result is that the vacancy ordered intermetallic compounds are primarily restricted to the bcc and ω parent crystal structures. Furthermore, over half the bcc intermetallic compounds that contain vacancies also contain Al.

Both the $CaCu_5$ and Laves C15 parent crystal structures appear prominently, occupying the third and fourth positions, respectively, in the histograms of Figure 3.3 and Figure 3.4. Both are Laves-like phases, consisting of triangular and kagomé layers, and are common among binary compounds in which the constituents have very different atomic radii [67, 68]. The larger constituent occupies a subset of the triangular layers,

while the kagomé layers are exclusively occupied by the smaller constituent. Figure 3.4 indicates that Laves C15 does not host many distinct orderings and is dominated by the C15 prototype. The $CaCu_5$ parent crystal structure, in contrast, has been assigned five prototype orderings in Figure 3.4. However, the $Ni_{17}Th_2$, Th_2Zn_{17}, and $Mn_{12}Th$ prototype orderings assigned to $CaCu_5$ can only be described as superstructure orderings over the sites of $CaCu_5$ provided that dumbbells occupy a subset of the Ca sites. This is described in more detail in Appendix A.

The number of observed ordered compounds on each parent crystal structure (Table 3.1) is only a small fraction of the total number of geometrically possible orderings. The enumeration of symmetrically distinct orderings within supercells of the primitive unit cell of a parent crystal is a solved combinatorics problem [47]. Figure 3.5 compares the number of observed orderings to the total number of possible symmetrically distinct orderings as a function of their supercell volume (in integer multiples of the primitive unit cell of the parent crystal) [69] for bcc, fcc and hcp. While the number of possible orderings increases dramatically with increasing supercell size, the number of observed orderings peak at a supercell volume of four times the primitive unit cell for both the bcc and fcc parent crystal. Even at small supercell volumes, not all possible orderings are represented in nature. For example, there are two symmetrically distinct orderings on bcc in supercells consisting of two primitive bcc unit cells. Only the B2 ordering is observed in nature. The other, made up of alternating (110) planes of pure A and B is not among the list of bcc orderings found in this study. This is consistent with a ground state analysis of the bcc crystal, which showed that of the two possible orderings, only B2 can be a ground state for a lattice model with first and second nearest neighbor pair interactions [45]. This suggests that many of the commonly observed orderings are likely stabilized by short-range interactions. It does not, however, mean that more complex orderings are necessarily thermodynamically unstable. Ground state analyses of lattice models show

that more complex orderings in large unit cells require long-range interactions (beyond first and second nearest neighbor shells) [45, 44]. As long-range interactions tend to be weaker than short-range interactions, the order-disorder transition temperatures of more complex orderings will generally be lower than those of simpler orderings. Hence, they are less likely to be observed as their formation requires equilibration at low temperature. Kinetic factors may also hamper their formation as it will be easier to quench in local disorder before a complex ordered pattern can be realized through coordinated atomic motion.

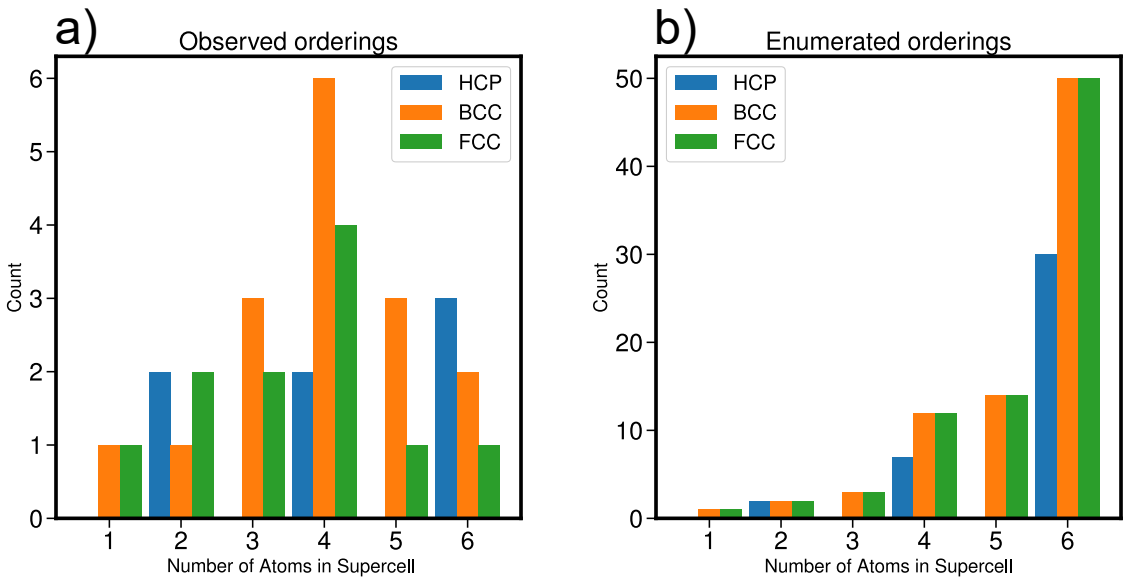

Figure 3.5: The number of a) experimentally observed orderings and b) geometrically possible (enumerated) orderings as a function number of atoms in a supercell for bcc, fcc, and hcp.

3.3.2 Crystal hierarchies for important metallic alloys

Parent crystal structures can also be ranked based on their frequency in more restricted alloy classes. Figure 3.6 shows the distribution of parent crystal structures in Al, Mg, Ni, Zn, Fe, and Ti rich binary alloys. A comparison of the histograms for each

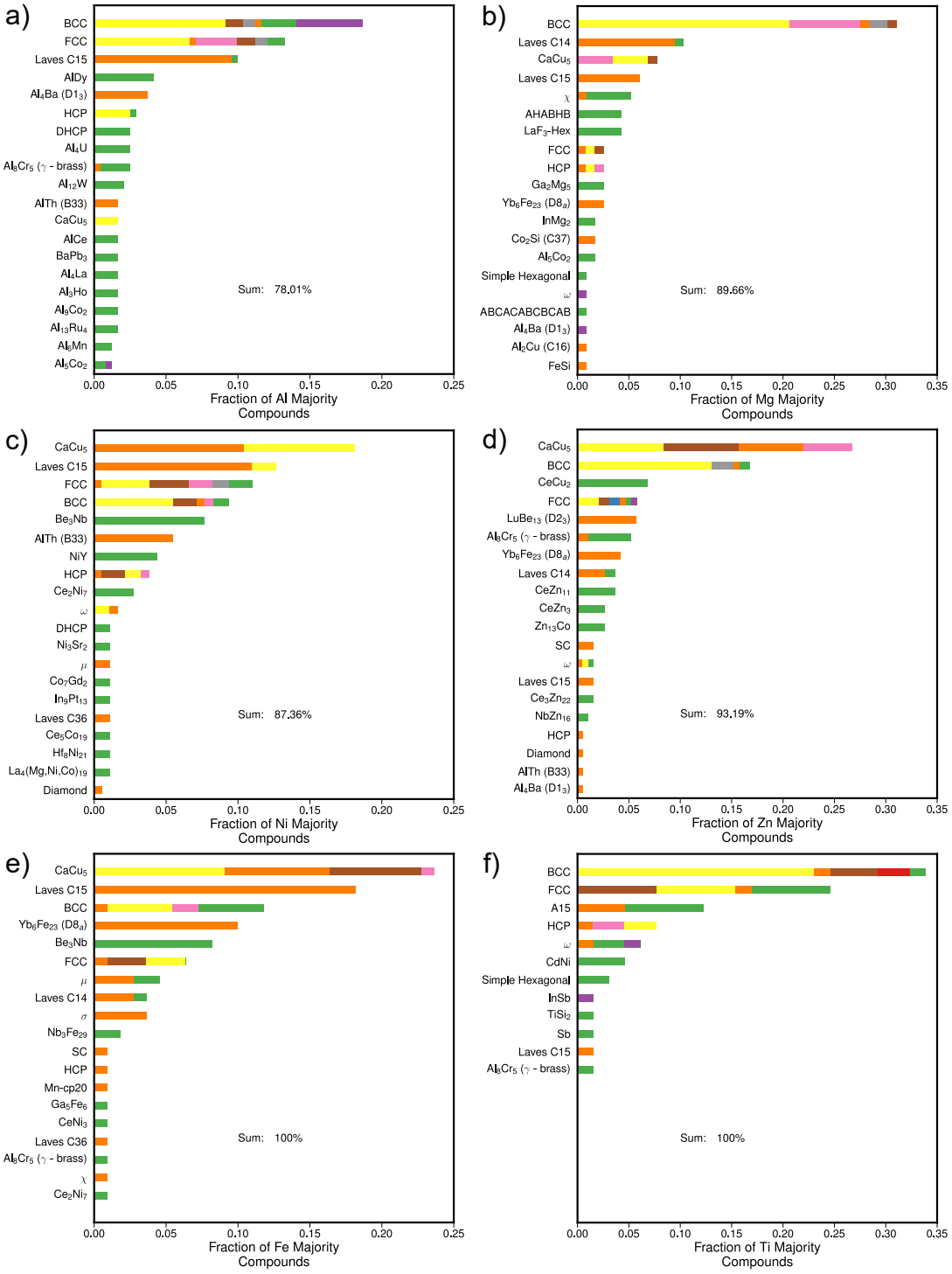

Figure 3.6: The distribution of compounds across parent crystal structures for Al, Mg, Ni, Zn, Fe, and Ti - rich binary alloys. The colored bars refer to the same orderings as in Figure 3.4. For parent crystals not shown in Figure 3.4, orange bars indicate an ordering with a Strukturbericht designation, green bars correspond to orderings without any label and purple indicates orderings that contain vacancies.

of the six alloy classes shows that there can be a large variability among the top parent crystal structures. For example, the most frequent parent crystal structures when only considering compounds having a majority of either Ni or Fe are $CaCu_5$ and Laves C15 instead of bcc and fcc. Binary compounds containing a majority of either magnesium, aluminum, or zinc form a large number of bcc orderings even though the elements themselves adopt either the hcp or fcc crystal structure at ambient temperatures and pressures. Aluminum rich alloys are much more likely than the others to accommodate large vacancy concentrations in bcc based intermetallic compounds as is evident by the large purple block on its bcc bar. Figure 3.6 also shows that titanium rich alloys and iron rich alloys only have a limited number of parent crystal structures, with 12 for Ti and 19 for Fe. Zn majority compounds frequently show up on the $CeCu_2$ parent crystal which is unlike the other five alloy classes.

3.3.3 Correlations between the occurrence of crystal structures

We have so far only considered the frequency with which each parent crystal structure occurs in binaries of metallic elements. Also of interest are correlations between pairs of parent crystal structures. That is, for any given pair of parent crystal structures A and B, are they more likely or less likely to appear together in the same binary system than would be expected from independent random sampling? This can be quantified with the following correlation parameter:

$$\kappa = \frac{P(\mathrm{A}+\mathrm{B})}{P(\mathrm{A})P(\mathrm{B})} - 1$$

where $P(\mathrm{A})$ and $P(\mathrm{B})$ are the probabilities with which parent crystal structures A and B occur. For intermetallic phases, we estimate these probabilities by the frequency with which they occur among all the binary systems analyzed in this study. The joint

probability P(A+B) represents the probability that the parent crystal structures A and B are both observed in the same binary system.

If the occurrence of parent crystal structures A and B in any binary system is uncorrelated, then P(A+B)=P(A)P(B) and the correlation parameter κ becomes equal to zero. If κ is positive, then the simultaneous presence of A and B in any binary occurs more frequently than that expected from independent random sampling. κ is less than zero when the A and B parent crystal structures are anti-correlated and κ assumes its minimum value of -1 when A and B never occur together in any binary system (i.e. P(A+B)=0).

Figure 3.7 displays the matrix of correlation parameters, κ, calculated for all pairs of the top twenty parent crystal structures for the intermetallic compounds considered in this study. The off-diagonal entries contain κ values for pairs of different parent crystal structures. Since several parent crystal structures host multiple derivative ordered structures, it is common that a binary system will exhibit two compounds that are derived from the same parent crystal structure. The diagonal elements of the correlation matrix in Figure 3.7 account for these occurrences. Blue signifies a positive correlation, while red indicates a negative correlation.

Figure 3.7 shows that the Laves-like phases are highly correlated with each other. The Laves-like $CaCu_5$ parent crystal, for example, has large κ entries with C15 and Be_3Nb. This is a reflection of the fact that multiple Laves-like phases with different stoichiometries tend to appear in the same binary. It is well-known that Laves-like phases form when mixing elements with different atomic radii [67, 68]. Figure 3.7 shows that cementite ($D0_{11}$) and Yb_6Fe_{23} ($D8_a$) are also highly correlated with Laves phases. The correlation between cementite and Be_3Nb is especially large, with a correlation parameter of κ=24. Both cementite and Yb_6Fe_{23} also tend to form between elements with large differences in atomic radii and can, therefore, be expected in the same binaries that form Laves-like

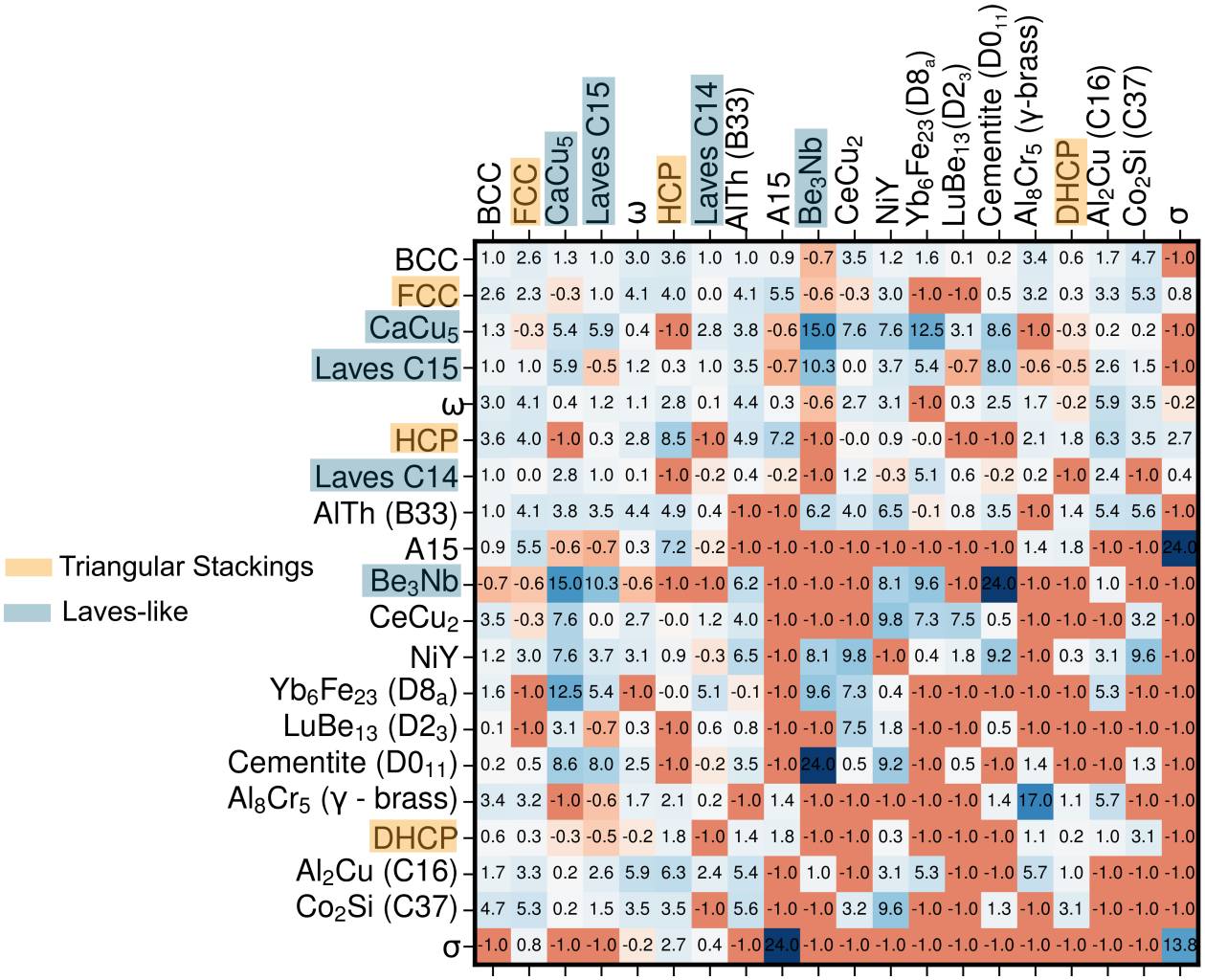

Figure 3.7: A matrix that displays the degree with which pairs of parent crystal structures are correlated over binary alloy systems. The numerical values respresent the κ correlation parameter. Positive values indicate that derived orderings of pairs of parent crystal structures occur more frequently than independent sampling. Negative quantities indicate that the pair of parent crystal structures are anticorrelated. Positive (negative) values have been colored a degree of blue (red) to reflect their magnitude for easy visualization of the matrix.

phases. Laves C14 is unlike the other Laves-like phases in that its correlation parameter, κ, with other parent crystals is generally small, including with other Laves-like phases and cementite, indicating that it does not tend to coexist with other parent crystals in the same binary systems.

Another notable trend in Figure 3.7 is that hcp is very strongly anti-correlated with

Laves-like phases. The other close-packed parent crystals, including fcc and dhcp, also show negligible to negative correlations with Laves-like phases. This likely is a result of the instability of close-packed phases when mixing constituents with large differences in atomic radii as was recently shown in a first-principles study [68]. A15 and the σ parent crystals show an especially large number of κ=-1 entries, meaning that they do not occur with many of the other top 20 parent crystals in binary alloys. However, the two parent crystals are very strongly correlated with each other, with κ=24. This coexistence could be due to the fact that both structures have coordination environments in which a central atom is connected to 12 other atoms in its coordination shell. Alternatively, the fact that A15 and σ are both very prominent in refractory containing intermetallics could explain the high κ value. A15 also has large κ values with the close-packed fcc and hcp phases. Both Al_8Cr_5 (γ-brass) and σ have very large diagonal κ values indicating that binaries with these phases have multiple derivatives of these phases.

It is also of interest to inspect the extent to which particular parent crystal structures are correlated with the crystal structures of the pure constituents. This is collected in the matrix of Figure 3.8. Each row in Figure 3.8 corresponds to a particular combination of pure element crystal structures. The first row, for example, collects all binary systems in which both constituents form hcp as pure elements. The rows are ordered by the number of binaries of each category. For example, the second to last column shows that there are 484 binaries made up of constituents that are both hcp in their pure form. The second most common type of binary is made up of a combination of an fcc and an hcp element; there are 330 binaries of this type.

Figure 3.8 indicates that a combination of two hcp elements results in a large number of bcc and Laves-like $CaCu_5$ derived compounds. Surprisingly, the fraction of hcp derived orderings are very low (only 3%) among these binaries, in spite of the fact that both end members are hcp. The next most frequent category of binaries, made of an fcc and

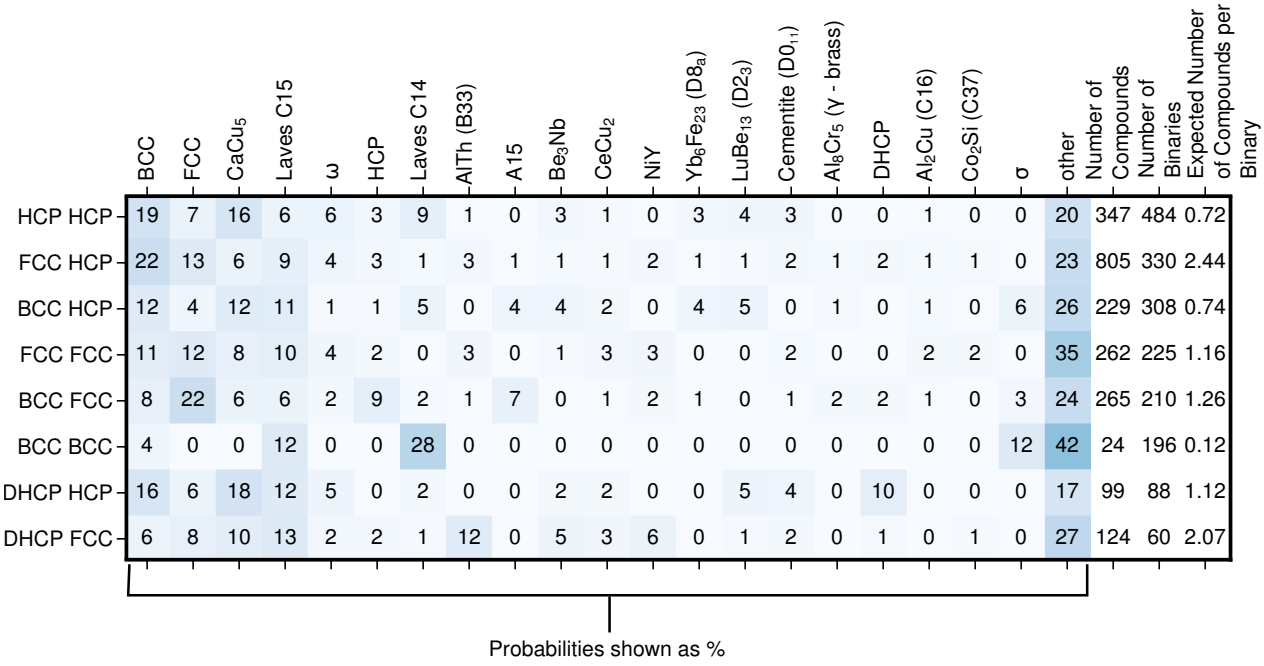

Figure 3.8: The probability (in percent) of the occurrence of each of the top twenty parent crystal structures broken down by the type of crystal structures of the constituents. The "Other" column denotes the percent of all remaining parent crystal structures.

an hcp element, also results in a high fraction of bcc derived intermetallic compounds (22%). fcc derived intermetallics are a distant second (13%) and, as with the hcp-hcp binaries, the fraction of hcp intermetallics is very low. The last column of the matrix in Figure 3.8 lists the average number of compounds per binary in each category. The combination of an fcc and hcp element leads to an average of 2.44 compounds per binary, which is substantially higher than all other categories, with the exception of the dhcp-fcc category, which has a value of approximately 2. The binaries made of two bcc elements show a very high probability of C14 formation and to a lesser extent the σ phase. Also notable about this category is the very low average number of compounds per binary, with a value of 0.12. Furthermore, a high fraction of compounds formed in the bcc-bcc category are categorized among the parent crystal structures below the top 20 discussed in this study (42%).

3.4 Discussion

The existence of a hierarchy among intermetallic compounds and simpler parent crystal structures has been recognized in materials science for many decades. Metallic binary systems commonly have intermetallic compounds that undergo order-disorder transitions to a solid solution on the same parent crystal structure at high temperature. A well-known example is CuZn, which forms the B2 ordering at low temperature but disorders through a second-order transition to a bcc solid solution upon heating [70]. Many thermodynamic descriptions of multi-component crystalline solids exploit the crystallographic relationships that exist between a parent crystal and their derivative orderings [41, 42, 71, 44, 18, 46, 49]. However, these descriptions have primarily been restricted to the simpler parent crystal structures such as bcc, fcc and hcp.

Here we investigated the extent with which intermetallic compounds more generally can be viewed as derivative ordered structures of higher symmetry parent crystal structures. The fact that 3/4 of the intermetallic compounds considered in this work can be mapped onto 20 simpler parent crystal structures suggests that a classification based on this hierarchical relationship is meaningful for a large number of intermetallic compounds. Of particular interest is the large number of parent crystal structures in the top 20 that have a complex topology and that also host multiple derivative chemical orderings. These include the ω phase, two Laves phases and Al_8Cr_5. Furthermore, parent crystal structures such as bcc and ω are found to host chemical orderings with high concentrations of vacancies, a possibility that is often overlooked in high throughput studies of phase stability.

The concept of a parent crystal structure plays a central role in first-principles and empirical thermodynamic descriptions of multi-component solids. Different orderings on a common parent crystal structure can be distinguished from each other and from a

disordered solid solution with the help of long-range order parameters [41, 42, 49]. This makes it possible to describe the thermodynamic properties of a parent crystal structure and its derivative orderings with a common free energy surface that is a function, not only of concentration, temperature and pressure, but also of long-range order parameters. Stable chemical orderings on a parent crystal structure then correspond to local minima on this common free energy surface. First-principles statistical mechanics methods that rely on the cluster expansion approach and Monte Carlo simulations are now routinely used to construct such free energy surfaces [49, 52, 72]. Ultimately, global phase stability is determined by a minimization over the free energy surfaces of multiple competing parent crystal structures.

The calculation of the phase diagram of a new and uncharted alloy system with first-principles statistical mechanics methods requires a manageable, ranked list of candidate parent crystal structures, as the computational cost of calculating a free energy surface for a single parent crystal can be high [35, 73, 66]. It is therefore of interest to have the ability to anticipate likely parent crystal structures for a particular composition space. In this context, simple descriptors that depend only on the elemental constituents of the alloy are desirable. Chemical descriptors, such as ionic radii and electronegativity, are commonly invoked to explain and rationalize crystal preferences within an alloy [74, 67, 68]. They can also be used to assess the likelihood of a particular parent crystal structure within a given composition space. Figure 3.9, for example, shows the density distribution for each of the top twenty parent crystals as a function of the radius ratio R_{big}/R_{small} and electronegativity difference $\chi_{big} - \chi_{small}$ of the binary constituents that form derivative orderings on each parent crystal.

As is clear in Figure 3.9, the density distributions of many of the top twenty parent crystal structures are localized within a restricted region of R_{big}/R_{small} and $\chi_{big} - \chi_{small}$ space. Exceptions are ω, Laves C14 and Co_2Si (C37), which have more spread out density

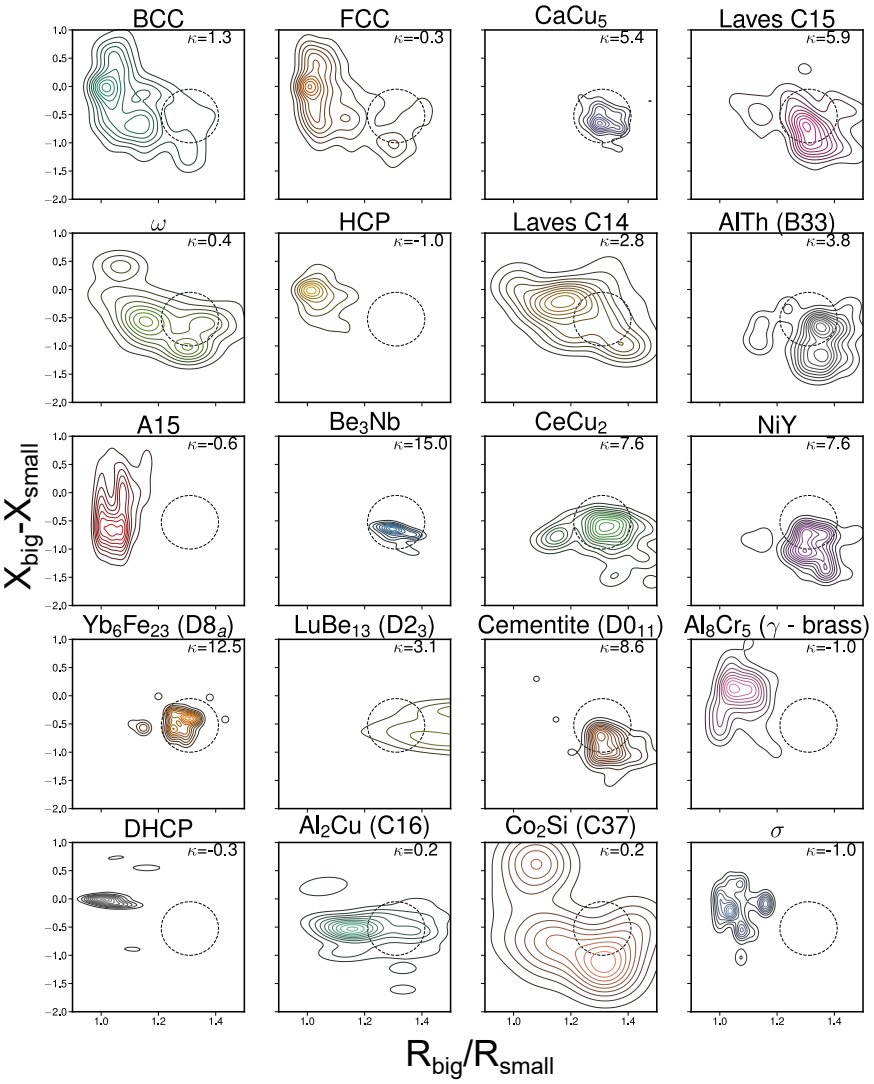

Figure 3.9: Contour plots of the kernel density estimates (KDEs) of the distributions of chemistries on the top twenty parent crystals Figure 3.7. The KDEs are over the distribution of radius ratio and electronegativity difference of the elements present in the binary intermetallic. The κ correlation values of each parent crystal with respect to $CaCu_5$ is also shown on each plot. The majority of $CaCu_5$ chemistries form with radius ratios between 1.2 and 1.4 and electronegativity differences of -1 to 0. This region is denoted by the dashed circles.

distributions. The simple parent crystal structures, such as bcc, fcc and hcp tend to be favored when combining elements that have similar atomic radii (i.e. $R_{big}/R_{small} \approx 1$). Other more complex crystals, such as A15 and σ also tend to be formed by elements that have similar atomic radii. The Laves-like phases, such as $CaCu_5$, C15 and Be_3Nb, in contrast, form in binaries having a large radius ratio R_{big}/R_{small} between the constituents. For example, pairs of chemical species that combine to form compounds that are derivative orderings of $CaCu_5$ have radius ratios between 1.2 and 1.4 and electronegativity differences between 0 and -1.0.

Overall, the density distributions of Figure 3.9 suggest that simple descriptors can be used as a first approximation to assemble a ranked list of likely parent crystal structures. A further narrowing of likely parent crystal structures in an unexplored composition space can be achieved by exploiting empirically established correlations among parent crystal structures, as, for example, measured by the correlation parameter κ tabulated in Figure 3.7. Any prior knowledge about the existence of one parent crystal structure increases the likelihood of other parent crystal structures that it is highly correlated with. For example, the existence of a $CaCu_5$ derived compound in an alloy system strongly suggests that Be_3Nb, Yb_6Fe_{23}, cementite ($D0_{11}$), $CeCu_2$, NiY and Laves C15 may also form in the same binary system as these parent crystals have a high κ value with respect to $CaCu_5$. The high degree of correlation between these particular parent crystal structures is also reflected by the density distributions in R_{big}/R_{small} and $\chi_{big} - \chi_{small}$ space of Figure 3.9.

The dashed circles in each density distribution plot of Figure 3.9 encompasses the domain in R_{big}/R_{small} and $\chi_{big} - \chi_{small}$ space corresponding to the binary alloys that form $CaCu_5$ derivatives. Also shown in each density distribution plot are the κ values of Figure 3.7 for each parent crystal with respect to $CaCu_5$. Figure 3.9 clearly shows that Be_3Nb, Yb_6Fe_{23}, cementite ($D0_{11}$), $CeCu_2$, NiY and Laves C15, which are highly

correlated with $CaCu_5$ in that they commonly appear together in the same binary, also have a high density in the same region of R_{big}/R_{small} and $\chi_{big} - \chi_{small}$ space. This overlap shows that the more complex parent crystal structures such as the Laves-like phases, cementite, $CeCu_2$ and NiY tend to form when mixing elements having a large size mismatch. It is also clearly evident in Figure 3.9 that parent crystal structures that have a negative correlation κ with respect to $CaCu_5$, including HCP, A15, Al_8Cr_5, dhcp and σ, have density distributions that falls outside the dashed circle.

While simple descriptors such as radius ratio and electronegativity differences appear to explain correlations between $CaCu_5$ and other parent crystal structures, it is not always as clear cut for the other top twenty parent crystal structures. Appendix A shows similar plots to that of Figure 3.9 for each of the top twenty parent crystal structures. In many cases, the correlations between pairs of parent crystal structures are consistent with a large overlap of their density distributions in R_{big}/R_{small} and $\chi_{big} - \chi_{small}$ space. However, there are also many cases where this is not true, suggesting that further work is required to identify a larger set of descriptors with which the occurrence of each parent crystal structure can be predicted with a high degree of confidence. More data, either experimental or first-principles, will also be required to improve the quantitative reliability of correlations reported here.

Our analysis has so far been restricted to intermetallic compounds. However, similar hierarchies exist among more complex compounds such as oxides, sulfides, nitrides etc. Corundum Al_2O_3, for example, can be viewed as a particular Al-vacancy ordering over the interstitial sites of an hcp oxygen sublattice, while anatase TiO_2 is a particular Ti ordering over the octahedral interstitial sites of an fcc oxygen sublattice [75]. More esoteric oxides such as NbO, WO_3 and MoO_3 can be derived from rocksalt as a particular ordering of vacancies on both its metal and oxygen sublattices. The anions of oxides and sulfides tend to be bigger and more abundant than the metal cations. In many oxides and

sulfides, the anions, therefore, form a close-packed sublattice such as fcc or hcp, while the metal cations fill interstitial tetrahedral or octahedral sites. There are, of course, many exceptions to this trend with a vast array of complex oxide and sulfide crystal structures that have more complex anion sublattices. In contrast to oxides and sulfides, the nitrides and carbides commonly have more metal cations than nitrogen or carbon. Many of their crystal structures can therefore be viewed as a close-packed metal sublattice with nitrogen or carbon occupying interstitial sites [73].

3.5 Conclusion

It has long been recognized that common intermetallic crystal structures such as B2 and $L1_2$ are super lattice orderings of simpler parent crystal structures such as bcc and fcc. Common first-principles statistical mechanics approaches to calculate finite temperature phase stability exploit the hierarchical relationship between ordered compounds and their underlying parent crystal structures. In this work we have explored the extent to which intermetallic compounds in general can be viewed as derivative orderings on higher symmetry parent crystal structures. Our analysis was enabled by a robust mapping algorithm to measure the similarity between crystal structures. We found that a large fraction of intermetallic compounds can indeed be viewed as chemical orderings over a small number of higher symmetry parent crystal structures. While many compounds are derivative orderings of bcc and fcc, a larger number are found to be orderings of more complex crystal structures that include ω and Laves phases. A similar approach can be applied to categorize other classes of crystalline materials including oxides, sulfides, carbides, nitrides etc. The hierarchical organization of crystal structures into high symmetry parent crystals and derived ordered structures should enable the development of a deeper understanding of the relationship between crystal structures and lays the

foundation for the efficient calculation of phase diagrams in new alloy systems.

3.6 Acknowledgments

This work was supported by the ONR BRC Program, Grant Number N00014-18-1-2392, the NFS IDEAS center, Grant Number 1934641 and the Schmidt Family Foundation. Use was made of computational facilities purchased with funds from the National Science Foundation (CNS-1725797) and administered by the Center for Scientific Computing (CSC). The CSC is supported by the California NanoSystems Institute and the Materials Research Science and Engineering Center (MRSEC; NSF DMR 1720256) at UC Santa Barbara. We are also grateful for computing resources from the National Energy Research Scientific Computing Center (NERSC), a U.S. Department of Energy Office of Science User Facility operated under Contract No. DE-AC02-05CH11231.

Chapter 4

Transformation pathways between simple crystal structures and other common crystal structures.

4.1 Introduction

Martensitic transformations are commmonly found in many engineering applications today. Evidence of martensitic transforms are present in precipitate hardened alloys [76], shape memory alloys [77, 78], magnetocalorics [79] and self-assembling block copolymers [80]. The phase transformations that occur in these materials are often between two simple crystal structures e.g. face-centered cubic (fcc), body-centered cubic (bcc), hexagonal close-packed (hcp), or body-centered tetragonal (bct). While transformations between simple crystal structures have been described (e.g. Bain path, Burgers path, hcp to ω) [81, 82, 83, 77], few pathways that describe the transformation between a simple crystallographic phase and a topologically complex one have been discovered. One notable exception to this is the discovery of the family of pathways from hcp to the Friauf-Laves

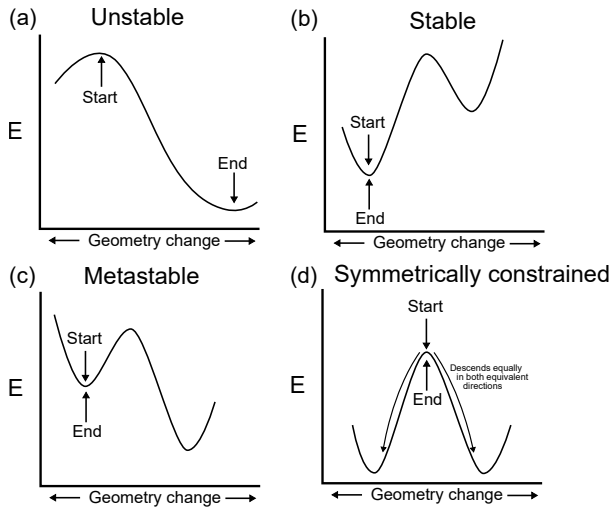

Figure 4.1: DFT calculations used to study transformation pathways can be initialized in an (a) unstable, (b) stable, (c) metastable, or (d) symmetrically constrained state. Scenarios (a) and (d) can result in a discovery of a spontaneous transformation pathway. Symmetrically constrained scenarios must be slightly perturbed in one of the equivalent directions to begin the downward energy trajectory. Otherwise, the geometry will remain in the symmetrically constrained state.

family of intermetallic phases [84]. The lack of simple-to-complex pathways could be because the exact mechanisms of martensitic transformations are often difficult to observe experimentally; however, an energetic pathway that describes the transformation from one phase to the other can be determined using first-principles methods. First-principles methods are particularly helpful because they can be initialized with an arbitrary geometry. An arbitrary initial geometry can correspond to a few characteristic points on the full energy landscape of the material of interest. Figure 4.1 shows 4 different locations on a hypothetical energy landscape at which a density functional theory calculation can be initialized.

Depending on the curvature of the energy landscape, energy minimization routines will either determine the initial geometry is a local minimum in the energy landscape, transform the initial geometry incrementally into a lower energy arrangement of ions, or assert that the initial geometry is too high symmetry to lower its energy in a unique way.

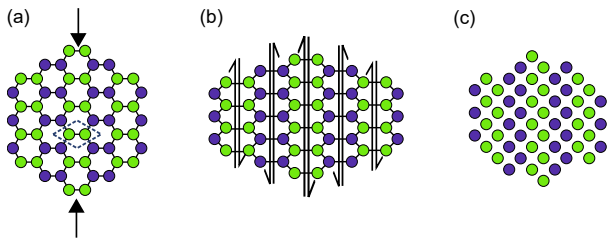

Figure 4.2: A hypothetical pathway from (a) an ordering on a honeycomb layer to (c) an ordering on a square layer. The pathway is broken down into the strain components ((a) to (b)) and the atomic displacement components ((b) to (c)).

The curvature of the energy landscape around an initial geometry is determined by the elements present in the initial geometry. For example, given an arrangement of A and B atoms on a crystalline lattice, one would expect the energy landscape of assigning Mg to A and Al to B to be very different than assigning Ni to A and Nb to B. This result is intuitive because Mg and Al interact differently than Ni and Nb.

Figure 4.2a shows a hypothetical arrangement of atoms on a honeycomb lattice. A choice of which element is assigned to the green atom and the blue atom determines which scenario from Figure 4.1 represents the energy landscape best. If the scenario from Figure 4.1a best represents the energy landscape around the honeycomb structure, the structure could rearrange into the square lattice shown in Figure 4.2c.

Examining prominent crystal structures that have compatible orderings like the hypothetical example in Figure 4.2 can lead to the discovery of important transformation pathways.

4.2 A map of connectivity amongst the most common intermetallic crystal structures

In a previous work [26], we have categorized a large portion of intermetallic crystal structure data present on the Inorganic Crystal Structure Database (ICSD) and the

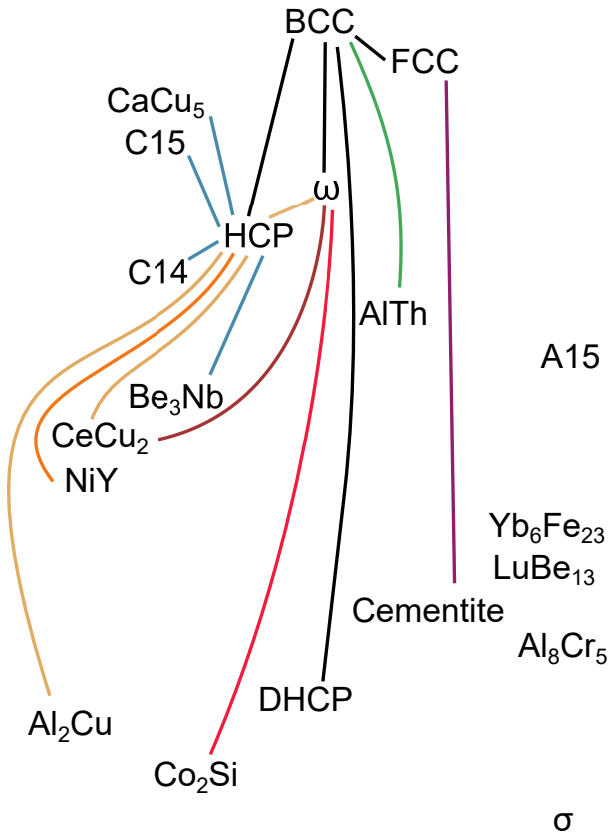

Figure 4.3: The top twenty most common parent crystal structures for intermetallic compounds and how they are connected by transformation pathways. Different colored lines indicate different families of pathways. Parent crystals that are not connected do not currently have a diffusionless transformation pathway to any other parent crystal.

Materials project. This cataloguing of intermetallic crystal structures has allowed us to rank parent crystal structures in order of most commonly observed. Figure 4.3 shows a connectivity graph between the top 20 most frequently seen intermetallic parent crystals where edges between parent crystals represent transformation pathways many of which can happen spontaneously.

Some of these pathways have been described in previous works [81, 82, 83, 77, 84] but those marked in shades of orange, red, green, or purple have been discovered in this study. The transformation pathways described in this work all connect a chemical ordering on a simple parent crystal structure (fcc, bcc, hcp, or ω) to a more complex crystal structure.

It should be noted that not all of the 20 most common intermetallic parent crystals have a facile transformation pathway that links them to a simple parent crystal such as fcc, bcc, hcp, or ω. We believe there is something fundamentally similar between these unconnected parent crystals, but it will require further studies to determine the details of the similarity. In this work, we show the existence of 7 different transformation pathways from designated orderings on simple crystal structures to more complex crystal structures. We summarize which chemistries cause the designated orderings to become dynamically unstable to drive the formation of the complex crystal structure. We also comment on particular interesting alloy systems where experimental corroboration of these transformation pathways is most likely.

4.3 A review of the transformation from hcp to Laves C15

Although the pathway from hcp to Laves C15 has been studied in a previous work, we have decided to reinvestigate the trends presented in Natarajan *et al.* amongst a larger range of the periodic table [84].

Element pairings selected from those highlighted in Figure 4.4 were initialized on the generic A_2B ordering in an $\sqrt{3} \times \sqrt{3}$ supercell of hcp shown in Figure 4.5.

Choosing different elements to place on the A (purple) sublattice and B (orange) sublattice of Figure 4.5, results in varying chemical interactions among the ions. All initial geometries undergo a structural energy minimization using DFT. At the end of the structural energy minimization the resulting geometry is identified. The classification of each final geometry for each choice of elements is shown in Figure 4.6.

For most chemical pairings, the arrangement of atoms on the hcp superstructure is

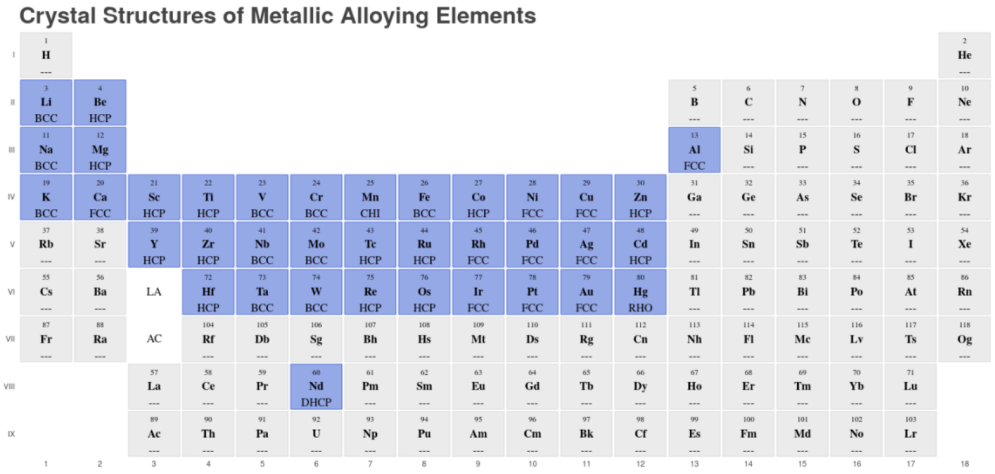

Figure 4.4: The set of elements used for the high-throughput DFT calculations to illuminate transformation pathways in this study are highlighted in blue.

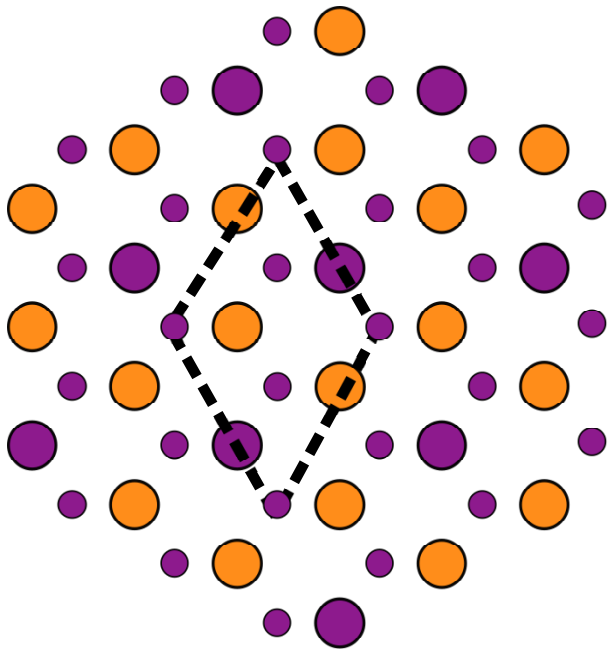

Figure 4.5: A 2D projection of a $\sqrt{3}$ x $\sqrt{3}$ supercell of hcp with composition A_2B and all the B atoms in the $\sqrt{3}$ x $\sqrt{3}$ pattern in one layer. This ordering has the potential to spontaneously transform into Laves C15. Small and large atoms are to distinguish the different layers of hcp while the purple and orange atoms represent the majority and minority elements in the ordering.

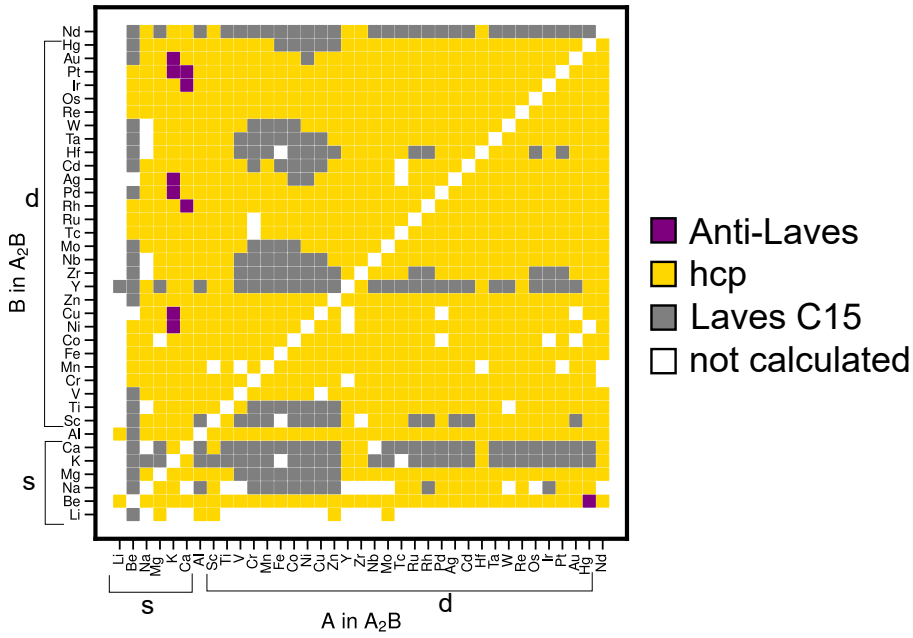

Figure 4.6: A color map representing the final geometries of structural relaxations in DFT for element choices on the ordering in Figure 4.5. The s block metals and d block metals are grouped together. We used Al to represent p block metals and Nd to represent f block metals.

stable. For other pairings, this is not the case and the initial arrangement of atoms as hcp is dynamically unstable. This causes the ions to spontaneously collapse into the Laves C15 crystal structure. In rare scenarios, the dynamically unstable hcp ordering collapsed into a different arrangement of atoms we have called the "anti-Laves" crystal structure. The atomic radius ratio (R_{maj}/R_{min}) and Pauling electronegativity difference (χ_{maj}-χ_{min}) of the chemical pair are highly correlated with the final crystal structure. For radius ratios less than 0.8, it is most likely that the chemical pairing collapsed to Laves C15. It has been seen in other works that a difference in radius can act as a driving force for formation of Laves-like phases [85, 86]. For radius ratios near 1, the initial geometry is likely to remain as hcp. For very large radius ratios and negative electronegativity differences, there is a chance that the initial geometry collapsed to the anti-Laves crystal structure.

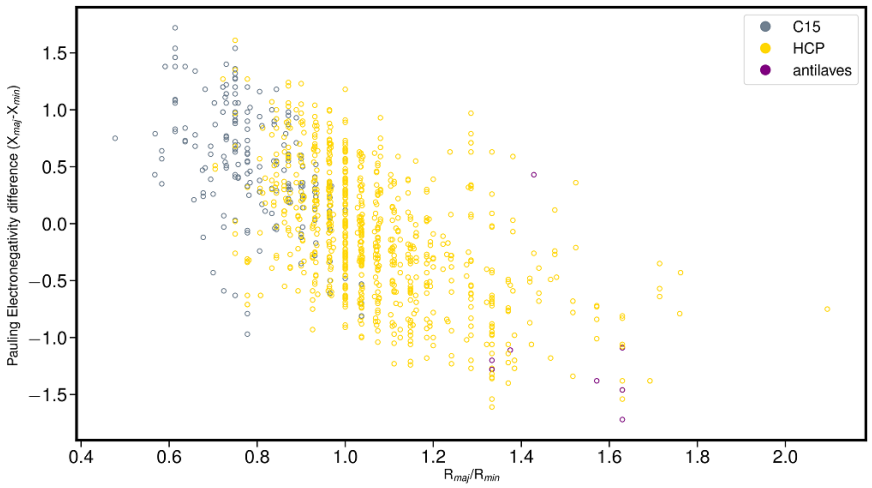

Figure 4.7: The radius ratio and electronegativity difference of various chemistries initialized on a $\sqrt{3}$ x $\sqrt{3}$ supercell of hcp with composition A_2B and all the B atoms in the $\sqrt{3}$ x $\sqrt{3}$ pattern in one layer shown in Figure 4.5. The color coding indicates whether the ions relaxed away from their original position to form Laves C15, remained as hcp, or relaxed to form a phase we have labelled as "anti-Laves"

Figure 4.7 shows the radius ratio vs. electronegativity difference for all compounds initialized on the hcp superstructure colored by final geometry classification. Points of the same classification are clustered in a specific region in the space of radius ratio and electronegativity difference. This clustering is made obvious in Figure 4.8 in which the 2D kernel density estimate of the points is shown to illustrate the shape of each distribution.

If an initial geometry collapses to something other than hcp, it indicates that the resultant phase is relatively more stable than hcp, but it does not guarantee that the resultant phase is stable with respect to all other compounds in the alloy system. In order to measure stability, we have collected the distance to the 0K convex hull for each resultant phase and classifed them by the final geometry. Figure 4.9 shows a normalized histogram of distance to the convex hull of each choice of chemistry. The formation energy data to generate the 0K convex hull was extracted from the Materials Project [3] via pymatgen.

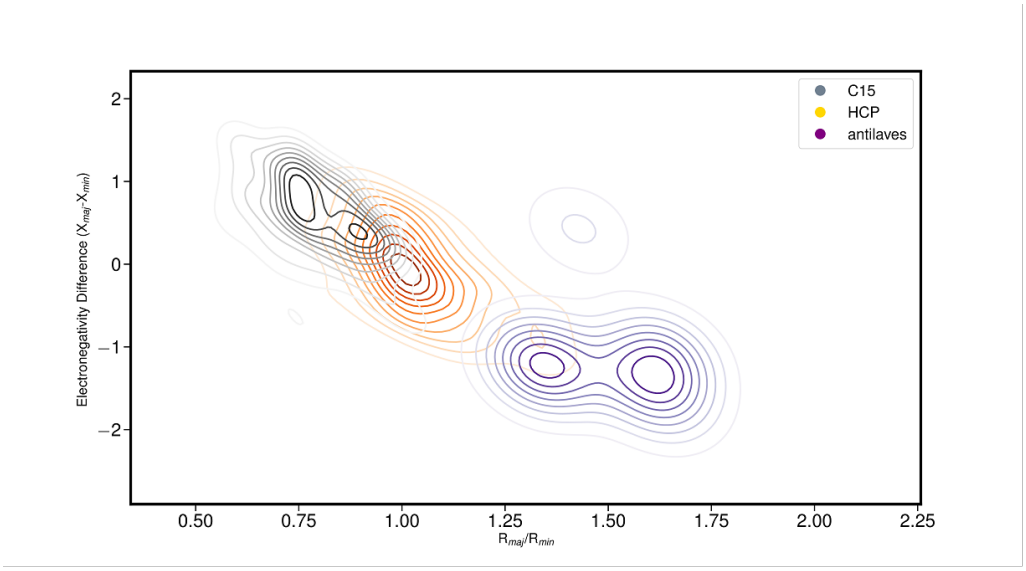

Figure 4.8: The kernel density estimate of the compounds that formed Laves C15, remained as hcp, and formed "anti-Laves". These distributions indicate roughly which radius ratio and electronegativity difference cause the given structure to form from the precursor ordering.

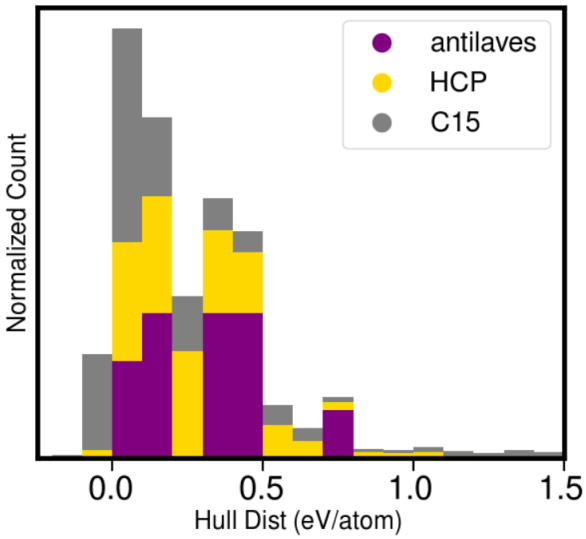

Figure 4.9: The distribution of distance to the convex hull of the compounds that formed Laves C15, remained as hcp, and formed "anti-Laves". These distributions indicate the stability of an ordering relative to other compounds in its respective binary. The convex hull of every binary system is based on the formation energy of compounds calculated on the Materials Project.

Resulting Crystal	# of total chemistries	# observed	# negative hull distance
Anti-Laves	10	0	0
C15	230	50	39
hcp	1048	0	18
other	0	0	0

Table 4.1: A summary of the amount of chemical pairings that remained as hcp, collapsed to "anti-Laves", and collapsed to Laves C15. The second column shows the amount of chemistries that collapsed and are seen experimentally. The third column shows the amount of chemistries that break the 0K convex hull according to energies compiled from the Materials Project i.e. potentially new computational ground states.

Figure 4.9 indicates that there are some choices of chemistry that collapsed to Laves C15 and have a negative hull distance. A negative hull distance implies that this chemistry is more stable than other competing phases in the alloy system of interest that have been calculated by the Materials Project. This indicates that this study may have revealed new ground state structures. A summary of the amount of chemical pairings that remained as hcp, collapsed to the "anti-Laves" crystal structure, and collapsed to Laves C15 is shown in Table 4.1. Table 4.1 also shows the amount of instances where an initial geometry that collapsed to a different structure has been observed experimentally or has a negative hull distance with respect to data on the Materials Project.

The hcp to Laves C15 transformation pathway should serve as a simple example in which a simple structure ordering is decorated with different chemistries and results in 3 potential outcomes. In general, other transformation pathways discovered using this method will not be as simple. In the next section, we show that another ordering on a $\sqrt{3}\times\sqrt{3}$ supercell of hcp results in a more complicated family of transformation pathways.

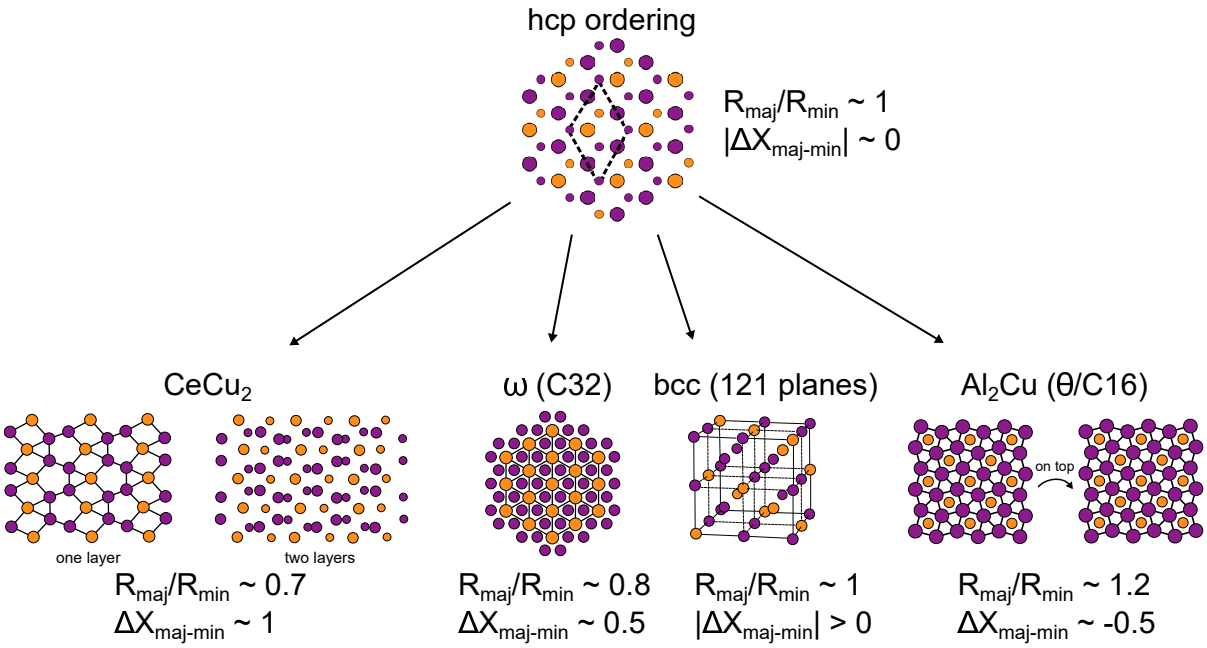

Figure 4.10: The various crystal structures that are transformations of the special $\sqrt{3}$ x $\sqrt{3}$ ordering on hcp. Each of the five crystal structures shown have a different value of radius ratio and Pauling electronegativity difference that promotes its formation. Purple (orange) atoms represent the majority (minority) element. The hcp, $CeCu_2$, ω, and θ structures are 2D projections of the ab-plane. In these pictures, small atoms represent atoms in the layer behind the big atoms.

4.4 A special hcp ordering

Figure 4.10 shows an A_2B chemical ordering on a $\sqrt{3} \times \sqrt{3}$ supercell of hcp that is dynamically unstable to 4 prominent crystal structures depending on choice of chemical decoration.

Element pairings selected from those highlighted in Figure 4.4 were initialized on the hcp ordering in a $\sqrt{3} \times \sqrt{3}$ shown in Figure 4.10. The classification of each final geometry for each choice of elements is shown in Figure 4.11.

The final crystal structure that manifests at the end of the structural energy minimization of this hcp ordering depends on the radius ratio and electronegativity difference of the element on the majority sublattice of the structure and the element on the minority sublattice of the structure. If $R_{maj}/R_{min} \approx 0.7$ and $X_{maj} - X_{min} \approx 1$, then

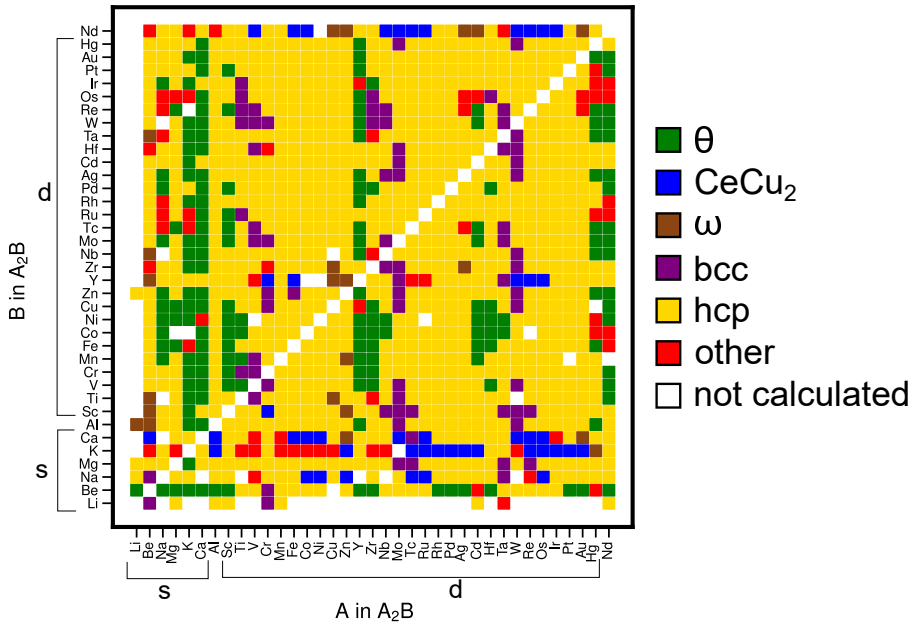

Figure 4.11: A color map representing the final geometries of structural relaxations in DFT for element choices on the hcp ordering in Figure 4.10. The s block metals and d block metals are grouped together. We used Al to represent p block metals and Nd to represent f block metals.

the hcp ordering collapses to the $CeCu_2$-type crystal structure. If $R_{maj}/R_{min} \approx 0.8$ and $X_{maj} - X_{min} \approx 0.5$, then the hcp ordering collapses to the C32 ordering on the ω crystal structure. If $R_{maj}/R_{min} \approx 1$ and $|X_{maj} - X_{min}| > 0$, then the hcp ordering collapses to a (121) plane ordering on the bcc crystal structure. If $R_{maj}/R_{min} \approx 1.2$ and $X_{maj} - X_{min} \approx -0.5$, then the hcp ordering collapses to the C16 ordering on the Al_2Cu-type crystal structure, also referred to as θ in Al-Cu alloy literature [87]. If there is very little difference in radius or electronegativity, then the hcp ordering is likely to remain hcp. These trends are approximate but can be seen in Figure 4.12 when all choices of chemistry are located in radius ratio and electronegativity difference space.

It is important to realize that the hcp ordering could be dynamically unstable towards more than the 4 listed crystal structures. We have collected the final relaxed structures of chemical pairings that do not resemble hcp, bcc, ω, θ, and $CeCu_2$ and grouped them in a category labelled "other." The general shape of the distributions of points can be

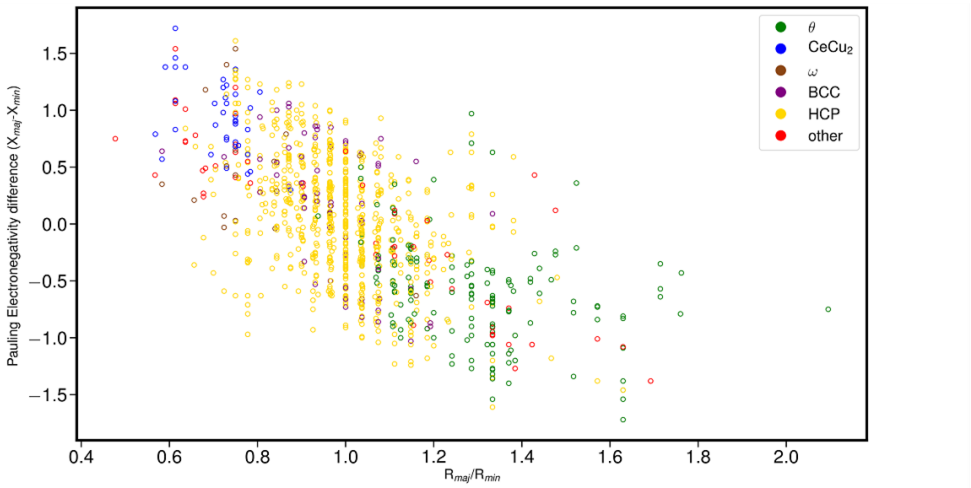

Figure 4.12: The radius ratio and electronegativity difference of various chemistries initialized on a $\sqrt{3}$ x $\sqrt{3}$ supercell of hcp with composition A_2B and one B atom in each layer arranged in the $\sqrt{3}$ x $\sqrt{3}$ pattern shown in Figure 4.10. The color coding indicates whether the ions relaxed away from their original position to form C16 (θ), a bcc 121 plane ordering, ω (C32), the $CeCu_2$ structure, remained as hcp, or relaxed to form a phase other than these.

seen easier in Figure 4.13 where we show the kernel density estimate of the chemistries that formed each final crystal structure.

Figure 4.13 shows that the peak of each distribution is at a different location in radius ratio and electronegativity difference space.

The stability of each collapsed phase across many chemistries is examined by plotting the normalized distribution of distance to the 0K convex hull for each respective alloy system in Figure 4.14. The convex hulls are constructed using the available formation energies of relevant compounds on the Materials Project.

Figure 4.14 shows a select few compounds have negative hull distances with respect to a previously calculated convex hull indicating the potential presence of newly discovered intermetallic ground state structures. A summary of the amount of chemical pairings that collapsed to each crystal structure is shown in Table 4.2. Table 4.2 also shows the amount of instances where an initial geometry that collapsed to a different structure has

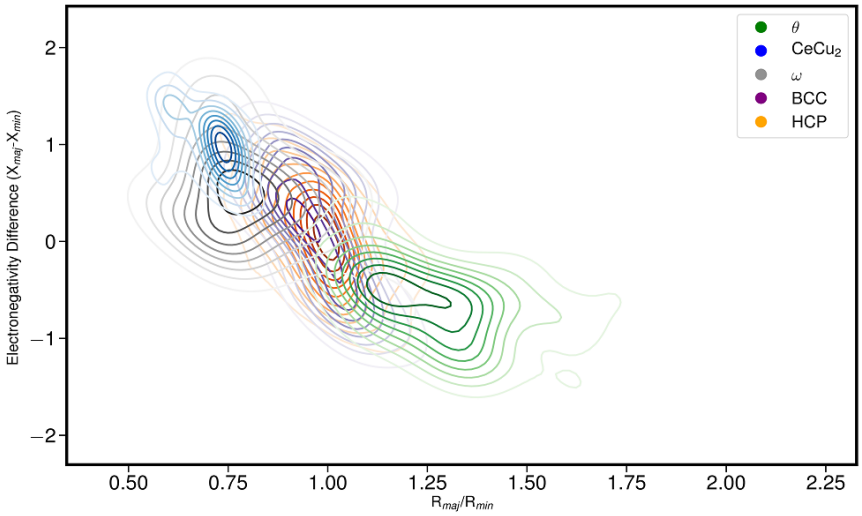

Figure 4.13: The kernel density estimate of the compounds that formed C16 (θ), a bcc 121 plane ordering, ω (C32), the $CeCu_2$ structure, and remained as hcp. These distributions indicate roughly which radius ratio and electronegativity difference cause the given structure to form from the precursor ordering.

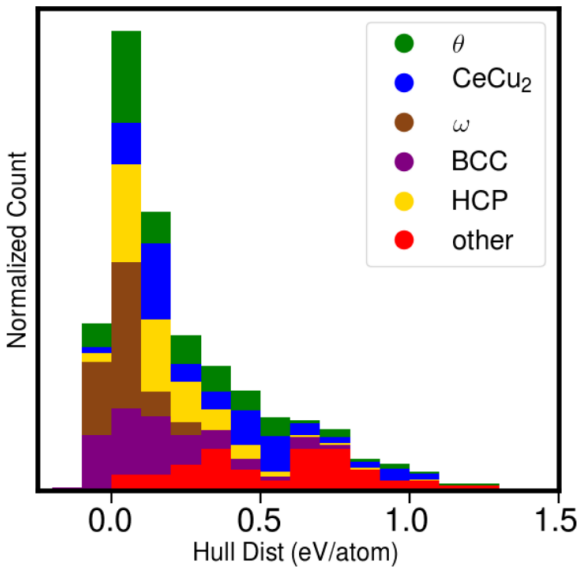

Figure 4.14: The distribution of distance to the convex hull of the compounds that formed C16 (θ), a bcc 121 plane ordering, ω (C32), the $CeCu_2$ structure, and remained as hcp. These distributions indicate the stability of an ordering relative to other compounds in its respective binary. The convex hull of every binary system is based on the formation energy of compounds calculated on the Materials Project.

been observed experimentally or has a negative hull distance with respect to data on the Materials Project.

There are many similarities between the ordering that is dynamically unstable to Laves C15 (Figure 4.5) and the one dynamically unstable to $CeCu_2$ (Figure 4.25). The region of radius ratio and electronegativity difference space for chemistries that collapsed to Laves C15 coincides with that of $CeCu_2$. It is strange that according to the histogram found in Kolli *et al.* [26] Laves C15 is much more common that $CeCu_2$ yet there are very similar precursor hcp orderings that allow for their formation due to the same difference in radius ratio. The reason why Laves C15 is observed more often and is generally more stable across alloy systems than the $CeCu_2$-type structure is an interesting topic for future studies.

Experimental evidence of these transformation pathways is difficult to find as it would require high precision in-situ transmission electron microscopy (TEM) likely with temperature control. Nevertheless, we propose that alloy systems that have a precipitate that corresponds to a phase to which the hcp ordering in Figure 4.10 is dynamically unstable are likely to show evidence of the transformation pathway. In particular, alloy systems in which the majority element's preferred crystal structure is hcp and one of such phases exists as a precipitate. For example, Zr-Fe-Ni alloys, the alloys used in nuclear cladding for boiling water reactors, match both of these criteria [88, 89]. These alloys have a majority composition of Zr which prefers the hcp crystal structure and precipitates that have the Al_2Cu-type (θ) structure that contain Fe and Ni. Orientation relationships imaged between the precipitates and the matrix phase in Zr-Fe-Ni alloys might provide evidence that nucleation of C16 precipitates are driven by the transformation pathway mentioned here [88, 89].

Resulting Crystal	# of total chemistries	# observed	# negative hull distance
bcc	73	0	17
ω	22	1	8
hcp	872	0	35
$CeCu_2$	46	0	1
Al_2Cu	170	5	17
other	59	?	1

Table 4.2: A summary of the amount of chemical pairings that remained as hcp, collapsed to bcc,ω, $CeCu_2$, Al_2Cu (θ), or another structure. The second column shows the amount of chemistries that collapsed and are seen experimentally. The third column shows the amount of chemistries that break the 0K convex hull according to energies compiled from the Materials Project i.e. potentially new computational ground states.

4.5 The pathway from hcp to NiY

There is an AB ordering on a rectangular supercell of hcp that is dynamically unstable to the NiY-type crystal structure and some other phases. A depiction of this special ordering is shown in Figure 4.15.

An AB ordering has no majority or minority sublattice so the methods used in the previous sections for determining chemical combinations, radius ratio, and electronegativity differences needed to be adjusted. Unique pairs of elements (order does not matter) were selected from Figure 4.4 and decorated on the ordering in Figure 4.15 with one element on the purple sites and the other on the orange sites. Structural energy minimization was performed on these initial geometries using DFT. The classification of each final geometry for each choice of elements is shown in Figure 4.16.

The class of the resulting structures were plotted in radius ratio and electronegativity difference space such that radius ratio is now always >= 1 (R_{big}/R_{small}). The electronegativity difference is now an absolute difference such that $\Delta X = |X_{big} - X_{small}|$. The distribution of chemistries in radius ratio and electronegativity difference space is shown in Figure 4.17.

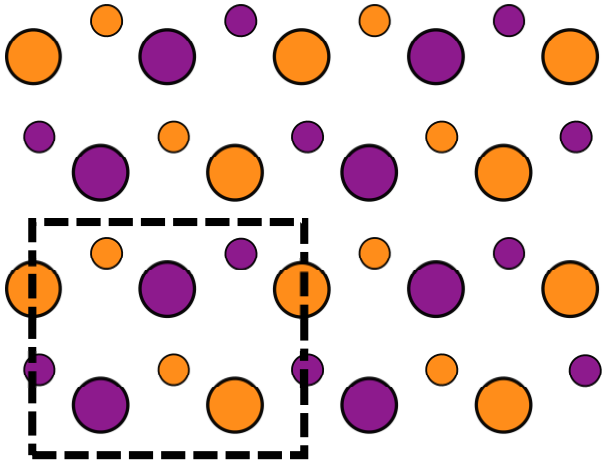

Figure 4.15: A 2D projection of a rectangular supercell of hcp with composition AB and a staggered zigzag ordering. This ordering has the potential to spontaneously transform into the NiY structure. Small and large atoms are to distinguish the different layers of hcp while the purple and orange atoms represent the majority and minority elements in the ordering in this case they are equivalent.

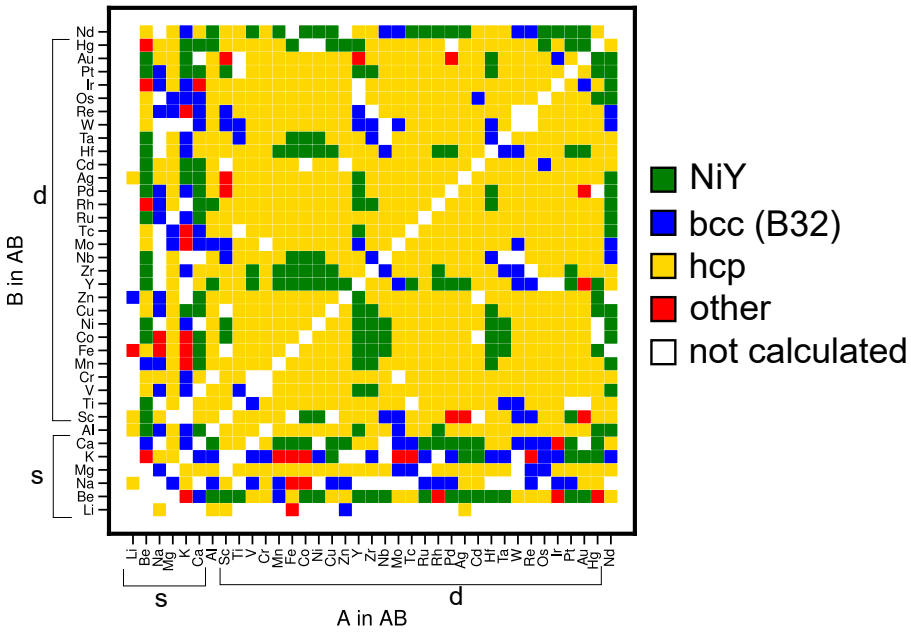

Figure 4.16: A color map representing the final geometries of structural relaxations in DFT for element choices on the hcp ordering in Figure 4.15. The s block metals and d block metals are grouped together. We used Al to represent p block metals and Nd to represent f block metals.

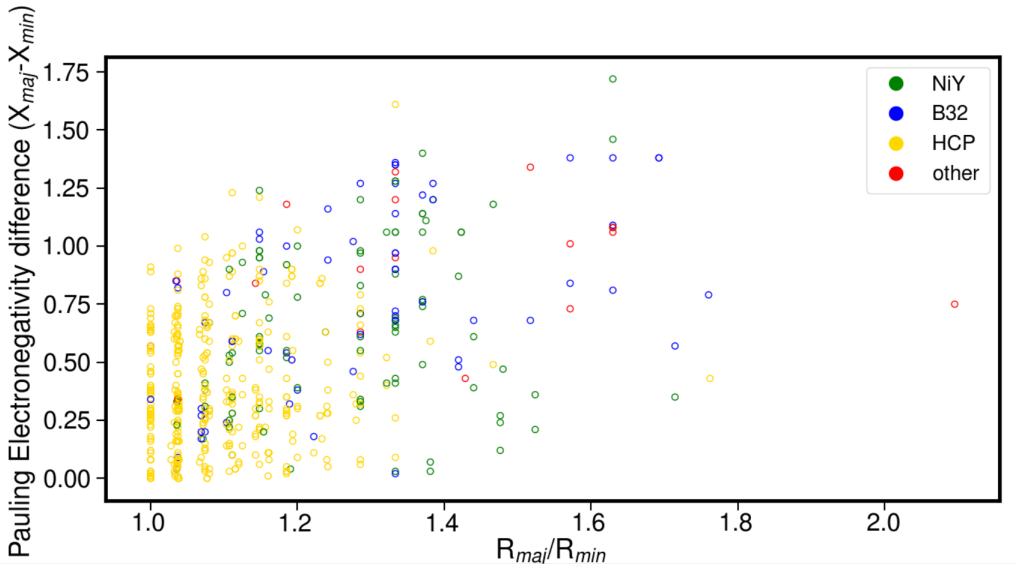

Figure 4.17: The radius ratio and electronegativity difference of various chemistries initialized on a rectangular supercell of hcp with composition AB and a staggered zigzag ordering shown in Figure 4.15. The color coding indicates whether the ions relaxed away from their original position to form the NiY structure, a BCC ordering (B32), remained as hcp, or relaxed to form a phase other than these.

The separation of different final structures in this space is not as clear as in previous sections with the hcp to Laves C15 and hcp to Al_2Cu pathways. This is made apparent in the kernel density estimates of the data distributions shown in Figure 4.18.

The distributions of the bcc ordering B32 and NiY have significant overlap, although the peak for both of these distributions is shifted to higher radius ratios than that of the structures that remained as the hcp ordering.

The stability of the collapsed structures is shown in Figure 4.19 by examining the distribution of distance from the 0K convex hull based on relevant structures found on the Materials Project. A significant portion of compounds that collapsed to the NiY-type structure have low or negative hull distances showing that NiY-type structures are energetically competitive phases in many alloy systems. A summary of the amount of chemical pairings that collapsed to each crystal structure is shown in Table 4.3. Table 4.3 also shows the amount of instances where an initial geometry that collapsed to a different

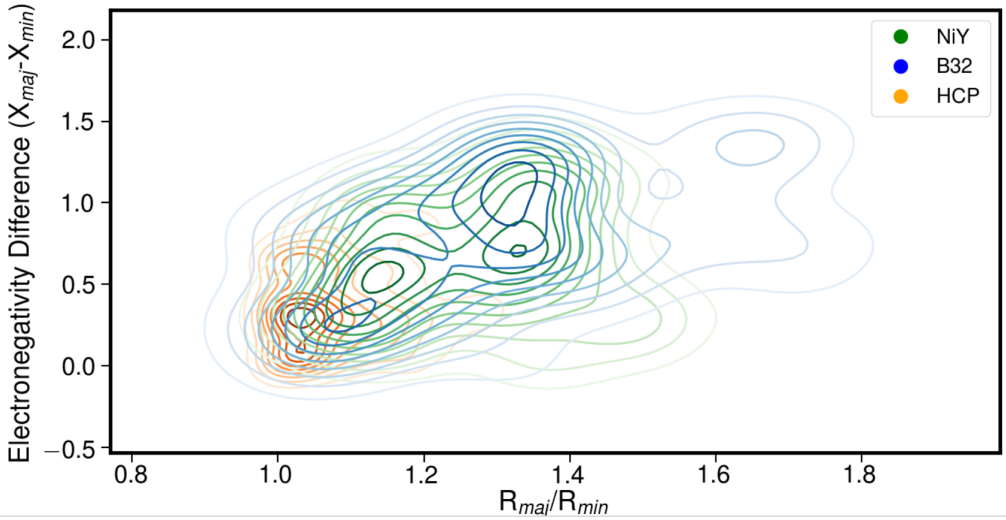

Figure 4.18: The kernel density estimate of the compounds that formed the NiY structure, a BCC ordering (B32), and remained as hcp. These distributions indicate roughly which radius ratio and electronegativity difference cause the given structure to form from the precursor ordering.

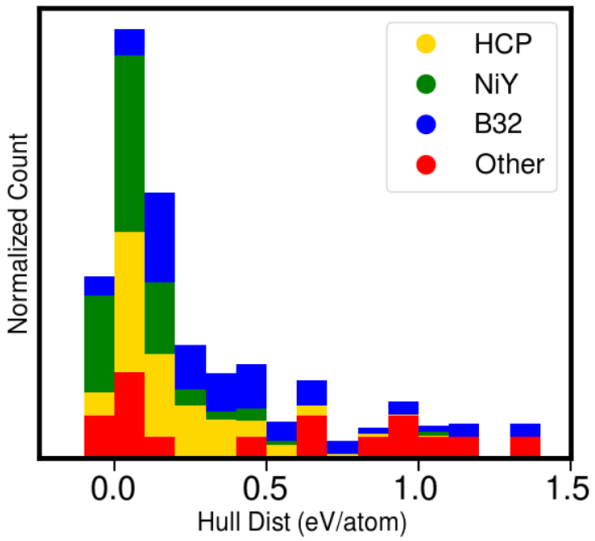

Figure 4.19: The distribution of distance to the convex hull of the compounds that formed the NiY structure, a bcc ordering (B32), and remained as hcp. These distributions indicate the stability of an ordering relative to other compounds in its respective binary. The convex hull of every binary system is based on the formation energy of compounds calculated on the Materials Project.

Resulting Crystal	# of total chemistries	# observed	# negative hull distance
NiY	98	4	26
B32	61	1	4
hcp	407	0	25
other	19	?	3

Table 4.3: A summary of the amount of chemical pairings that remained as hcp, collapsed to bcc ordering B32,the NiY-type structure, or another structure. The second column shows the amount of chemistries that collapsed and are seen experimentally. The third column shows the amount of chemistries that break the 0K convex hull according to energies compiled from the Materials Project i.e. potentially new computational ground states.

structure has been observed experimentally or has a negative hull distance with respect to data on the Materials Project.

4.6 The pathway from $L1_2$ to cementite ($D0_{11}$)

In this work, we searched for orderings on simple crystal structures that are dynamically unstable for certain chemistries. If the ordering is low enough symmetry, initializing a geometry with a specific chemical choice is enough to start the structural energy minimization to the lower energy structure. Occasionally, the ordering on the simple crystal structure has high enough symmetry such that we get a scenario shown in Figure 4.1d. In these instances, we linearly interpolate between the geometries of the simple ordering and the expected endpoint. We apply a slight distortion along this path to move the starting geometry for the minimization off of the high symmetry point in the energy landscape. This way the energy minimization routines have a unique downhill direction to move towards.

We have performed these steps on a $\sqrt{2} \times \sqrt{2} \times 2$ square supercell of the $L1_2$ ordering on fcc. The supercell of $L1_2$ is shown in Figure 4.20.

After applying the slight geometric perturbation in the direction of cementite ($D0_{11}$),

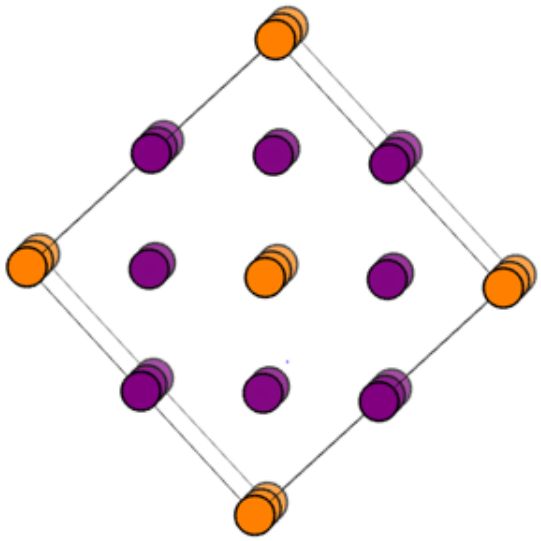

Figure 4.20: A perspective view of square supercell of the $L1_2$ ordering on fcc with composition A_3B. This ordering has the potential to spontaneously transform into the cementite ($D0_{11}$) structure. The purple and orange atoms represent the majority and minority elements in the ordering.

we initialized the geometry with chemical pairings from Figure 4.4 and conducted structural energy minimization using DFT. The classification of each final geometry for each choice of elements is shown in Figure 4.21.

The results of these calculations show that, similarly to the hcp to Al_2Cu pathway, there is a correlation of radius ratio to the structures that collapse to cementite ($D0_{11}$). The classification data plotted in radius ratio and electronegativity difference space is shown in Figure 4.22.

There is a cluster of points that collapsed to cementite at $R_{maj}/R_{min} \approx 1.35$. The cluster becomes more clear when examining the kernel density estimates in Figure 4.23. The peak and spread of the cementite distribution has minimal overlap with the $L1_2$ distribution. The stability of cementite in alloy systems can be examined in the distribution of hull distances shown in Figure 4.24.

A summary of the amount of chemical pairings that collapsed to each crystal structure

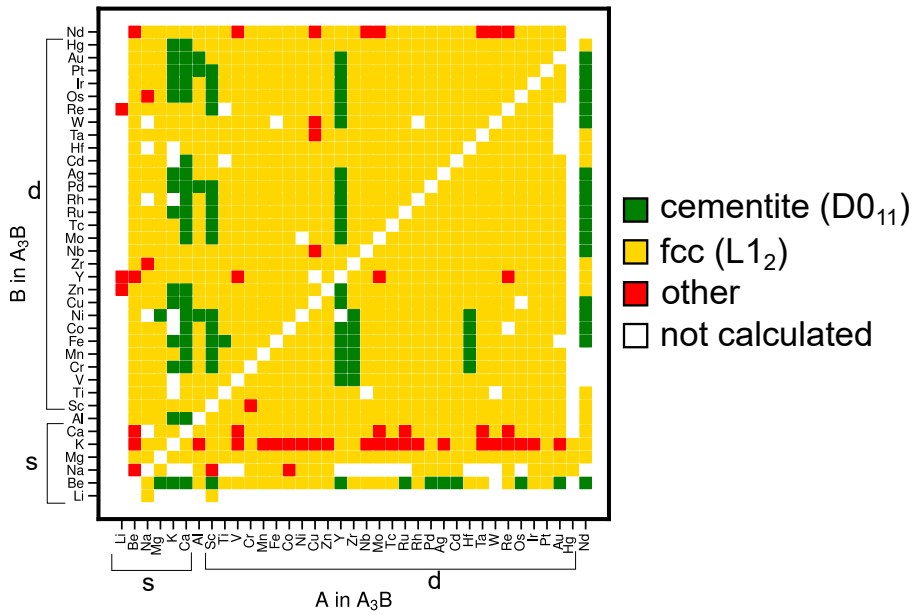

Figure 4.21: A color map representing the final geometries of structural relaxations in DFT for element choices on the supercell of $L1_2$ in Figure 4.20. The s block metals and d block metals are grouped together. We used Al to represent p block metals and Nd to represent f block metals.

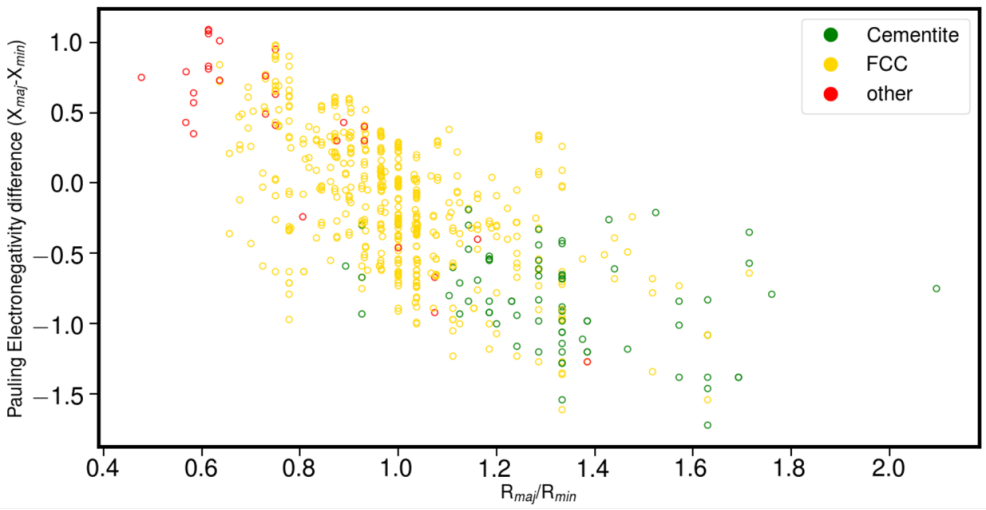

Figure 4.22: The radius ratio and electronegativity difference of various chemistries initialized on a square supercell of the $L1_2$ ordering with composition A_3B shown in Figure 4.20. The color coding indicates whether the ions relaxed away from their original position to form the cementite ($D0_{11}$) structure, remained as $L1_2$, or relaxed to form a phase other than these.

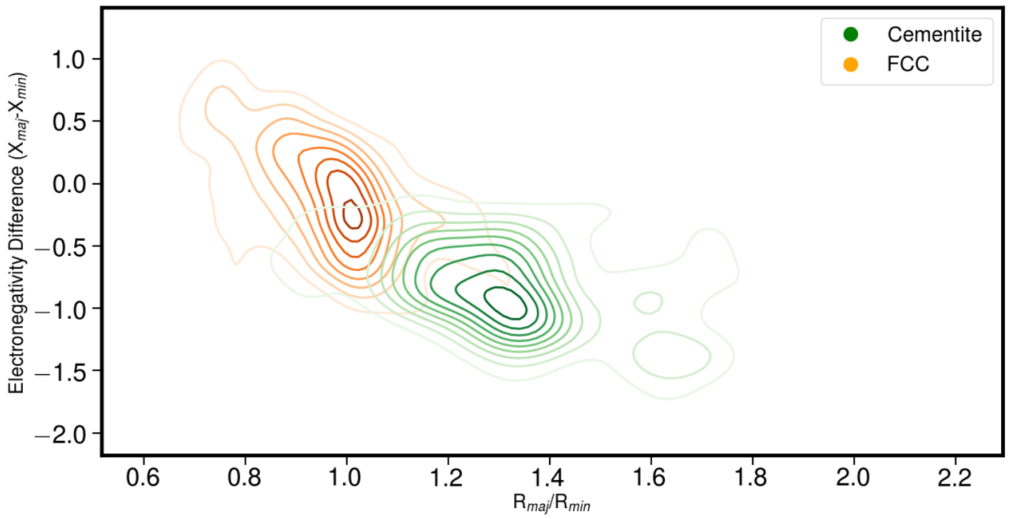

Figure 4.23: The kernel density estimate of the compounds that formed the cementite ($D0_{11}$) structure and remained as $L1_2$. These distributions indicate roughly which radius ratio and electronegativity difference cause the given structure to form from the precursor ordering.

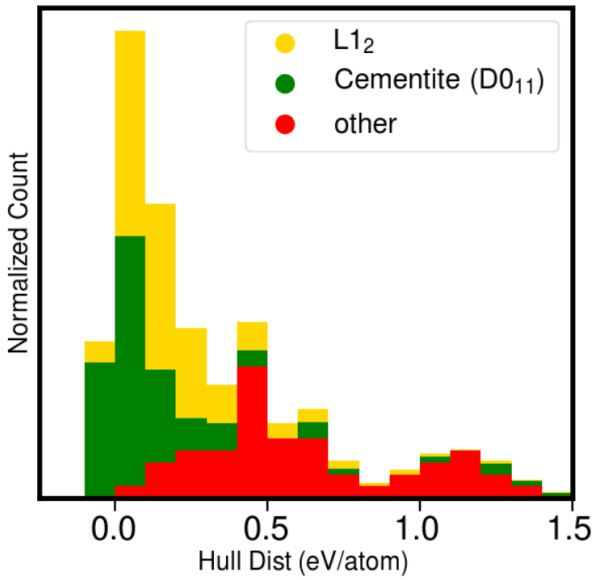

Figure 4.24: The distribution of distance to the convex hull of the compounds that formed the cementite ($D0_{11}$) structure and remained as $L1_2$. These distributions indicate the stability of an ordering relative to other compounds in its respective binary. The convex hull of every binary system is based on the formation energy of compounds calculated on the Materials Project.

Resulting Crystal	# of total chemistries	# observed	# negative hull distance
fcc $L1_2$	1023	88	46
cementite $D0_{11}$	112	7	26
other	51	?	0

Table 4.4: A summary of the amount of chemical pairings that remained as $L1_2$, collapsed to cementite ($D0_{11}$), or another structure. The second column shows the amount of chemistries that collapsed and are seen experimentally. The third column shows the amount of chemistries that break the 0K convex hull according to energies compiled from the Materials Project i.e. potentially new computational ground states.

is shown in Table 4.4. Table 4.4 also shows the amount of instances where an initial geometry that collapsed to a different structure has been observed experimentally or has a negative hull distance with respect to data on the Materials Project.

This pathway is particularly interesting to examine in the case of the Ni-Al binary alloy system. Ni-Al is one of the few alloy systems (Pt-Y and Pd-Y also) that contains $L1_2$ as a ground state on one side (Ni-rich) of the phase diagram and cementite ($D0_{11}$) as a ground state on the other (Al-rich) side [66]. Additionally, the elemental crystal structures of both Ni and Al are fcc. This makes temporary local regions of the $L1_2$ ordering more likely on both sides of the phase diagram. $L1_2$ is a prominent ordering in many fcc alloys due to its high symmetry and simple interaction parameters (Al-Al repulsion drives formation). In most $L1_2$ orderings, the minority element has a slightly larger atomic radius than that of the majority element [26]. In cementite structures, the opposite is the case. We hypothesize that on the Al-rich side of the Ni-Al phase diagram cementite is a stable ground state due to this radius difference ($r_{Al} > r_{Ni}$). According to the calculations performed here, the radius difference makes Al_3Ni $L1_2$ dynamically unstable to the Al_3Ni cementite structure.

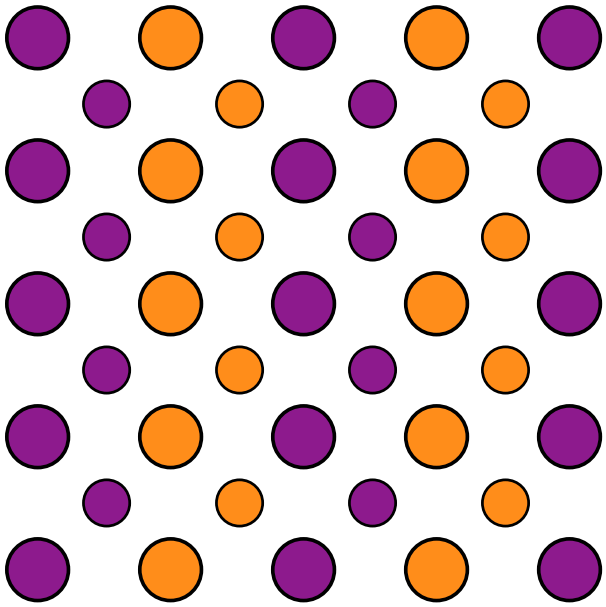

Figure 4.25: A 2D projection of the B11 ordering on bcc with composition AB. This ordering has the potential to spontaneously transform into the AlTh (B33) structure. The small and large atoms represent the body centers and the corner atoms while the purple and orange atoms represent the majority and minority elements in the ordering, in this case they are equivalent.

4.7 The pathway from B11 to AlTh (B33)

Another precursor ordering that needs to perturbed from a high symmetry starting configuration is the bcc ordering B11. The B11 ordering is shown in Figure 4.25.

A perturbation is made along a linearly interpolated path to the AlTh (B33) structure before beginning the structural energy minimization. The classification of each final geometry for each choice of elements is shown in Figure 4.26.

The results of the calculations are shown in radius ratio and electronegativity difference space in Figure 4.27.

Because the B11 ordering is an AB ordering like NiY, the adjusted radius ratio and electronegativity difference definitions are used here as well. Figure 4.27 shows a large portion of the calculations did not collapse to AlTh (B33) or remain as B11, most of which contain K, Y, Zr, Cd, Hg, or Nd.

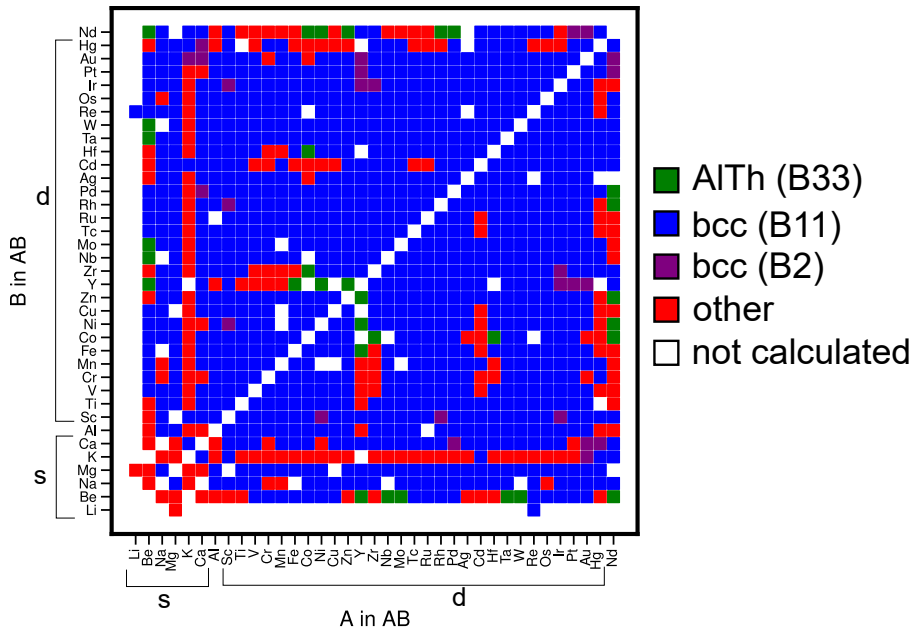

Figure 4.26: A color map representing the final geometries of structural relaxations in DFT for element choices on the B11 ordering in Figure 4.25. The s block metals and d block metals are grouped together. We used Al to represent p block metals and Nd to represent f block metals.

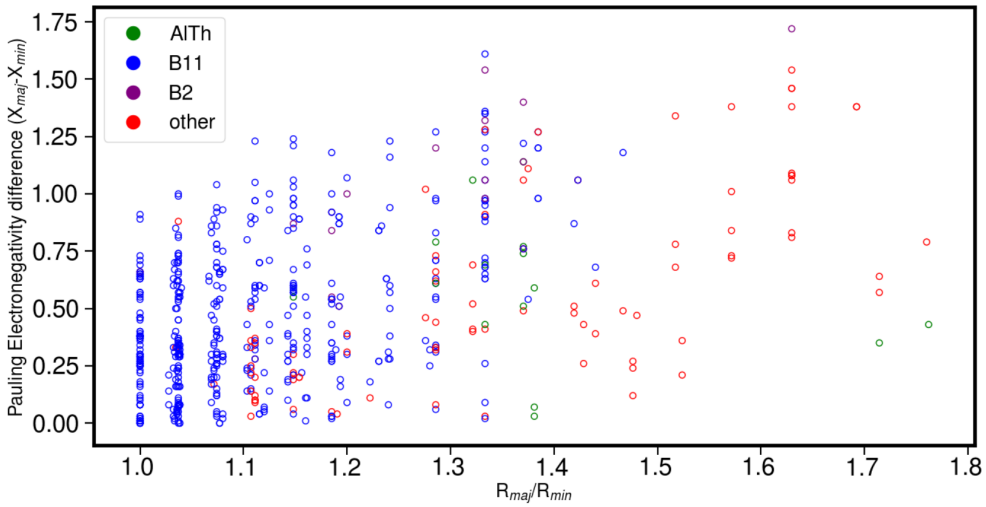

Figure 4.27: The radius ratio and electronegativity difference of various chemistries initialized on the bcc ordering B11 with composition AB shown in Figure 4.25. The color coding indicates whether the ions relaxed away from their original position to form the AlTh (B33) structure, B2, remained as B11, or relaxed to form a phase other than these.

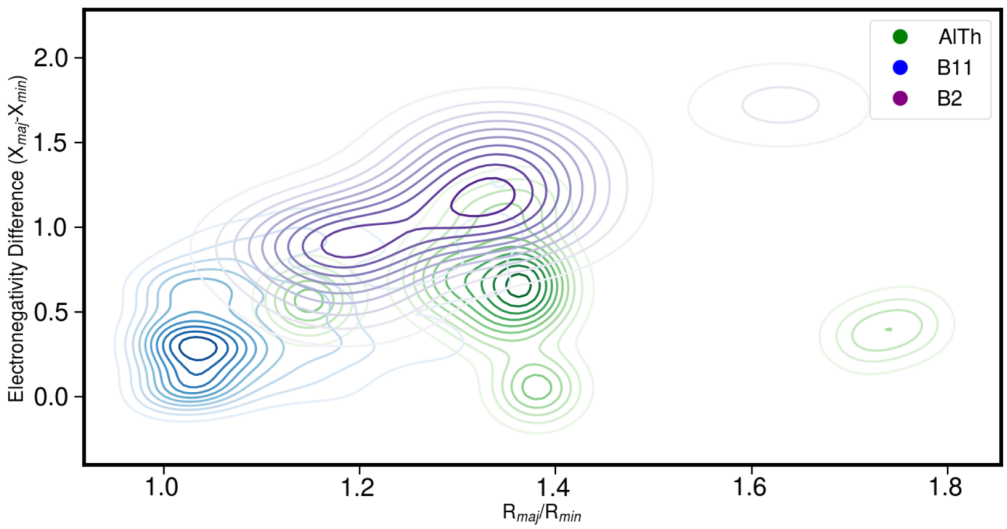

Figure 4.28: The kernel density estimate of the compounds that formed the AlTh (B33) structure, remained as B11 and ones that formed B2. These distributions indicate roughly which radius ratio and electronegativity difference cause the given structure to form from the precursor ordering.

Figure 4.28 shows the distributions of B11 and B33 have very little overlap.

B33 seems to be preferred when the radius ratio R_{big}/R_{small} is around 1.35. The stability of AlTh (B33) is highlighted in Figure 4.29 when examined the distribution of hull distances for the calculations. The perturbed B11 ordering is dynamically unstable to other crystal structures many of which are only metastable.

Although there are not many chemical pairings that collapsed to AlTh, those that did have low hull distances (less than 100meV) which indicates competitive stability to relevant phases. A summary of the amount of chemical pairings that collapsed to each crystal structure is shown in Table 4.5. Table 4.5 also shows the amount of instances where an initial geometry that collapsed to a different structure has been observed experimentally or has a negative hull distance with respect to data on the Materials Project.

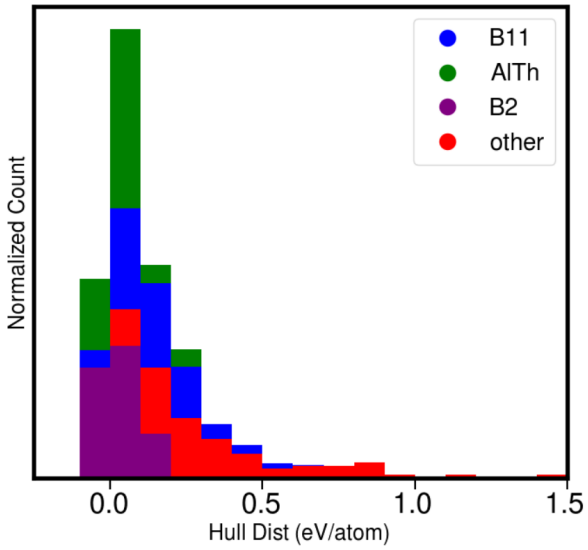

Figure 4.29: The distribution of distance to the convex hull of the compounds that formed the AlTh (B33) structure, remained as B11 and ones that formed B2. These distributions indicate the stability of an ordering relative to other compounds in its respective binary. The convex hull of every binary system is based on the formation energy of compounds calculated on the Materials Project.

Resulting Crystal	# of total chemistries	# observed	# negative hull distance
B11	485	4	33
AlTh(B33)	16	0	5
B2	13	9	5
other	95	?	0

Table 4.5: A summary of the amount of chemical pairings that remained as bcc ordering B11, collapsed to AlTh (B33), B2, or another structure. The second column shows the amount of chemistries that collapsed and are seen experimentally. The third column shows the amount of chemistries that break the 0K convex hull according to energies compiled from the Materials Project i.e. potentially new computational ground states.

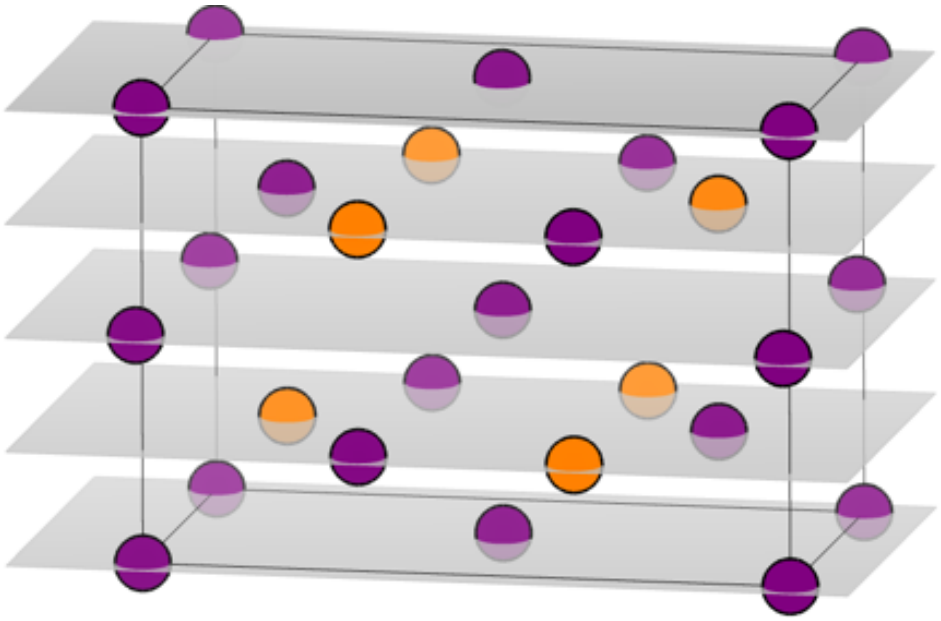

Figure 4.30: A perspective view of a rectangular supercell of the $B8_2$ ordering on ω with composition A_2B. This ordering has the potential to spontaneously transform into the Co_2Si (C37) structure. The purple and orange atoms represent the majority and minority elements in the ordering.

4.8 The pathway from ω $B8_2$ to Co_2Si (C37)

The pathways mentioned in the previous sections all begin on a chemical ordering on a traditionally simple crystal structure fcc, bcc, or hcp. While not traditionally thought of as a common simple crystal structure, the ω crystal has only a 3 atom basis and hexagonal symmetry, making it only slightly more complicated than hcp. We examine a pathway from a well-known A_2B chemical ordering on ω, $B8_2$, to the complex crystal structure of Co_2Si (C37). A rectangular supercell of the $B8_2$ ordering on ω in shown in Figure 4.30.

A slight perturbation in the direction of C37 is made on this supercell before the structural energy minimization begins. The classification of each final geometry for each choice of elements is shown in Figure 4.31.

The results of all potential chemical pairs from Figure 4.4 are shown in radius ratio

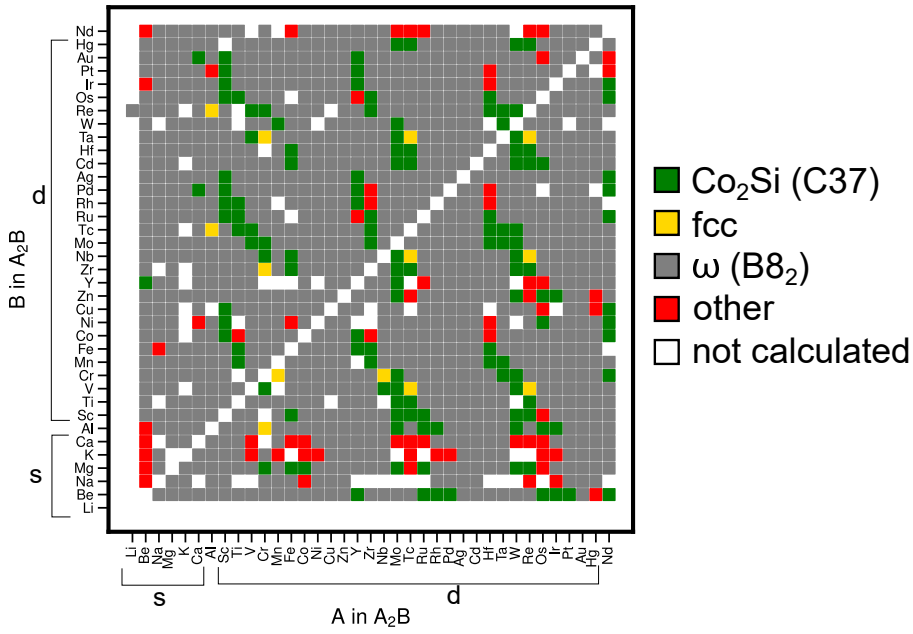

Figure 4.31: A color map representing the final geometries of structural relaxations in DFT for element choices on the supercell of the $B8_2$ ordering in Figure 4.30. The s block metals and d block metals are grouped together. We used Al to represent p block metals and Nd to represent f block metals.

and electronegativity difference space in Figure 4.32.

Figure 4.32 makes it apparent that radius ratio and electronegativity difference are not helpful features to distinguish which final crystal structure is most likely. Figure 4.33 reiterates this point showing that the distributions of Co_2Si, fcc, and $B8_2$ overlap heavily in this feature space. This indicates there must be some other driving force that causes Co_2Si (C37) to form instead of remaining as $B8_2$.

Figure 4.34 shows the stability of the collapsed phases as a distribution of hull distances over the compounds respective alloy systems.

A summary of the amount of chemical pairings that collapsed to each crystal structure is shown in Table 4.6. Table 4.6 also shows the amount of instances where an initial geometry that collapsed to a different structure has been observed experimentally or has a negative hull distance with respect to data on the Materials Project.

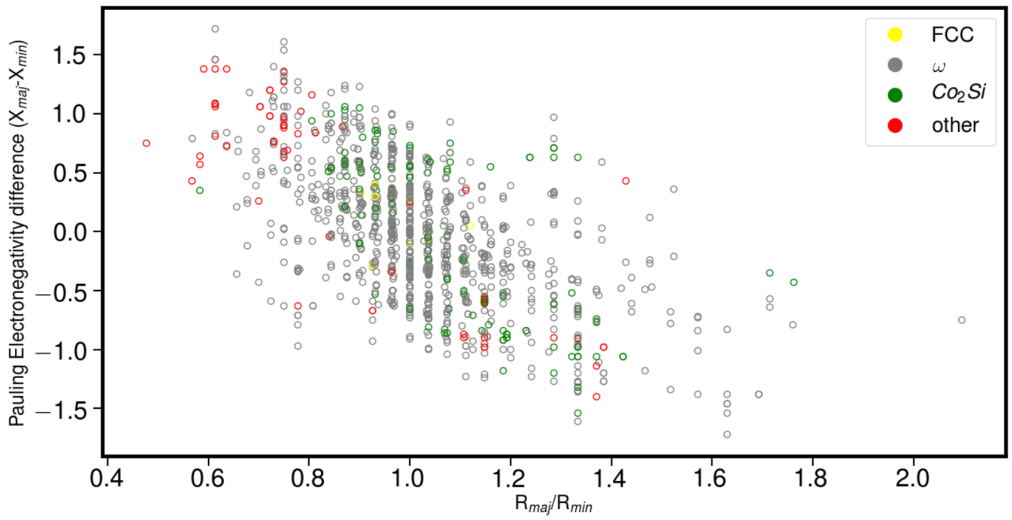

Figure 4.32: The radius ratio and electronegativity difference of various chemistries initialized on a volume 2 rectangular supercell of the ω ordering $B8_2$ with composition A_2B shown in Figure 4.30. The color coding indicates whether the ions relaxed away from their original position to form the Co_2Si (C37) structure, an fcc ordering, remained as $B8_2$, or relaxed to form a phase other than these.

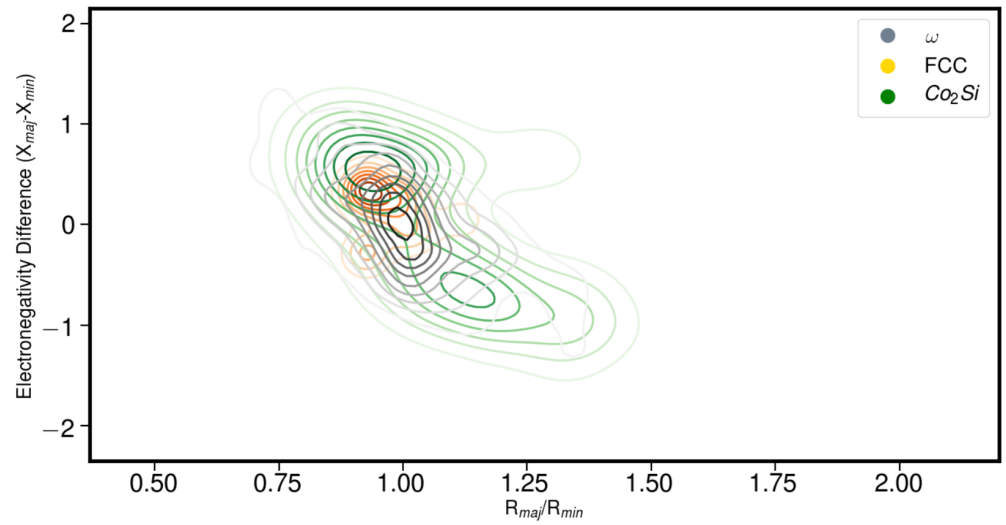

Figure 4.33: The kernel density estimate of the compounds that formed the Co_2Si (C37) structure, an fcc ordering, and remained as $B8_2$. These distributions indicate roughly which radius ratio and electronegativity difference cause the given structure to form from the precursor ordering.

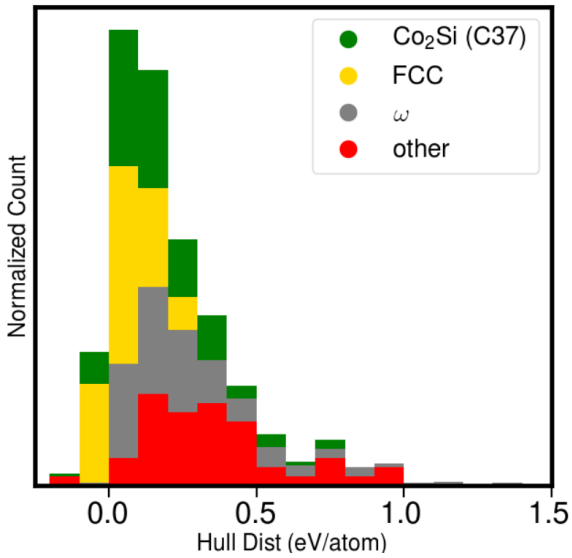

Figure 4.34: The distribution of distance to the convex hull of the compounds that formed the the Co_2Si (C37) structure, an fcc ordering, and remained as $B8_2$. These distributions indicate the stability of an ordering relative to other compounds in its respective binary. The convex hull of every binary system is based on the formation energy of compounds calculated on the Materials Project.

Resulting Crystal	# of total chemistries	# observed	# negative hull distance
ω $B8_2$	971	4	7
Co_2Si (C37)	136	2	12
fcc	13	0	3
other	65	?	6

Table 4.6: A summary of the amount of chemical pairings that remained as ω ordering $B8_2$, collapsed to Co_2Si (C37), an fcc ordering, or another structure. The second column shows the amount of chemistries that collapsed and are seen experimentally. The third column shows the amount of chemistries that break the 0K convex hull according to energies compiled from the Materials Project i.e. potentially new computational ground states.

4.9 Discussion and Conclusion

To our knowledge, before this work 9 of the top 20 most common intermetallic crystal structures were connected via known structural transformation pathways. In this study, we show the existence of pathways to 6 more of the top 20 most common crystal structures. The pathways begin from 5 special orderings on simple crystal structures fcc, bcc, hcp, and ω. Each of these orderings are dynamically unstable to another crystal structure in the top 20 most common crystal structures given a certain choice of elements to decorate the ordering. This dynamic instability indicates these transformations can happen spontaneously and martensitically. In some cases, the atomic radius ratio or the Pauling electronegativity difference of the elements chosen is a strong indicator of whether or not the special precursor ordering will collapse into a different crystal structure. In other cases, strong overlaps of distributions in radius ratio and electronegativity difference feature space indicate that there is another quantity that differentiates the formation of one crystal structure over another.

When comparing energies of collapsed crystal structures to existing calculated phase diagrams, we find that some of these collapsed phases could potentially be newly discovered ground state compounds. Some of the structures marked as new ground states relative to the energy data on the Materials project have already been calculated by the Open Quantum Materials Database (OQMD) and designated as ground states [90, 91]. We believe that OQMD also shows evidence of these spontaneous martensitic transformation pathways because some structures labelled as hcp superstructures are structurally closer to the NiY-type structure. This high-throughput DFT study has also brought to our attention the striking energetic and structural similarity between the NiY-type crystal structure and the AlTh (B33) crystal structure. The local bonding behavior of each of these structures is very similar but the long range connectivity and symmetry

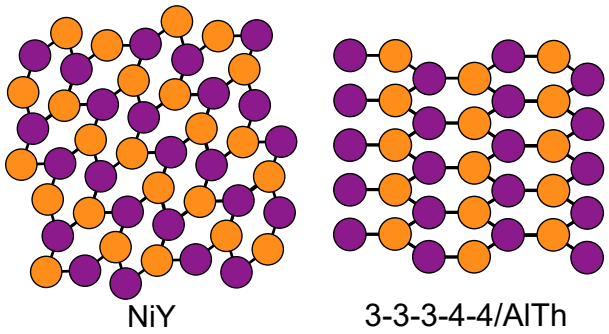

Figure 4.35: Single layers of the NiY-type structure and the AlTh-type (B33) structure. In both structures, Y-shaped patterns are seen and connected to form squished hexagons. The type of each atom alternates along the Y-shaped path. The B33 structure has more regularity in the bonding at larger distances when compared to NiY.

differs as seen in Figure 4.35.

In many alloy systems these two phases are competing with each other for stability often differing in energy by less than 100 meV per atom [90, 91].

Experimental evidence to verify the existence of these pathways is most likely obtained through high-resolution in-situ transmission electron microscopy with temperature control. Systems that can spontaneously form small areas of the dynamically unstable precursor ordering might have this critical region transform into a different crystal structure via one of the reported pathways. If this evidence is collected, it shows that the types of transformation pathways presented here can be mechanisms for nucleation of secondary precipitate phases in alloy synthesis and aging. We draw attention to the Ni-Al and Zr-Fe-Ni alloy systems because they have the ability to form pockets of their respective precursor orderings on the elemental crystal structure of the Al-rich and Zr-rich side of the phase diagrams. Orientation relationships between precipitates and matrix phases should be examined to see if interfaces occur along the high order planes that cause the dynamic instability. It is interesting to think whether these transformation pathways from dynamically unstable orderings on simple crystal structures is what causes the resulting collapsed structures to be observed so frequently in nature. The methods used

in this work led to the discovery of many new transformation pathways that deepen the understand of crystallographic relationships. With extended time and effort, we believe these methods can broaden the types of martensitic transforms that are used in technology today. For example, these pathways could promote nucleation of certain hardening phases to control the type of precipitates that form in structural alloys.

4.10 Computational Methods

Density Functional Theory (DFT) as parametrized by Perdew Burke and Ernzerhof (PBE) [15] was used to conduct structural energy minimization of various alloy orderings and chemical pairings. Projector augmented wave (PAW) [16, 92] theory was used to approximate the core electrons. DFT calculations were performed using the Vienna ab-initio software package (VASP) [14, 13]. Plane-wave cutoff energies of 550 eV were used for calculations with a k-point density of 60 Å. We believe PBE with this cutoff energy and k-point density was sufficiently accurate because these calculations accurately predict the correct ground state structures in many of the tested alloy systems. The formation energies of structures in each alloy system used in this study were extracted from the Materials Project using the pymatgen interface. Formation energies were calculated for each compound in this study by calculating all the elemental ground states with the same VASP parameters mentioned above and using the appropriate energies as references.

4.10.1 Determining precursor orderings

Precursor orderings were determined using the mapping algorithm implemented in the CASM code suite described in Chapter 2 [69, 26]. For each crystal structure in the top 20 most common crystal structures we mapped the most common chemical ordering onto the 4 simple crystal structures fcc, bcc, hcp, and ω. While the mapping scores are often large,

the CASM code suite provides the chemical configuration that minimizes the score, i.e. the closest ordering on the simple crystal to the crystal structure of interest. The closest ordering on the simple crystal structure with the minimum mapping score was designated as the trial precursor ordering. A small set of chemistries that were known to form the resultant crystal structure were initialized on the simple crystal structure ordering to determine if it was dynamically unstable. If the closest ordering had particularly high symmetry, it was slightly perturbed towards the resulting crystal structure to prevent the structural relaxation from being constrained to the initial geometry. While these pathways were constructed with one endstate in mind, it was often the case that the precursor ordering was dynamically unstable to multiple crystal structures. In order to determine which other crystal structures appeared, we used the mapping algorithm to group structures together and compare them to a set of known reference structures to identify them.

Chapter 5

The thermodynamic properties of spinel intercalation compounds

[1]

5.1 Introduction

Spinel intercalation compounds such as $LiMn_2O_4$ and $LiTi_2O_4$ exhibit exceptional rate capabilities when used as electrodes in Li-ion batteries [94]. The Mn based spinels are well suited as cathodes due to their high voltage [95, 96, 97, 98] while the Ti derived spinels, with their substantially lower voltages, are more suited as anode materials [99, 100, 101, 102]. The spinel crystal structure is also a promising intercalation host for Na and Mg-ion batteries. Recent experimental studies by Sun *et. al.* demonstrated that a sulfide spinel can intercalate Mg reversibly in a Mg-ion battery [103]. Manganese based spinel compounds have also shown promise as positive electrodes for Na-ion batteries [104, 105, 106].

[1] This chapter is largely reproduced from previously published work [93].

Spinel has a general chemical formula of AB_2X_4 and belongs to the $Fd\bar{3}m$ space group. The anions, X (i.e. oxygen or sulfur), of the spinel crystal structure occupy the 32e Wyckoff positions and form a face-centered cubic (FCC) lattice. The A cations occupy the 8a sites and are tetrahedrally coordinated by X, while the B cations occupy the octahedrally coordinated 16d sites. For instance, in spinels such as $LiMn_2O_4$, Li occupies the tetrahedral 8a sites and Mn occupies octahedral 16d sites [95]. The spinel crystal structure can also accommodate guest cations in the octahedrally coordinated 16c sites, which together with the tetrahedral 8a sites form a three-dimensional interconnected network that facilitates the rapid insertion and removal of guest cations [95] (see Fig. 5.1).

While a variation in the transition metal chemistry tends to affect the average voltage of the spinel compound [107, 108], much less is known about how anion chemistry (oxygen versus sulfur) and guest cation chemistry (Li versus Na versus Mg) affects the electrochemical properties of spinels. In transition metal oxide spinels, for example, Li prefers the tetrahedral sites, and only displaces to octahedral sites once the number of Li exceeds the number of available tetrahedral sites [95, 109, 110]. In a sulfide spinel such as TiS_2, in contrast, Li prefers the octahedral sites [111] at all compositions. Mg, which has the same ionic radius as Li but a higher valence, occupies tetrahedral sites in oxides such as $MgCr_2O_4$ [112], but prefers a mix of tetrahedral and octahedral sites in sulfide spinels such as TiS_2 [113, 103]. In spite of the increased interest in Na-ion batteries, very little is known about the behavior of Na in spinel compounds. The larger ionic radius of Na compared to those of Li and Mg suggests that different electrochemical properties should emerge upon insertion of Na into a spinel host.

Here we perform a first-principles statistical mechanics study of the electrochemical properties of spinel as a function of intercalating guest species and anion chemistry by focusing on six systems. We consider an oxide and a sulfide spinel, using spinel CoO_2 and

TiS_2 as model host compounds. For each we determine the electrochemical properties, site preferences, and volume expansion upon insertion of Li, Na, and Mg. Li and Mg have the same ionic radius but a different valence, while Na has the same valence as Li but a larger ionic radius than both Li and Mg. This makes it possible to separate the role of ionic radius from guest cation oxidation state. The role of electrostatic interactions can be assessed by comparisons between the more ionic CoO_2 and the more covalent TiS_2 spinel hosts.

The results of this study reveal general principles with which to rationalize the electrochemical properties of spinels, which are to a large extent determined by guest cation site preferences. Guest cation radius plays an important role in determining site preference, with larger cations favoring octahedral sites. Electrostatic interactions, which become more important in oxide hosts, work in the opposite direction and favor tetrahedral occupancy. A higher guest cation oxidation state leads to an increased stability of cation-vacancy ordered phases and can lead to mixed occupancy over tetrahedral and octahedral sites. These principles can be combined to tailor the electrochemical properties of spinel intercalation compounds and suggest that Na insertion into oxide spinel hosts should enable high rate capable electrodes.

5.2 Methods

Density Functional Theory (DFT) as parametrized by Perdew Burke and Ernzerhof (PBE) [15] was used to calculate formation energies of Li/Na/Mg-vacancy orderings over the interstitial sites of spinel CoO_2 and TiS_2 (roughly 1100 calculations in total). Projector augmented wave (PAW) [16, 92] theory was used to approximate the core electrons. DFT calculations were performed using the Vienna ab-initio software package (VASP) [14, 13]. Plane-wave cutoff energies of 450, 530, and 600 eV were used for calculations

containing Mg, Na, and Li respectively. A Monkhorst-Pack k-point grid of 7x7x7 was used for the primitive cell; calculations with larger supercells had a scaled grid to maintain or exceed the k-point density of the primitive cell. Formation energies of A-vacancy (A=Li,Na,Mg) configurations over the tetrahedral and octahedral sites of spinel CoO_2 and TiS_2 were used to train cluster expansion Hamiltonians [17, 114] to predict the energy of arbitrary configurations within each spinel host. The cluster expansion Hamiltonians were used in grand canonical Monte Carlo simulations to calculate room temperature electrochemical properties, including open circuit voltage profiles and equilibrium site occupancies. The Clusters Approach to Statistical Mechanics (CASM) software package was used to construct and parametrize the cluster expansions and to perform the grand canonical Monte Carlo simulations [36, 35, 39, 69].

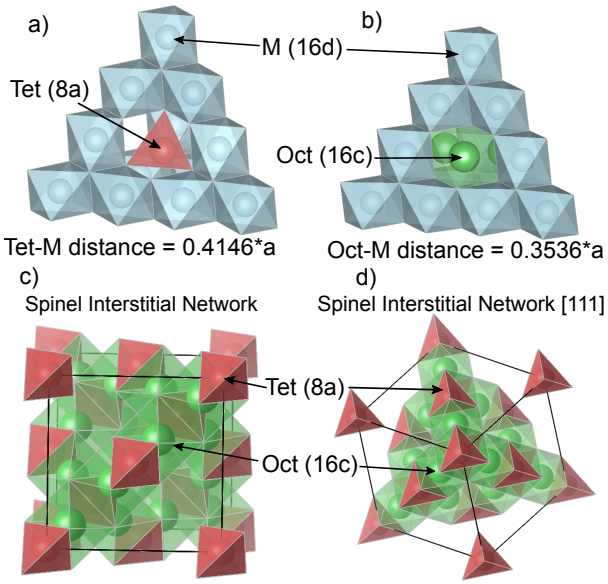

Figure 5.1: (a) The connectivity between a tetrahedral interstitial and the MX_2 framework of the spinel crystal structure. (b) The connectivity between octahedral interstitials and the MX_2 framework of the spinel crystal structure. (c) & (d) Intercalating species can fill a network of interconnected tetrahedral and octahedral sites within the spinel host. The tetrahedral (8a) sites form a diamond network with octahedral (16c) sites located between neighboring tetrahedral sites. The tetrahedral and octahedral sites share faces.

5.3 Results

Spinel intercalation compounds have cubic symmetry, with transition metal cations ordered over half the octahedral interstitial sites of a close-packed FCC anion sublattice. Li, Na, or Mg guest cations can occupy one of two distinct sets of interstitial sites that do not share faces with the transition metal containing octahedra. The tetrahedral (8a) sites form a diamond network, with each tetrahedral site surrounded by four octahedral (16c) sites. There are twice as many octahedral sites as tetrahedral sites, with each octahedral site sharing a face with two tetrahedral sites. Fig. 5.1 shows the connectivity of the MX_2 spinel framework and its interstitial sites. The simultaneous occupation of adjacent octahedral and tetrahedral sites is energetically unfavorable due to large electrostatic repulsions. Guest cation (i.e. Li, Na, or Mg) migration through the interstitial network of a spinel host requires elementary hops between adjacent octahedral and tetrahedral sites. A large difference in energy between the tetrahedral and octahedral sites will, therefore, result in high migration barriers for cation diffusion [109, 111, 115, 116] and any strategy that equalizes the tetrahedral and octahedral site energies should lead to an enhancement of guest cation mobility within the spinel host.

To identify the factors that determine site preference within spinel, we first calculated the relative stability between octahedral 16c and tetrahedral 8a site occupancy in the dilute limit as a function of volume for Li, Na, and Mg in the TiS_2 and CoO_2 spinel hosts. Fig 5.2 shows the variation of the energy of an octahedral and a tetrahedral A-cation in a 2×2×2 super cell of the primitive spinel unit cell (i.e. $A_{1/32}MX_2$) as a function of the conventional cubic cell lattice parameter for the six systems. A comparison of Figs. 5.2 (a) and (e) and of Figs. 5.2 (b) and (f) shows that Li and Mg have very similar site preferences in both spinel TiS_2 and CoO_2 respectively. This is likely due to their similar ionic radii (0.68 Å vs. 0.66 Å) [117]. In the sulfide spinel, both Li and Mg prefer the

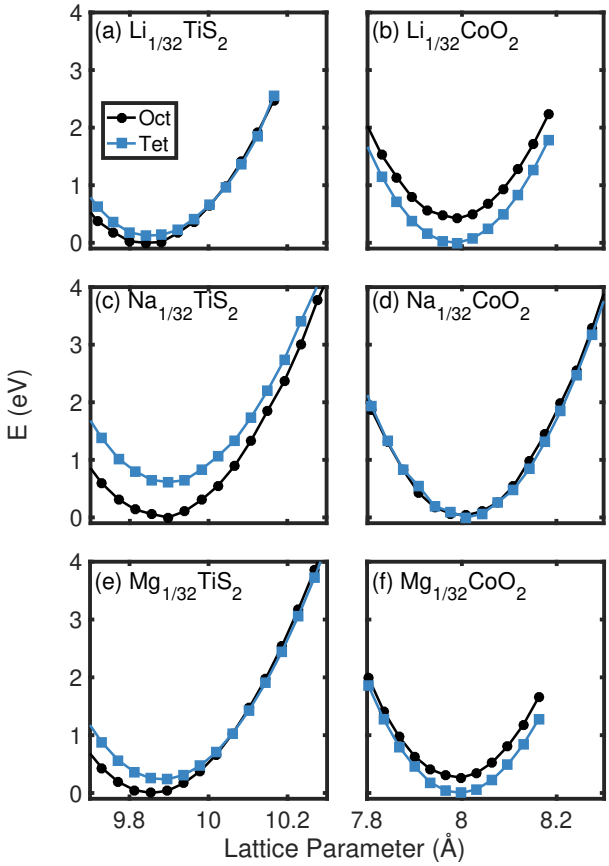

Figure 5.2: Total energies of octahedrally coordinated A-ions (black circle) and tetrahedrally coordinated A-ions (blue square) as a function of the conventional cubic cell lattice parameter of for the systems (a) Li_xTiS_2, (b) Li_xCoO_2, (c) Na_xTiS_2, (d) Na_xCoO_2, (e) Mg_xTiS_2, and (f) Mg_xCoO_2. Calculations were performed in the dilute limit in a cell that corresponds to a 2x2x2 supercell of the spinel primitive cell and a composition of $A_{1/32}MX_2$. The energy scale is relative to the lowest energy structure.

octahedral site at dilute concentrations, only marginally favoring the tetrahedral site at volumes that are substantially larger than the equilibrium volume of spinel TiS_2. In the oxide, the Li and Mg site preference is reversed, with both cations favoring the tetrahedral site over the octahedral site. This reversal can be attributed to the more ionic nature of the CoO_2 host compared to the more covalent TiS_2 host. The distance between the A-cation and its neighboring transition metal cations M in the 16d sites is larger for the tetrahedral 8a site than for the octahedral 16c site (0.4146a vs. 0.3536a, where a is

the conventional cubic lattice parameter). The enhanced electrostatic interactions in the oxide, therefore, lead to a preference for tetrahedral 8a site occupancy as it enables an increased separation between positively charged cations.

A comparison between Li and Na intercalation in the CoO_2 and TiS_2 spinel hosts shows the importance of the cation radius in determining site preference. Fig.5.2 (c) shows that Na, with its larger ionic radius (0.97 Å) [117], prefers the larger octahedral site (2.345 x 10^{-2} a^3 $Å^3$ where a is the conventional cubic lattice parameter) substantially more (by 0.3 eV to 1 eV) than the smaller tetrahedral site (6.634 x 10^{-3} a^3 where a is the conventional cubic lattice parameter) in TiS_2. In the more ionic $Na_{1/32}CoO_2$ oxide (Fig.5.2 (d)) the energies of the tetrahedral and octahedral sites are almost equal to each other. The enhanced electrostatic interactions that generally favor tetrahedral occupancy in the oxide is not sufficient to overcome the cost in energy of squeezing the larger Na cation into the smaller tetrahedral site, thereby making the tetrahedral and octahedral sites in CoO_2 essentially degenerate in energy at dilute Na concentrations.

Site preferences in spinel at higher guest cation concentrations can be revealed by considering formation energies of a large number of A-vacancy configurations within spinel TiS_2 and CoO_2 as a function of concentration. These are shown in Fig. 5.3. Configurations having only octahedrally (tetrahedrally) coordinated guest cations are shown in blue (red), while those having a mix of octahedral and tetrahedral occupancy are shown in purple. The majority of the ground state configurations (the lowest energy configurations that reside on the convex hull) in TiS_2 contain octahedrally coordinated guest ions. Only in Mg_xTiS_2 are there ground state configurations at intermediate to high x that consist of a mix of octahedrally and tetrahedrally coordinated Mg ions. A comparison between the formation energies of Li_xTiS_2 and Na_xTiS_2 configurations shows that increasing the ionic radius of the guest cation while keeping its oxidation state fixed, penalizes tetrahedral site occupancy in the spinel host. Fig. 5.3 (c) shows a

very strong preference for octahedral occupancy at all concentrations in Na_xTiS_2, with configurations having any tetrahedral occupancy being substantially higher in energy compared to configurations having only octahedral occupancy.

Figs. 5.3 (b), (d), and (f) show a stronger preference for tetrahedral sites in the more ionic A_xCoO_2 spinel compounds. All Li_xCoO_2 ground states below $x = 1/2$ contain only tetrahedrally coordinated Li. Mg_xCoO_2 exhibits a similar trend, with the exception of the ground state at $x = 5/12$, which consists of a mix of tetrahedral and octahedral occupancy. While most Mg reside in tetrahedral sites in this ground state, some occupy octahedral sites, thereby allowing an increase of some Mg-Mg pair distances. Both Li_xCoO_2 and Mg_xCoO_2 also exhibit a large two-phase region between $x = 1/2$ and $x = 1$ in which the guest cations transition from tetrahedral occupancy at $x = 1/2$ to octahedral occupancy at $x = 1$. The majority of ground state configurations in Na_xCoO_2, in contrast, have mixed tetrahedral and octahedral occupancy. Only at $x = 1/2$ do the Na cations exclusively occupy tetrahedral sites.

Intercalation of guest cations into a host compound is usually accompanied by a volume increase. Fig. 5.4 shows the cube root of the cell volume for A-vacancy configurations within spinel TiS_2 and CoO_2 that have energies within 10 meV/atom of the convex hull. The cube root of the volume can be used as a proxy for an averaged conventional cubic cell lattice parameter for each cation-vacancy configuration in spinel, even if the particular configuration does not strictly preserve cubic symmetry. While Fig. 5.4 shows that all compounds undergo a volume expansion with concentration, x, the Na_xCoO_2, Na_xTiS_2, Li_xCoO_2, and Mg_xCoO_2 systems exhibit very little variation in cell volume between configurations at each concentration. This is not true in Li_xTiS_2 and Mg_xTiS_2 which exhibit significant variations in cell volume at each concentration. Figures 5.4 (c) and (d) show that Na insertion into spinel induces larger volume changes of the host than that accompanying Li or Mg insertion.

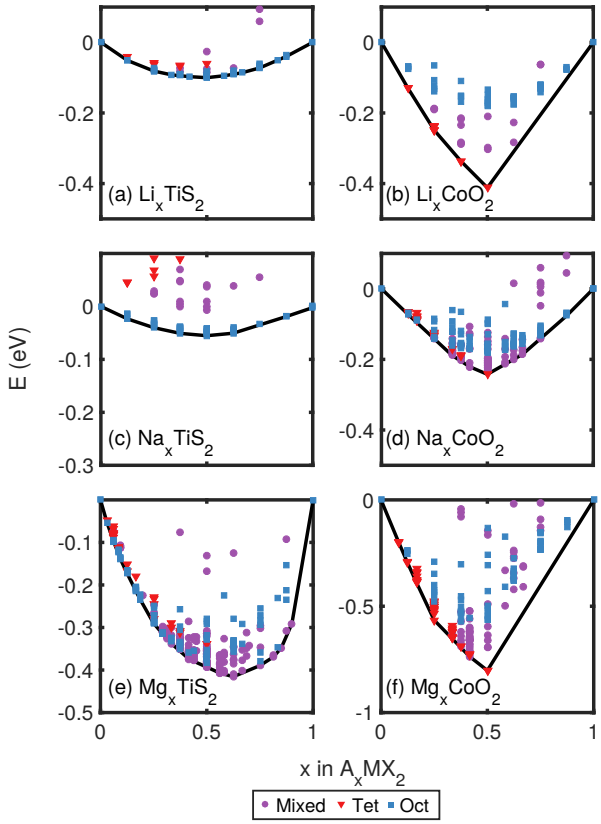

Figure 5.3: The formation energies (eV/formula unit) of A-vacancy configurations within spinel MX_2 as a function of A composition for the systems (a) Li_xTiS_2, (b) Li_xCoO_2, (c) Na_xTiS_2, (d) Na_xCoO_2, (e) Mg_xTiS_2, and (f) Mg_xCoO_2. Configurations that contain all octahedrally coordinated magnesium, all tetrahedrally coordinated magnesium, and mixed coordination correspond to blue squares, red triangles, and purple circles respectively. The convex hull (black line) connects the ground state configurations. Note that the scale on subfigure (c) and subfigure (f) are different due to a shallow and deep convex hull respectively.

The voltage of an electrode material is related to the chemical potential of the shuttled cation according to the Nernst equation

$$V(x) = -[\mu_{\mathrm{A}}(x) - \mu^{\circ}_{\mathrm{A}}]/ze \tag{5.1}$$

where z = 1 for Li and Na and z=2 for Mg. μ°_{A} is the chemical potential of the respective

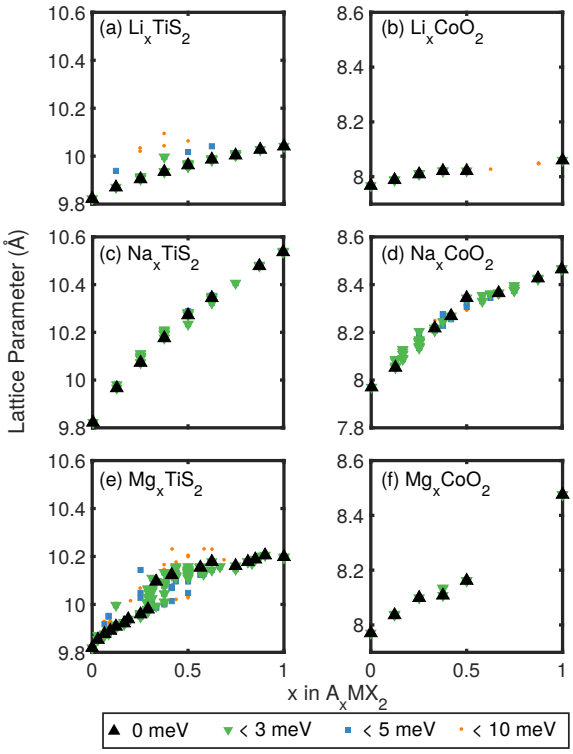

Figure 5.4: Cubic cell lattice parameter (calculated as the cube root of the cell volume) for spinel A_xMX_2 as a function of A composition at 0 K according to DFT for configurations with formation energies within 10 meV/atom from the convex hull for the systems (a) Li_xTiS_2, (b) Li_xCoO_2, (c) Na_xTiS_2, (d) Na_xCoO_2, (e) Mg_xTiS_2, and (f) Mg_xCoO_2. The black triangles, green triangles, blue squares, and orange circles represent the ground states, configurations with energies within 3 meV/atom, 5 mev/atom, and 10 meV/atom from the convex hull respectively.

A metal reference electrode. We calculated the chemical potentials of Li, Na, and Mg in spinel CoO_2 and TiS_2 at room temperature with grand canonical Monte Carlo simulations applied to cluster expansions of the configurational energy of cation-vacancy disorder. A separate cluster expansion was parameterized for each of the six spinel compounds using the DFT-PBE formation energies of Fig. 5.3 as training data.

Fig. 5.5 shows the calculated voltage profiles of all six compounds at room temperature (300 K) relative to their respective metallic electrodes. The sloping voltage profiles of the three sulfides indicate solid solution behavior. Fig. 5.5 e. shows that, at 300K, it is

not thermodynamically favorable to intercalate more than $x = 0.9$ Mg into TiS_2 because the voltage reaches 0 at this point. The voltage profiles of the oxide exhibit more pronounced features indicative of ordering reactions and phase transformations. The steps in the voltage profile indicate the occurrence of stable ordered phases at stoichiometric compositions while plateaus correspond to two-phase reactions. Both Li_xCoO_2 and Mg_xCoO_2 have voltage profiles that are qualitatively very similar. A large step at $x = 0.5$ separates a high voltage region between $x = 0$ and 0.5 from a plateau extending from $x = 0.5$ to 1 at lower voltages. While Na_xCoO_2 also exhibits a step at $x = 0.5$ it is not as large as in the Li and Mg containing oxide spinels. Na_xCoO_2 also does not exhibit a large plateau between 0.5 and 1, but rather a smoother sloping profile signifying solid solution behavior toward the end of discharge.

More insight about the evolution of the voltage profiles can be gained by inspection of the site occupancy as a function of cation content. Fig. 5.6 shows the distribution of A cations on tetrahedral and octahedral interstitial sites as a function of composition. In Li_xTiS_2 and Na_xTiS_2, the cations exclusively occupy the octahedral sites. The Mg cations of Mg_xTiS_2 initially only fill octahedral sites but start to occupy a small fraction of tetrahedral sites as well beyond $x = 0.375$. All three sulfide spinels exhibit a solid solution at room temperature. The preference for octahedral sites in these compounds results in a sloping voltage profile.

Site occupancy in the oxides is more complex than in the sulfides. Li and Mg both prefer the tetrahedral sites over the octahedral sites in spinel CoO_2 below $x = 1/2$, although there is some mixed occupancy in Mg_xCoO_2 around $x = 5/12$ to maximize Mg-Mg pair distances. At $x = 0.5$ all tetrahedral sites are filled in Li_xCoO_2 and Mg_xCoO_2 and further increases in cation concentration must be accommodated by the less favorable octahedral sites. The filling of all tetrahedral sites results in a large step in the voltage profile at $x = 0.5$. Since the tetrahedral and octahedral sites share faces, the filling of oc-

tahedral sites requires a simultaneous displacement of tetrahedrally coordinated cations, which occurs through a two-phase reaction. This two-phase reaction manifests itself as a plateau between $x = 0.5$ and $x = 1$ in the voltage profile. Both Li_xCoO_2 and Mg_xCoO_2 also show smaller voltage steps below $x = 0.5$ due to cation ordering over the tetrahedral sites. In Na_xCoO_2, the tetrahedral and octahedral sites are essentially degenerate in energy. Hence Na insertion into spinel CoO_2 occurs on both tetrahedral and octahedral sites. At $x = 0.5$, the Na fill all tetrahedral sites as this configuration maximizes the distance between nearest neighbor Na cations (3.62 Å)at the 0.5 composition. Na_xCoO_2 also exhibits an extended solid solution beyond $x = 0.65$ consisting of mixed octahedral/tetrahedral occupancy. The voltage profile of Na_xCoO_2 is therefore, similar to those of the sulfides at low and high concentrations due to high octahedral site occupancy at those concentrations, but it also exhibits the large step that characterizes the voltage profiles of the other oxide spinels due to tetrahedral filling at $x = 0.5$.

5.4 Discussion

Our first-principles statistical mechanics study of spinel A_xCoO_2 and A_xTiS_2 with A being either Li, Na or Mg has enabled a systematic determination of the effect of (i) host ionicity (i.e. oxide versus sulfide), (ii) the A cation radius and (iii) the A cation oxidation state on the electrochemical properties of spinel intercalation compounds. Oxides are generally more ionic than sulfides. A clear manifestation of this emerges when comparing the A cation site preferences in spinel CoO_2 to those of TiS_2. Tetrahedral sites are preferred in more ionic spinel hosts, as it allows an increased separation between the postively charged guest cations and the transition metal cations. Furthermore, the tetrahedral 8a sites of spinel share corners with transition metal containing 16d octahedra, while the octahedral 16c sites share edges with the 16d sites (see Fig. 5.1). TiS_2 is

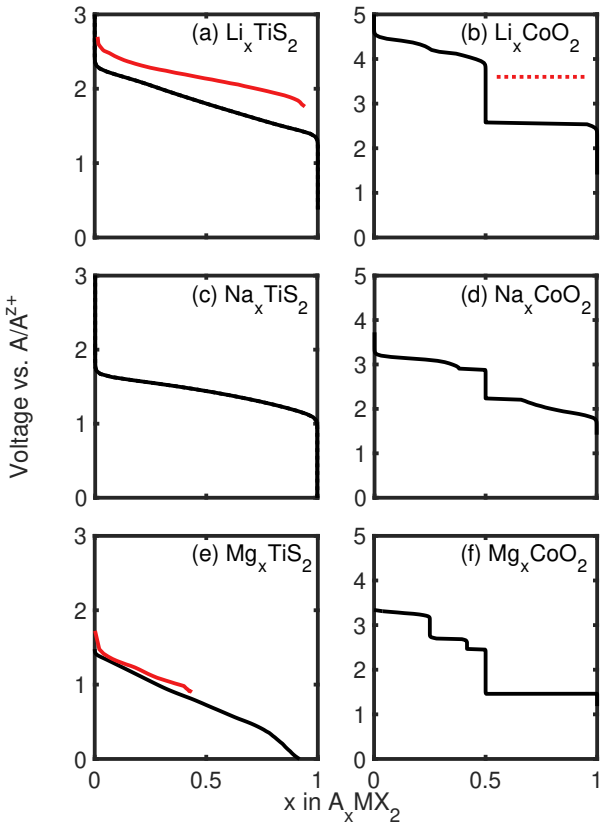

Figure 5.5: The calculated voltage of A_xMX_2 relative to A metal from a Monte Carlo simulation for the systems (a) Li_xTiS_2, (b) Li_xCoO_2, (c) Na_xTiS_2, (d) Na_xCoO_2, (e) Mg_xTiS_2, and (f) Mg_xCoO_2. An experimental voltage curve of Li_xTiS_2 / Li coin cell measured by Bonnick *et. al.* is shown on (a) [118]. The value of the voltage plateau representing the $x > 0.5$ region of an experimental voltage curve of Li_xCoO_2 / Li coin cell measured by Kim *et. al.* is shown on (b) [119]. An experimental voltage curve of Mg_xTiS_2 / Mg coin cell measured by Sun *et. al.* [103] is shown on (e).

a more covalent and compliant crystal than CoO_2, with the larger sulfur anion able to more effectively screen transition metal-intercalant electrostatic interactions. Octahedral sites are therefore preferred in TiS_2 as steric factors play a more important role.

The effect of guest cation radius on site preference in spinel is clearly revealed by the differences between the Li and Na containing spinels. The difference in energy between the smaller tetrahedral and the larger octahedral sites in spinel Na_xTiS_2 (between 0.3 eV and 1 eV) is significantly larger than in Li_xTiS_2 (between 0.1 eV and 0.5 eV), which can be attributed to the larger ionic radius of Na (0.97 Å) compared to that of Li (0.68 Å). In

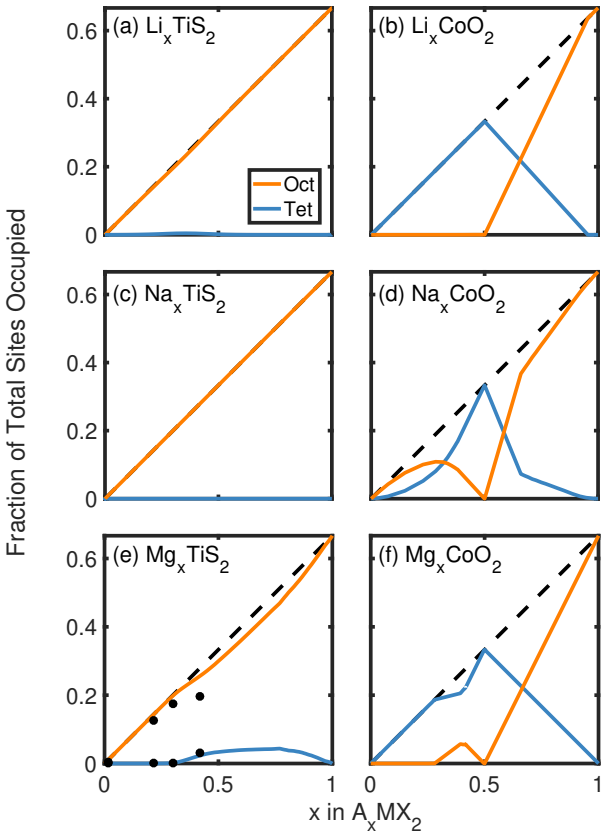

Figure 5.6: A concentration in the octahedral (orange line) and tetrahedral sites (blue line) of spinel at 333 K as calculated with Monte Carlo simulations for the systems (a) Li_xTiS_2, (b) Li_xCoO_2, (c) Na_xTiS_2, (d) Na_xCoO_2, (e) Mg_xTiS_2, and (f) Mg_xCoO_2. The black points in (e) are experimentally measured concentrations from Sun *et. al.* [103]

the oxide spinel, where Li very much favors the tetrahedral sites, Na is more ambivalent, with tetrahedral and octahedral site energies being essentially degenerate.

The guest cation's formal oxidation state also plays a role in affecting electrochemical properties. While Li and Mg insertion into the same spinel host generates voltage profiles that are qualitatively similar to each other, there are differences. These can be attributed to a difference in the Li and Mg oxidation state since Li^+ and Mg^{2+} have very similar ionic radii (0.68 Å vs. 0.66 Å) [117]. The voltage profile of Mg_xCoO_2 has larger steps than that of Li_xCoO_2 (especially at $x = 0.25$), signifying an increased stability of cation-vacancy orderings that is likely driven by stronger electrostatic interactions in the former. The Mg

containing spinels also exhibit mixed tetrahedral/octahedral occupancy that is likely also driven by electrostatic interactions, as mixed occupancy at intermediate concentrations enables an increased separation between Mg pairs.

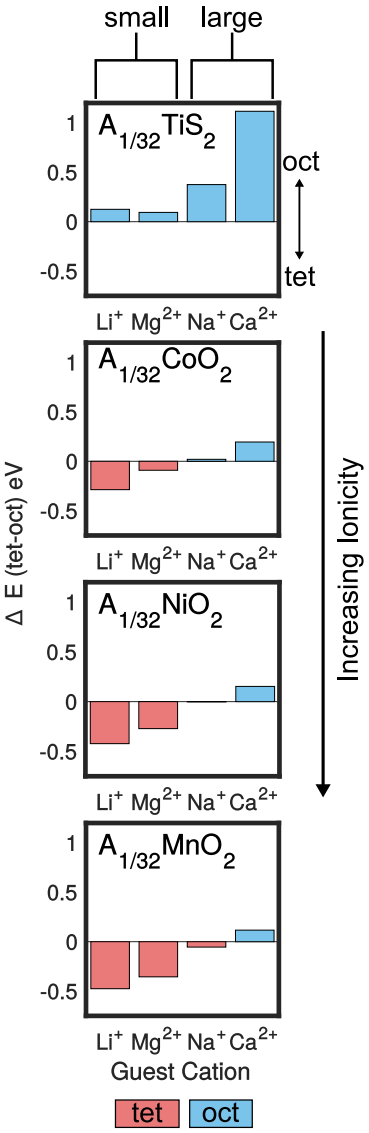

Figure 5.7: Total energy differences between tetrahedrally coordinated A-ions and octahedrally coordinated A-ions as a function of guest cation for TiS_2, CoO_2, NiO_2, and MnO_2 spinels. Calculations were performed in the dilute limit in a cell that corresponds to a 2x2x2 supercell of the spinel primitive cell and a composition of $A_{1/32}MX_2$. The color coded bars summarize the preference for octahedral (blue) or tetrahedral (red) coordination of the guest cation for each system.

The general trends identified in this study have been distilled from two model spinel host chemistries. The TiS_2 and CoO_2 spinel hosts investigated here have relatively simple electronic structures characterized by itinerant valence electrons. Many oxide spinel compounds contain Mn and/or Ni and further studies on these compounds are necessary to generalize or nuance the trends identified here. Additional complexities are expected in Mn and Ni containing spinel compounds, however, as electrons in these compounds tend to localize more. Contributions from additional electronic degrees of freedom that can give rise to Jahn-Teller distortions, charge ordering, orbital ordering and magnetic ordering must therefore be explicitly taken into account [120].

Simple calculations of site energy differences, however, indicate that the trends established here persist in the more complex and ionic NiO_2 and MnO_2 spinel hosts at dilute guest cation concentrations. This is revealed in Fig. 5.7, which compares the difference in energy between tetrahedral and octahedral site occupancy at dilute Li, Mg, Na and Ca concentrations in the spinel forms of TiS_2, CoO_2, NiO_2 and MnO_2. (Fully relaxed DFT calculations were performed in 2×2×2 supercells of the spinel primitive cell holding the lattice parameters fixed at the equilibrium lattice parameters of the host in the absence of a guest cation). Both the NiO_2 and MnO_2 compounds tend to be more ionic than CoO_2 since the occupied transition metal d-orbitals of Ni and Mn in the spinels hybridize less with the surrounding oxygen p-orbitals than those of Co [6]. Ca is also included because its ionic radius is very similar to that of Na (Na 0.97 Å and Ca 0.99 Å [117]) but its formal oxidation state is +2 as opposed to +1. Fig. 5.7 clearly shows an increased preference for tetrahedral occupancy over octahedral occupancy as the ionicity of the host increases. For Na, the difference in energy between tetrahedral and octahedral occupancy is very small in all three oxides, however, there is a general trend towards tetrahedral occupancy when going from CoO_2 to NiO_2 to MnO_2. The Na preference for tetrahedral 8a sites in MnO_2 is consistent with experimental observations for spinel MnO_2 (i.e. λ-MnO_2) [104]

and $Ni_{0.25}Mn_{0.75}O_2$ [105]. The role of guest cation radius is also clearly apparent in Fig. 5.7, with an increase in cation radius favoring octahedral sites over tetrahedral sites. A more subtle trend is revealed with respect to the guest cation oxidation state. Figure 5.7 suggests that the tetrahedral sites become slightly less stable when going from a guest cation oxidation state of +1 to +2 while holding the ionic radius fixed. It should be noted though that for the same guest cation concentration, the guests with formal oxidation state +2 donate twice as many electrons than the guests with oxidation state +1 and thereby reduce the host at twice the rate. Each +2 guest cation is therefore surrounded by twice as many reduced transition metal cations (i.e. M^{+3}) and we suspect that this leads to a slight reduction in electrostatic repulsion between the guest cation and the surrounding transition metals.

Guest cation mobility ranks among the most important properties that require optimization for battery applications. Cation transport within the spinel host arises from successive hops between nearest neighbor tetrahedral and octahedral sites [109, 111, 115]. Any reduction in the energy difference between the tetrahedral and octahedral sites of spinel will, therefore, lead to an increase in cation mobility [116]. The general principles revealed by this study show that the energy difference between tetrahedral and octahedral site occupancy in spinel can be controlled by tuning guest cation radius and host bonding character. The combination that appears to equalize the tetrahedral and octahedral site energies most is Na insertion into an oxide spinel. Indeed, the calculations of this study predict that the tetrahedral and octahedral sites are nearly degenerate in spinel CoO_2 upon insertion of Na. The flattening of the energy landscape in Na_xCoO_2 arises from a competition between electrostatic interactions, which favor tetrahedral sites, and steric factors, which favor the larger octahedral sites. Fig. 5.7 suggests that the same is true in the dilute limit in NiO_2 and MnO_2 spinels. The larger ionic radius of Na compared to that of Li, should result in lower migration barriers for Na diffusion compared to those

for Li diffusion in the same spinel host. We expect that alloying strategies exist with which the degree of ionic bonding of the spinel host can be fine-tuned to maximize Na ion mobility within spinel. Other factors must, of course, also be taken into consideration when searching for optimal transition metal chemistries, including a determination of whether the chemistry favors the spinel crystal structure and whether it is resistant to common electrochemical or mechanical degradation mechanisms [6].

5.5 Conclusion

We investigated the effects of anion chemistry (oxide/sulfide) and guest cation chemistry (Li/Na/Mg) on the electrochemical properties of spinel intercalation compounds. The electrochemical properties of spinel compounds are highly sensitive to guest cation site preferences. Two factors play a dominant role in determining guest cation site preference within spinel: (i) the guest cation radius, with larger cations favoring octahedral sites and (ii) the bonding character of the host, with the more ionic oxides favoring tetrahedral site occupancy. Our study has revealed simple design principles with which new spinel compounds can be developed and has indicated that Na insertion into oxide spinel compounds shows promise for high rate capable batteries. The large ionic radius of Na favors octahedral coordination while the ionic host of an oxide favors tetrahedral coordination, resulting in a unique equalization of the tetrahedral and octahedral site energies in spinel Na_xCoO_2. The energy difference between tetrahedral and octahedral sites in spinel is directly correlated with cation mobility and any flattening of the energy landscape will result in enhanced cation mobilities. We expect that these insights will lead to the discovery of transition metal oxide chemistries that will form spinel hosts that can be synthesized and that simultaneously enable high Na-ion mobilities.

5.6 Acknowledgement

S. K. Kolli is grateful for helpful discussions with Dr. Maxwell D. Radin, Julija Vinckeviciute, and John G. Goiri. This material is based upon work supported by the National Science Foundation, Grant DMR- 1410242. We acknowledge support from the Center for Scientific Computing from the CNSI, MRL: an NSF MRSEC (DMR-1121053). This research used resources of the National Energy Research Scientific Computing Center, a DOE Office of Science User Facility supported by the Office of Science of the U.S. Department of Energy under Contract No. DE-AC02-05CH11231.

Chapter 6

Elucidating cation mobility shutdown in spinel and rocksalt intercalation compounds

6.1 Introduction

The rich variety of intercalation compounds that can host Li^+, Na^+, K^+ and Mg^{2+} ions has led to the development of a multitude of promising rechargeable battery types that rely on the shuttling of mobile cations between an anode and a cathode [121, 122, 123, 124, 125, 126, 127, 128, 4, 129, 130, 131, 132, 133, 134, 135]. The rate with which such a rechargeable battery can be cycled is in large part determined by the diffusion coefficient of the shuttled cation within the electrodes [136]. Several factors affect cation diffusion coefficients, including the chemistry, crystal structure and cation concentration of the host material [137].

The majority of today's commercial Li-ion batteries utilize a dense transition metal oxide as the electroactive material in their cathodes. Important examples include the

family of layered transition metal oxides such as $LiCoO_2$, $LiNi_{(1-y-z)}Mn_yCo_zO_2$ (NMC) and $LiNi_{(1-y-z)}Co_yAl_zO_2$ (NCA) [138] as well as the high voltage $LiMn_{2-y}Ni_yO_4$ [139] spinels. The $Li_xM_{1-x}O$ disordered rocksalts [8], where M refers to a mixture of transition metals, are also receiving much attention as high capacity alternatives to current cathode materials [12, 140, 141, 7, 9].

The oxygen ions of most transition metal oxide electrode materials adopt a close-packed face-centered cubic (fcc) lattice, with transition metals filling a subset of the octahedral interstitial sites of the oxygen sublattice [138]. In the layered materials, the transition metals fill alternating (111) planes of octahedral interstitial sites, while in the spinel crystal structure, they adopt a three dimensional ordering. In the disordered rocksalts [8], the transition metals are more randomly distributed, although they often exhibit some degree of short-range order [142, 9]. In all three materials classes, the remaining octahedral interstitial sites are available for occupancy by guest ions such as Li.

The topology of an fcc oxygen sublattice has important consequences for cation transport. If the mobile cation prefers octahedral sites, it must migrate through a tetrahedral site, where it will usually thermalize, before continuing on to an adjacent octahedral site [143, 144, 111, 137]. Since the intermediate tetrahedral site is coordinated by four octahedral sites, the barriers of cation hops will be very sensitive to the number of other cations in the surrounding octahedral sites [111]. Electrostatic and steric interactions generally lead to an increase of the migration barrier with the number of cations in surrounding octahedral sites as schematically illustrated in Figure 6.1. Our findings show that the diffusion in intercalation compounds is dominated by the lowest barrier vacancy cluster. This leads to highly correlated diffusion mechanisms that are mediated by vacancy clusters, such as double vacancies in layered materials and triple vacancies in spinels [111, 137].

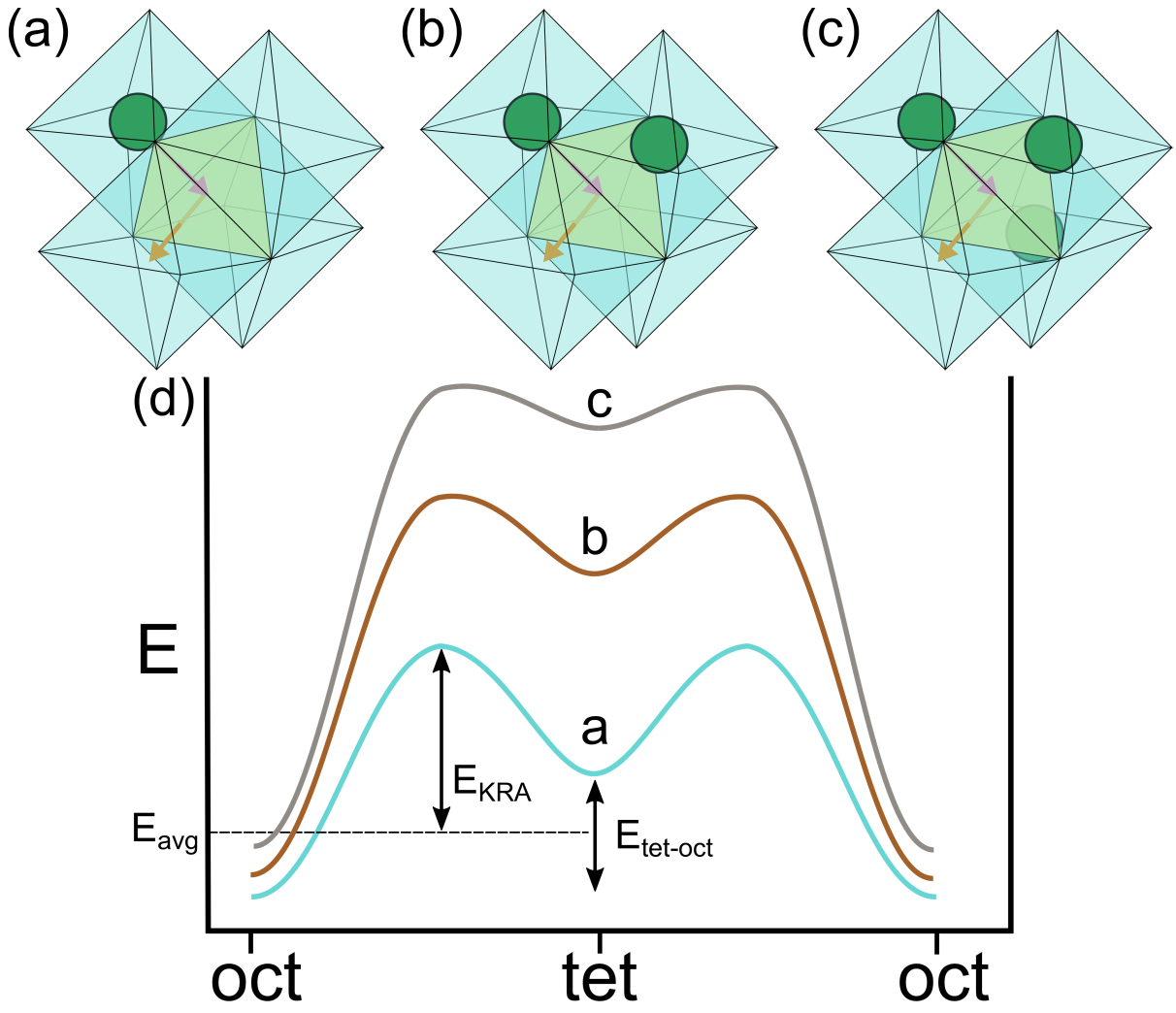

Figure 6.1: The diffusion path for a cation on an octahedral site via a (a) triple vacancy, (b) divacancy, and (c) single vacancy mechanism. (d) Hypothetical energy landscapes for these diffusion mechanisms. The ion first moves to the tetrahedral site via the magenta arrow. For productive diffusion, the ion must move forward via the orange arrow (or one of its equivalents) instead of hopping back to its original spot.

While the transition metal (TM) cations of layered and spinel hosts are well ordered over the octahedral sites of an fcc anion sublattice, they are more randomly distributed in disordered rocksalts (DRX) [8, 12]. In contrast to layered compounds where each intermediate tetrahedral site of a hop is coordinated by one TM [144] or to spinel compounds where those sites are coordinated by zero TM [111], the tetrahedral sites of DRX may be coordinated by 0, 1 or 2 transition metal cations (labeled 0-TM, 1-TM and 2-TM sites) [12, 145]. The most facile hops are those that pass through the 0-TM tetrahedral sites. The tetrahedral sites coordinated by 1 or 2 transition metals have significantly higher barriers due to electrostatic interactions arising from the high oxidation state of the transition metals [12]. Optimal Li transport occurs in disordered rocksalts with transition metal compositions that ensure percolating networks of 0-TM, which requires a Li:TM ratio greater than 1:1 [12].

Here we show that vacancy cluster diffusion mechanisms in intercalation compounds with an fcc anion sublattice result in diffusion coefficients that have a strong concentration dependence. We use kinetic Monte Carlo simulations to calculate cation diffusion coefficients and show that the diffusion coefficient drops significantly once the concentration of the diffusion-mediating vacancy clusters fall below a percolation threshold. We focus on the spinel compound as a model system since its TM ordering over the octahedral sites of an fcc anion sublattice ensures fully percolating networks of 0-TM tetrahedral sites. The spinel crystal can, therefore, be viewed as the idealized limit of DRX compounds with fully percolating 0-TM channels, without requiring a deficiency of TM below x=1/2. We find that even with fully percolating 0-TM networks, the cation diffusion coefficient can drop by several orders of magnitude over a small concentration interval due to the onset of highly correlated motion that arises once interconnected networks of diffusion mediating vacancy clusters become cut-off from each other. The results of this study provide fundamental insights about diffusion processes with which electrode materials

having superior transport properties can be designed.

6.2 A concrete example: Mg diffusion in spinel TiS_2

To illustrate the key characteristics of cation diffusion in an fcc anion sublattice, we first consider Mg diffusion in spinel TiS_2. The promise that Mg-ion batteries can offer high energy densities and capacities due to the 2^+ oxidation state of the shuttled Mg-ions [134, 146, 135] has led to both theoretical and experimental interest in spinel TiS_2 as a candidate electrode material [147, 148, 149]. Figure 6.2 shows the experimentally measured voltage curve of spinel Mg_yTiS_2 [118] and compares it to a voltage curve that was calculated with Monte Carlo simulations applied to a first-principles cluster expansion of the Mg_yTiS_2 system at 333 K [149]. The agreement is very good. Mg predominantly occupies the octahedral sites, but exhibits some tetrahedral site occupancy at intermediate concentrations [147, 149]. The smooth voltage curve indicates a solid solution without any strong ordering tendencies [136].

The experimental voltage curve only extends to $y \approx 0.5$. The calculated voltage curve, in contrast, suggests that the Mg concentration can reach a value of $y \approx 0.8$ before the voltage equals zero. The limited experimental capacity has been attributed to a decrease in the Mg diffusion coefficient at higher Mg concentrations. Figure 6.3a shows the self-diffusion coefficient (also referred to as the jump diffusion coefficient [19, 136]) of Mg in TiS_2 as calculated with kinetic Monte Carlo simulations at 333 K applied to the same cluster expansion Hamiltonian used to calculate the voltage curve in Figure 6.2. Migration barriers in the kinetic Monte Carlo simulations were calculated by combining the cluster expansion energies of the end points with a constant kinetically resolved activation (KRA) barrier [144, 150, 151, 152, 136]. The barriers of hops between octahedral and tetraheral sites are generally found to scale with the difference in the octahedral and

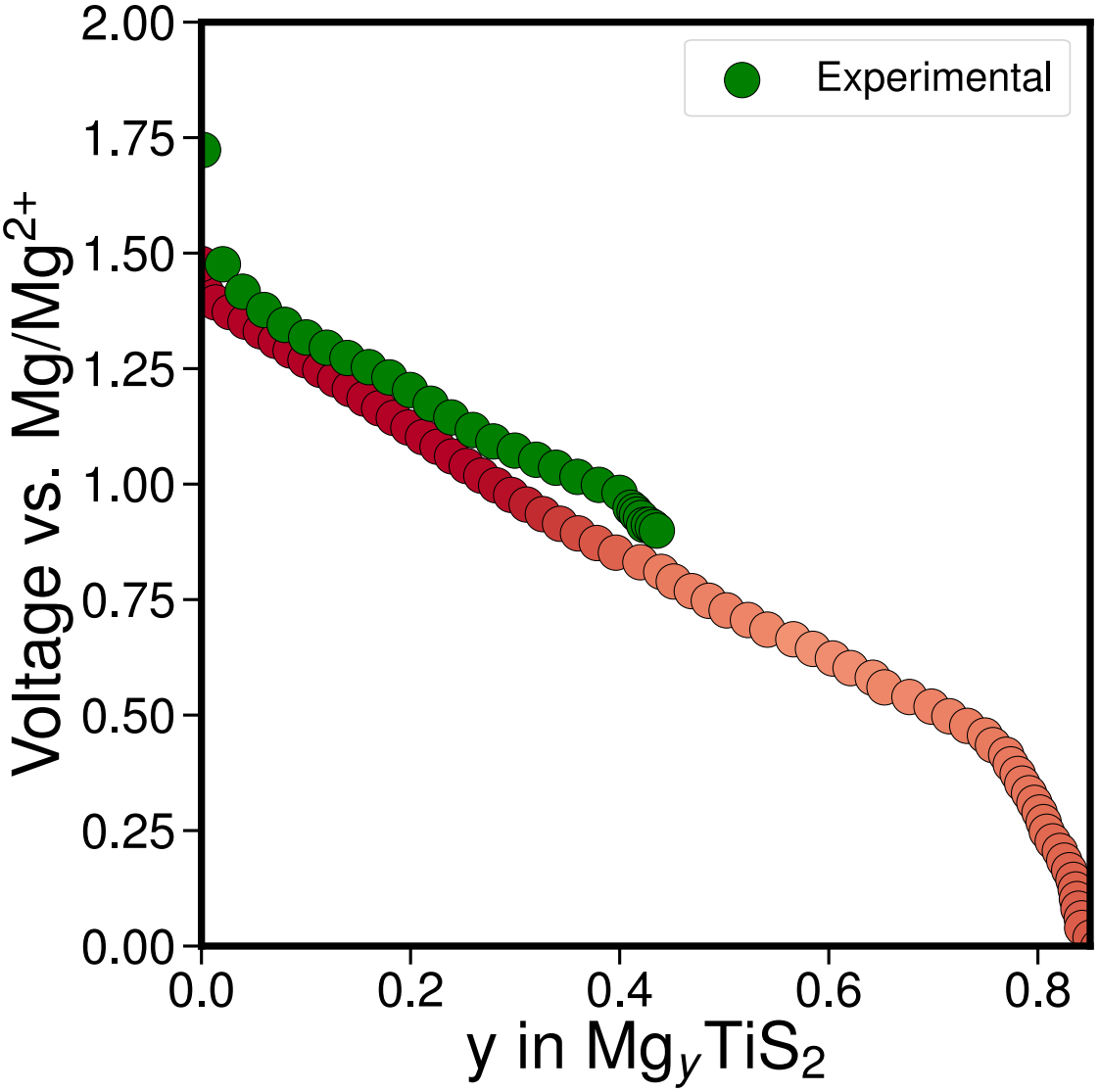

Figure 6.2: The calculated and experimental [118] voltage curve of Mg_yTiS_2. The color of the points in the calculated curve indicates the amount of octahedral site preference (more red is a stronger octahedral preference).

tetrahedral site energies [111]. The use of a constant KRA barrier of 0.5 eV was motivated by several nudged elastic band calculations of migration barriers in spinel Mg_yTiS_2 [147] some of which are shown in Appendix B.

The calculated Mg self-diffusion coefficient in Figure 6.3(a) remains more or less constant below $y = 0.5$, but then decreases by several orders of magnitude in a narrow composition interval. The experimentally measured self-diffusion coefficient by Bonnick *et al.* [118] exhibits a similar variation with composition, although it only extends to $y \approx 0.5$ due to the onset of strong polarization at higher concentrations. Figure 6.3(a) clearly reveals a large quantitative discrepancy between the experimental and calculated self-diffusion coefficient. This discrepancy can be attributed to a variety of factors. The extraction of a diffusion coefficient from galvanostatic intermittent titration technique (GITT) measurements requires an accurate estimate of the active surface area of the electrode particles, for which there is often much uncertainty. Hence the numerical values of reported diffusion coefficients are less reliable than their variation with concentration. The experimental migration barriers as measured in Mg_yTiS_2 are generally more consistent with calculated barriers [147, 118] and, therefore, also more consistent with the lower diffusion coefficients calculated with kMC. The exponential dependence of hop frequencies on migration barriers is a factor that can lead to quantitative uncertainties in the predicted diffusion coefficients [153]. For the purposes of the present discussion, however, only the qualitative variation with concentration is of primary importance.

Insight about the origin of the sudden drop in the Mg self-diffusion coefficient around $y \approx 0.5$ in Mg_yTiS_2 can be obtained by an inspection of the calculated correlation factor, shown in Figure 6.3(b). The correlation factor, f, is a measure of the degree with which successive hops are correlated and is equal to 1 when cations perform an unhindered random walk [136]. Any correlations between successive hops will lead to a correlation factor that is less than 1. In general, the tracer diffusion coefficient will be proportional

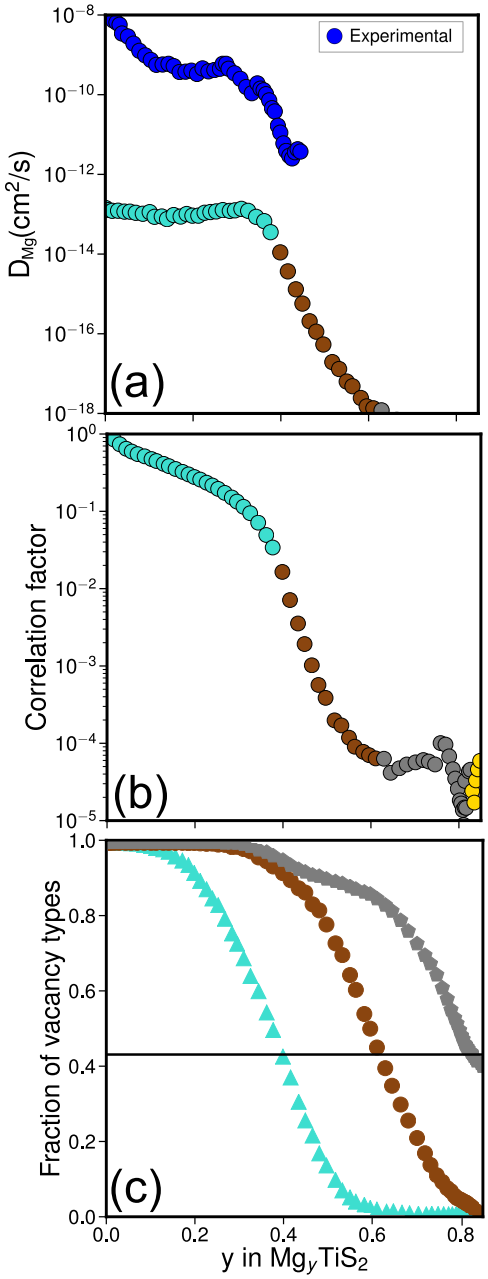

Figure 6.3: (a) The calculated and experimental self-diffusion coefficient of Mg in Mg_yTiS_2 [118]. (b) The calculated correlation factor of Mg in Mg_yTiS_2. (c) The fraction of tetrahedral sites in Mg_yTiS_2 surrounded by 3+ (blue), 2+ (brown), or 1+ (grey) vacancies. The site percolation threshold is marked by a solid black line. The color of the points in (a) and (b) indicates which tetrahedral-vacancy environment is above the site percolation threshold in spinel. This corresponds to the vacancy quantities shown in (c).

to the correlation factor. Figure 6.3(b) shows that, similar to the self-diffusion coefficient in Figure 6.3(a), the calculated correlation factor also decreases by almost four orders of magnitude in a narrow concentration interval around $y \approx 0.5$. This indicates that Mg hops become highly correlated above $y \approx 0.5$.

The cause of the sudden onset of highly correlated diffusion can be traced to the diffusion mechanism in Mg_yTiS_2. Due to the strong dependence of the migration barrier on the number of occupied octahedral sites surrounding the intermediate tetrahedral site, Mg diffusion in spinel TiS_2 is overwhelmingly dominated by triple vacancy hops due to the low barrier compared to double or single vacancy hops. Figure 6.3(c) tracks the fraction of tetrahedral sites with different numbers of vacancies in their four surrounding octahedral sites. The blue curve in Figure 6.3(c) collects the fraction of tetrahedral sites that are surrounded by 3 or 4 octahedral vacancies. The fraction of these tetrahedral sites also decrease rapidly with increasing Mg concentration and they play a crucial role in mediating Mg transport.

A comparison of Figure 6.3(b) and Figure 6.3(c) reveals that the drop in the correlation factor occurs once the triple vacancy concentration dips below the percolation threshold on a diamond network, shown by the horizontal line in Figure 6.3(c). The tetrahedral sites that constitute the intermediate states between neighboring octahedral sites of the spinel form a diamond network and the unhindered diffusion of Mg by means of a triple vacancy mechanism requires a percolating network of quadruple and triple vacancies over the diamond network of tetrahedral sites. Once quadruple and triple vacancies no longer form percolating networks beyond $y \approx 0.5$, the self-diffusion coefficient drops very rapidly and diffusion becomes highly correlated as is evident in Figure 6.3(a) and (b). Beyond that composition, the overwhelming majority of Mg hops continue to be mediated by triple vacancies, but the triple vacancies are disconnected and Mg can only migrate back and forth along disconnected chains.

Similar phenomena were predicted for Li diffusion in spinel TiS_2, however, the diffusion coefficient decreases more gradually and at higher concentrations [111]. A crucial difference between Li and Mg diffusion in spinel TiS_2 is the difference in barriers between the triple vacancy mechanism and the divacancy mechanism. Due to the higher oxidation state of Mg^{2+} cations relative to that of Li^{+}, the repulsion between two Mg ions occupying adjacent tetrahedral and octahedral sites is larger than that between two Li ions. This leads to divacancy migration barriers that are significantly higher than those of triple vacancies in Mg_yTiS_2 (roughly 300 meV). For Li the difference in barriers between triple and divacancy hops is less pronounced (roughly 120 meV). Hence, when the triple vacancy concentration is below the percolation threshold, Li can still escape isolated networks of interconnected triple vacancies with reasonable hop frequencies via divacancy channels, even if they constitute a very small minority of the hops. This behavior is also known to occur in metallurgical alloys, where highly correlated diffusion sets in once the lowest barrier hop environment no longer forms percolating chains [154].

6.3 Parametric study of diffusion in spinel intercalation compounds

The Mg_xTiS_2 example highlights the crucial role that vacancy clusters play in mediating guest ion diffusion within a spinel host. This is a direct consequence of the close-packed anion sublattice of spinel, which constrains cation migration to hops between octahedral and tetrahedral sites. Similar vacancy cluster diffusion mechanisms should, therefore, dominate in other intercalation compounds with close packed anion sublattices such as the disordered rocksalts. To generate a more systematic understanding of diffusion mechanisms in hosts with close-packed anion sublattices of differing chemistries,

we next perform a parametric study of diffusion with kMC applied to simple lattice models that capture the essential thermodynamic and kinetic properties of intercalation compounds with close-packed anion sublattices.

We continue to use spinel as a model system as it serves as an idealization of disordered rocksalts in which all 0-TM tetrahedral sites belong to fully percolating channels. Simple lattice models are able to capture most of the essential electrochemical properties that emerge upon inserting guest ions into a spinel host crystal structure. The spinel crystal structure has twice as many non-face sharing octahedral sites (16c sites of the $Fd\bar{3}m$ space group) as non-face sharing tetrahedral sites (8a sites). The tetrahedral sites form a diamond network while the octahedral sites reside between pairs of tetrahedral sites. Each tetrahedral site is coordinated by four octahedral sites, while each octahedral site is coordinated by two tetrahedral sites.

6.3.1 Electrochemical properties

Guest ions within spinel will generally have a preference for either the tetrahedral site or the octahedral site. This site preference is determined by a difference in the energy ΔE_{t-o} between the octahedral site and the tetrahedral site. A positive (negative) ΔE_{t-o} signifies octahedral (tetrahedral) site preference. We can also introduce a nearest neighbor pair interaction between an adjacent pair of octahedral and tetrahedral sites V_{t-o}. This interaction, when positive, describes a repulsion between two guest cations when they occupy a nearest neighbor pair of tetrahedral and octahedral sites. Additional interactions can further refine the model, such as an interaction between nearest neighbor octahedral sites, V_{o-o}, and an interaction between nearest neighbor tetrahedral sites, V_{t-t}, along with other multi-site terms and longer range interactions. The interactions define

a lattice model Hamiltonian that can be written as

$$E = \sum_i V_t \sigma_i + \sum_j V_o \sigma_j + \sum_{i,j} V_{t-o} \sigma_i \sigma_j + \dots \tag{6.1}$$

where the σ_i and σ_j represent occupation variables assigned to each tetrahedral site i and octahedral site j within the crystal (σ_i is equal to 1 when a guest cation occupies site i and zero when the site is vacant). The coefficients V_o and V_t are equal to the dilute site energies of the octahedral and tetrahedral sites respectively with $\Delta E_{t-o} = V_t - V_o$. The simple lattice model Hamiltonian in Equation (6.1) lists the first few terms of a more general cluster expansion Hamiltonian [17, 151, 136]. The expansion coefficients of a cluster expansion can be trained to a database of first-principles energies for a large number of different cation vacancy orderings. The resultant Hamiltonian then describes the energy of a particular chemistry as a function of cation-vacancy orderings [148, 149, 93]. Instead of focusing on a particular chemistry, we next study simple lattice model Hamiltonians parametrically to understand how different interaction coefficients affect thermodynamic and cation transport properties.

To first order, only two independent interaction parameters are needed to predict commonly observed experimental voltage curves exhibited by spinel compounds. These are the site preference energy parameter ΔE_{t-o} and the nearest-neighbor octahedral-tetrahedral pair interaction V_{t-o}. Figure 6.4 maps out the regions in ΔE_{t-o} and V_{t-o} space corresponding to qualitatively distinct voltage profiles for the spinel host. The voltage curves were calculated with grand canonical Monte Carlo simulations applied to the simple lattice model Hamiltonian over a grid of ΔE_{t-o} and V_{t-o} values. Four regions with distinct voltage profiles are evident in Figure 6.4. The site occupancy is shown by the shade of color in the voltage curve, with blue (red) reflecting tetrahedral (octahedral) occupancy and white signifying mixed occupancy.

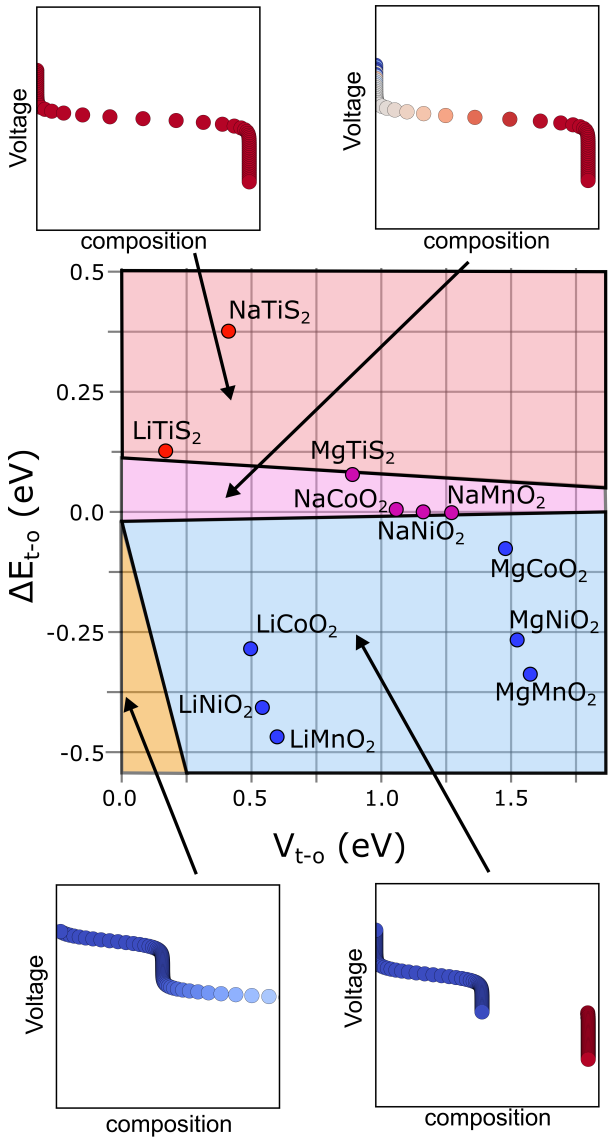

Figure 6.4: A map of characteristic voltage curves based on the relative energies of the tetrahedral and octahedral interstitial sites and the effective cluster interaction (ECI) of the nearest-neighbor octahedral-tetrahedral pair cluster in the spinel network. Some notable chemistries have been placed roughly in the correct regions of their characteristic voltage curve and ECI values for reference. Some notable chemistries have been placed roughly in the correct regions of their characteristic voltage curve and ECI values for reference.

For positive ΔE_{t-o}, where the octahedral sites are energetically preferred, cation insertion is predicted to proceed through a solid solution, as reflected by the smooth sloping voltage profile [136]. The guest cations gradually fill the octahedral sites until they are completely filled at $x = 1$. When ΔE_{t-o} is small but still positive, reflecting host and guest chemistries where tetrahedral and octahedral sites are close in energy, thermal excitations will lead to some degree of tetrahedral site occupancy. The nearest neighbor V_{t-o} interaction has little effect on the voltage curves when octahedral sites are preferred.

Negative values of ΔE_{t-o} correspond to a tetrahedral site preference. In this case, the tetrahedral sites fill first until they are completely saturated at x=1/2. Beyond that point the less favorable, but more numerous, octahedral sites must be filled. This leads to a voltage step at $x = 1/2$, as a certain energy is needed to overcome ΔE_{t-o} before octahedral sites can be filled. The qualitative shape of the voltage curve depends on the value of the nearest neighbor V_{t-o} pair interaction.

When V_{t-o} is small or negligible, guest cations will simply fill the octahedral sites as a solid solution beyond $x = 1/2$ without displacing tetrahedral cations as the simultaneous occupation of nearest neighbor tetrahedral and octahedral sites is easily tolerated. However, when V_{t-o} becomes large and positive, nearest neighbor tetrahedral-octahedral pairs become too costly for simultaneous occupancy and the filling of the more numerous octahedral sites is accompanied by a displacement of tetrahedral cations. This is predicted to occur through a two-phase reaction as is evident by the plateau in the voltage curve between $x = 1/2$ and $x = 1$.

More complex insertion sequences emerge upon the addition of longer-range and multi-site interactions to the lattice model Hamiltonian. For example, the inclusion of a strong repulsion between nearest neighbor octahedral sites, V_{o-o}, when ΔE_{t-o} is positive but not too large will lead to an increase in tetrahedral site occupancy at guest

cation concentrations of $x \approx 0.4$. A mix of octahedral and tetrahedral occupancy at intermediate concentrations allows for an increase in the spacing between cations, and thereby a minimization of occupied nearest neighbor octahedral-octahedral pairs to avoid the repulsive V_{o-o} interactions. If the repulsive V_{o-o} interactions are larger than ΔE_{t-o}, then mixed occupancy can be expected, as the penalty of occupying unfavorable tetrahedral sites is smaller than having nearest neighbor octahedra-octahedral occupancy. This occurs in systems such as Mg_xTiS_2 [147], where the strong electrostatic interactions due to the high oxidation state of the Mg^{2+} leads to a large V_{o-o} pair interaction [149]. Other examples of how additional interactions can introduce more features to the voltage profile and site occupancy are shown in Appendix B.

Figure 6.4 also shows a first order estimate of where different spinel and guest ion chemistries fall in the low-dimensional ΔE_{t-o} and V_{t-o} parameter space. The placement of each chemistry in this map was informed by the results of past studies using density functional theory calculations [93]. The smaller guest cations such as Li and Mg tend to prefer tetrahedral sites in the more ionic oxide spinel hosts. Since Mg has a higher oxidation state than Li, its nearest neighbor V_{t-o} interaction coefficient will be larger than that for Li. In a sulfide spinel such as TiS_2, which is more covalent than the oxide spinels, guest cations prefer the octahedral sites. The tetrahedral sites are penalized when the guest cation is large. Na insertion into an oxide spinel results in a ΔE_{t-o} that is close to zero, with tetrahedral and octahedral sites having similar energies. In the TiS_2 spinel, however, the energy of occupying a tetrahedral site is significantly higher than in an octahedral site. The placement of the different chemistries in this map should be viewed as a projection from a much higher dimensional parameter space. To capture many of the subtle nuances exhibited by each individual chemistry, it is necessary to include many more interaction parameters that extend beyond the site and nearest neighbor pair interaction [93]. Nevertheless, many of the essential features of these chemistries are

already captured with a two-interaction parameter lattice model Hamiltonian.

6.3.2 Diffusion in spinels

Having mapped out how the thermodynamic properties of spinel intercalation compounds depend on the interaction coefficients of a simple lattice model Hamiltonian, we next explore how guest cation diffusion is affected by the interaction coefficients. The Mg_xTiS_2 example shows that the self-diffusion coefficient drops by several orders of magnitude once the triple vacancy concentration falls below the percolation threshold. This behavior is undesirable for battery applications. It occurs because the migration barriers for divacancy and single vacancy hops are significantly higher than the barriers for triple vacancy hops. Once the concentration of triple vacancies falls below the percolation threshold, the cations are trapped in disconnected chains of triple vacancies. In order to escape, they must migrate into divacancy or single vacancy clusters, which will only occur to a sufficient degree if the barriers for these hops are not significantly higher than those of hops into triple vacancies. To first order, the barriers associated with different vacancy clusters can be tuned by varying V_{t-o}, the interaction between nearest neighbor tetrahedral and octahedral sites. We again used kinetic Monte Carlo simulations in which the energies of the end points of the hops are calculated with the lattice model Hamiltonian of Equation (6.1). The barriers within the kMC simulations were calculated with a constant KRA of 0.3 eV.

We first consider the case when V_{t-o} is zero and $\Delta E_{t-o} > 0$. Octahedral sites are then favored, but the energy of the tetrahedral site is unaffected by the number of occupied nearest neighbor octahedral sites. The triple vacancy, divacancy and single vacancy hops then all have an identical migration barrier. The calculated self (jump) diffusion coefficient and accompanying correlation factor are shown in Figure 6.5(a). While the self-

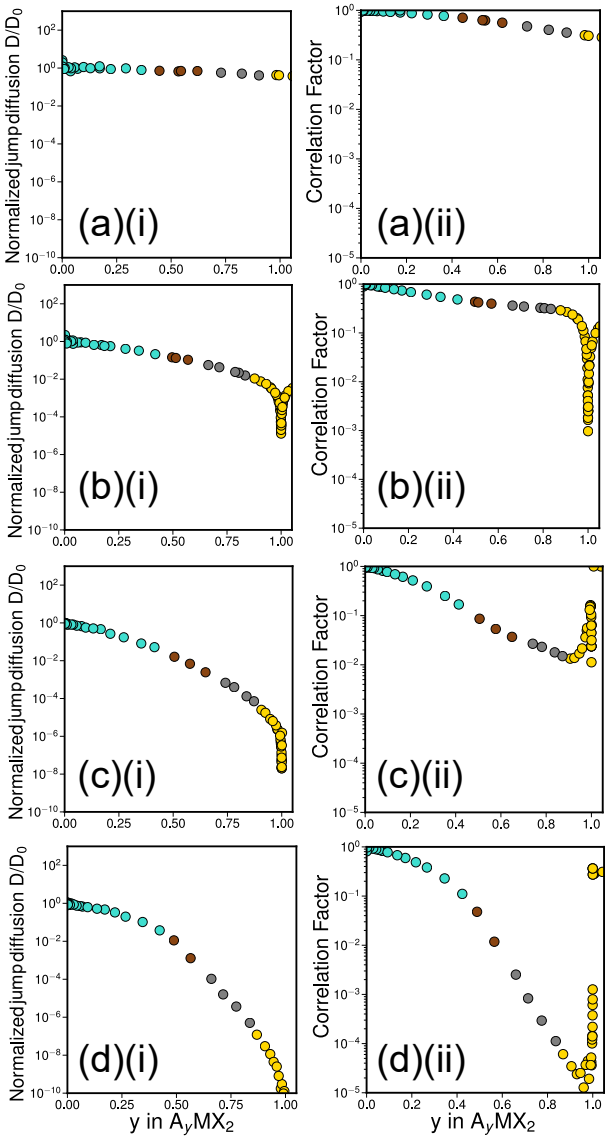

Figure 6.5: The jump diffusion coefficient and the correlation factor (a)$V_{t-o} = 0$ eV, (b)$V_{t-o} = 0.1$ eV, (c)$V_{t-o} = 0.25$ eV, and (d) $V_{t-o} = 0.75$ eV. Points are colored based on the type of vacancy above the percolation threshold.

diffusion coefficient decreases with increasing cation concentration, the chemical diffusion coefficient, obtained by multiplying the self-diffusion coefficient by the thermodynamic factor, is a constant, independent of cation concentration. Figure 6.5(b) shows the calculated transport coefficients and correlation factor for a slightly positive V_{t-o}. In this case there is a difference between the triple-vacancy, divacancy and single vacancy migration barriers. The difference is not too large (relative to k_BT where k_B is Boltzmann's constant and T is the absolute temperature), and divacancy hops are still accessible. While the majority of hops are mediated by triple-vacancies, once the percolation threshold for triple vacancies is reached, cations can still escape from isolated triple-vacancy chains by hopping into divacancies. Hence the correlation factor does not drop precipitously in a narrow concentration range and the diffusion coefficients do not vary more than one to two orders of magnitude with concentration. When V_{t-o} is positive and large (Figure 6.5(c)-(d)), the calculated transport coefficients decrease more significantly. The self-diffusion coefficient and the correlation factor drops by multiple orders of magnitude once the triple vacancy concentration dips below the percolation threshold in spinel. The drop, however, is not as abrupt as predicted for Mg_xTiS_2.

We next explore the effect of adding a repulsive interaction between nearest neighbor octahedral sites, V_{o-o}. We consider two scenarios. The first is for a small ΔE_{t-o}, which leads to a small difference in energy between tetrahedral and octahedral site occupancy. In this case, a positive V_{o-o} leads to some degree of tetrahedral site occupancy between $x = 0.3$ and $x = 0.6$ as described in the previous section. The second scenario is for a larger ΔE_{t-o}, which is chosen sufficiently large to suppress any appreciable tetrahedral occupancy even with a positive V_{o-o}. The calculated diffusion coefficients and correlation factors for both scenarios are shown in Figure 6.6(c) - (f). In both cases, there is a dramatic drop in both the self-diffusion coefficient and the correlation factor over a very narrow concentration interval, which is significantly more pronounced than in the cases

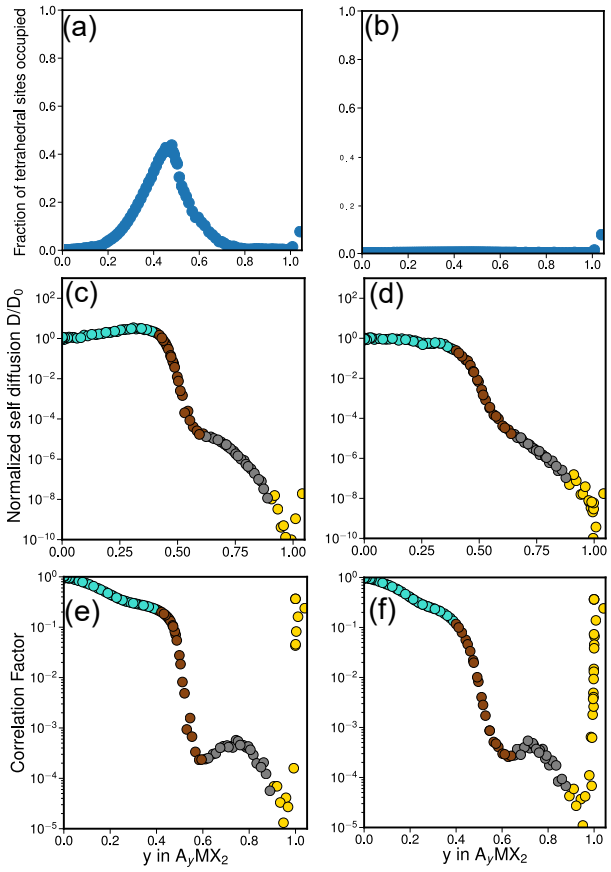

Figure 6.6: The fraction of tetrahedral sites for (a) a small ΔE_{t-o} and (b) a large ΔE_{t-o}. The diffusion coefficient for (c) a small ΔE_{t-o} and (d) a large ΔE_{t-o}. The correlation factor for (e) a small ΔE_{t-o} and (f) a large ΔE_{t-o}. Points are colored based on the type of vacancy above the percolation threshold.

without a V_{o-o} interaction. The curves for the two scenarios with positive V_{o-o} are very similar in spite of the fact that there is significant tetrahedral site occupancy in the first scenario. This suggests that the effect of tetrahedral site occupancy (to the extent predicted for the first scenario) is not especially large in determining transport coefficients. Instead, it is a positive V_{o-o} that leads to an increase in correlated motion over a narrow concentration interval around the percolation threshold of triple vacancies. A positive V_{o-o} further constricts the diffusion of cations as it will bias hops to octahedral sites that do not have occupied nearest neighbor octahedral sites. These become increasingly rare with increasing cation concentration.

6.4 Discussion and Conclusion

The results of this study show that the guest cation diffusion coefficient of an intercalation compound with a close-packed anion sublattice can drop abruptly at intermediate to high cation concentrations, a property that is undesirable for battery applications. Cation diffusion in a host with a close-packed anion sublattice occurs through a succession of hops between octahedral and tetrahedral sites. When cations prefer octahedral sites, they must pass through higher energy tetrahedral sites as they migrate through the crystal. In spinel and disordered rocksalts with fully percolating 0-TM networks, these tetrahedral sites are four-fold coordinated. It is this topological feature of the close-packed anion sublattice that leads to a cation diffusion mechanism that is mediated by vacancy clusters, primarily triple vacancies but also a small fraction of divacancies. This is because the migration barrier, which scales with the tetrahedral site energy, is strongly affected by the number of other cations that occupy adjacent octahedral sites: The barrier to hop into a triple vacancy is lower than that of hopping into a divacancy, which is itself lower than the barrier to hop into a single vacancy as schematically illus-

trated in Figure 6.1. The concentration of triple vacancies and divacancies decreases with increasing guest cation concentration and when diffusion is primarily mediated by triple vacancies and divacancies, a decrease in their concentration can result in a significant drop in the diffusion coefficient.

Our kinetic Monte Carlo simulations on model spinel systems have revealed that the abruptness of the decrease in the cation diffusion coefficient depends on the strength of the nearest neighbor repulsion between guest cations. In the absence of a nearest-neighbor repulsion (i.e. $V_{t-o} = 0$), the migration barrier is independent of the hop environment (i.e. the migration barriers for the triple vacancy, divacancy and single vacancy hops are all identical) and the self-diffusion coefficient scales as $(1 - y)$, where y is the cation concentration in spinel (Figure 6.5(a)). Once a repulsion between cations in nearest neighbor octahedral and tetrahedral sites is turned on, the migration barriers for triple vacancy, divacancy and single vacancy hops begin to differ. The stronger this nearest neighbor repulsion, the more the migration barrier depends on the surrounding environment and the larger the differences between the triple, di and single vacancy hops. This results in a self-diffusion coefficient that decreases more rapidly with y than $(1 - y)$ as is evident in Figure 6.5(b)-(d).

While the concentration of vacancy clusters has an influence on the cation diffusion coefficient, the kMC simulations for spinel show that this influence manifests itself in a significant way only after the concentration of diffusion mediating defects falls below the percolation threshold of a diamond network, the network of the sublattice of 0-TM tetrahedral sites in spinel. It is at this point that the correlation factor can decrease by several orders of magnitude and cation diffusion becomes highly correlated and inefficient. When the nearest-neighbor repulsion is large, the difference in the migration barrier of a triple vacancy and a divacancy hop is large and diffusion is dominated almost exclusively by triple vacancies. Once the fraction of quadruple and triple vacancies surrounding tetrahe-

dral sites falls below the percolation threshold at approximately $y \approx 0.5$, cation diffusion becomes primarily restricted to disconnected chains of quadruple and triple vacancies. This severely reduces the mobility of the guest cations, as manifested by a rapid decrease in the self-diffusion coefficient. The decrease in the self-diffusion coefficient becomes even more abrupt upon turning on a repulsive interaction between nearest neighbor octahedral sites (V_{o-o}) as this further restricts the trajectories of cations, causing a sudden decrease in the correlation factor. In Mg_yTiS_2, the effect is especially pronounced and leads to a four orders of magnitude drop in the self-diffusion coefficient around $y \approx 0.5$. In contrast, when the barriers to hop into divacancies are not much larger than those of hopping into triple vacancies, diffusing cations are more often able to escape disconnected chains of quadruple and triple vacancies, and the decrease in the diffusion coefficient is not as severe. This appears to be the case for Li_yTiS_2, where the decrease in the Li diffusion coefficient is not as sudden and dramatic as that of Mg in Mg_yTiS_2 [111].

Our results suggest ways in which the concentration dependence of the cation diffusion coefficient can be tuned in hosts with close-packed anion sublattices. The key is to modify the strength of the nearest neighbor repulsion between cations that simultaneously occupy adjacent tetrahedral and octahedral sites. This nearest neighbor repulsion is to an important degree affected by the oxidation state of the cation. For example, Li^+ and Mg^{2+} have approximately the same ionic radii but a different oxidation state, leading to different intercalation behavior that arises from differences in the strength of repulsive interactions due to their oxidation state [155]. The study of Bonnick *et al.* of Li_yTiS_2 and Mg_yTiS_2 clearly showed a significant difference between the Li and Mg diffusion coefficients that is consistent with the predictions of this work [118]. The nearest neighbor repulsion can also be screened to some extent by using larger and more covalent anions, such as sulfur instead of oxygen. Furthermore, the ionic versus covalent nature of the close-packed anion host likely has an affect on the nearest neighbor interaction and can

be tuned with transition metal chemistry [93].

Although we have only explicitly simulated diffusion in spinel hosts in which guest cations prefer octahedral sites, many of the results and conclusions of this study should help elucidate subtleties about cation diffusion mechanisms in disordered rocksalts. There is currently much interest in oxide disordered rocksalts (DRX) as candidate electrodes for Li-ion batteries. They are made Li-excess and, therefore, transition metal deficient, to ensure a sufficient number of 0-TM tetrahedral sites to form fully percolating networks of facile Li diffusion environments. The recently developed Li-excess oxyfluorides that have partial spinel ordering have also exhibited very high capacities and, in contrast to the oxide disordered rocksalts, very high rate capabilities. While Li ions in oxide spinels prefer tetrahedral sites (i.e. $\Delta E_{t-o} < 0$), the disorder among the transition metal cations of disordered rocksalts and oxyfluoride partially ordered spinels tends to shift the Li site preference from tetrahedral sites to octahedral sites, even when the Li concentration is below the maximum number of available 0-TM sites.

Similar to perfectly ordered spinel with octahedral site preference, we expect a decrease in the DRX Li diffusion coefficient at high concentrations due to the onset of highly correlated diffusion once the concentration of low barrier vacancy clusters fall below a percolation threshold. However, the percolation threshold of DRX is likely to differ from that of perfectly ordered spinel. The TM depletion of Li-excess disordered rocksalts opens up more 0-TM tetrahedral sites and produces a more disordered sublattice of 0-TM sites when compared to the diamond network of 0-TM sites in spinel. An increase in the connectivity of the 0-TM network will lower the percolation threshold above which the concentration of quadruple and triple vacancies must be kept to maintain fully interconnected chains of favorable diffusion pathways. Generally the percolation threshold can be reduced by increasing the coordination number of each site of a particular network. For example, the percolation threshold of diamond, which has a coordination number of

4, is 0.4286, while those of bcc and fcc, which have coordination numbers of 8 and 12, are 0.2458 and 0.1994, respectively [156]. The disorder among transition metal cations and the increased concentration of available octahedral sites in Li-excess DRX is also likely to affect the difference in migration barriers for triple, di- and single vacancy hops. The extent to which this is the case can be investigated with first-principles electronic structure calculations.

Chapter 7

Summary

In this thesis, we used crystallographic mapping algorithms, web scraping, and density functional theory (DFT) to study the relationships between the most common binary intermetallic structures. We also used DFT, cluster expansion methods, and statistical mechanics via Monte Carlo to study spinel intercalation compounds for electrochemical storage.

In chapter 3, we distilled crystallographic information from the Inorganic Crystal Structure Database (ICSD) and the Materials project to the most important parent crystal structures and reported on the chemistries that formed chemical orderings on each parent crystal. We found that $\approx 74\%$ of intermetallics can be considered orderings on 20 different parent crystals. While some of these were simple structures like bcc, fcc, and hcp, many were orderings on more complex structures. This organization into parent crystals will help expedite alloy research by exploiting this hierarchy using high-throughput cluster expansion studies.

In chapter 4, we examine these top 20 most common parent crystal structures for crystallographic relationships that lend themselves to martensitic transformations. We find that there are 5 special orderings on simple crystal structures fcc, bcc, hcp, and ω

that are dynamically unstable given certain element choices. These orderings result in 7 newly reported transformation pathways similar to those of the Bain path, Burgers path, Trinkle path, and Natarajan paths. We examine the prevalence of these pathways using high-throughput DFT to examine for which alloy systems the pathways may be most relevant. We suggest some alloy systems where experimental evidence that corroborates these pathways could be collected.

In chapter 5, we examine the thermodynamic properties of various spinel intercalation compounds using cluster expansion methods. We examine the effects of guest cation valence, guest ion size, and host ionicity on the electrochemical behavior of spinel. We find that increasing guest cation size or valence tends to favor octahedral sites, where increasing host ionicity tends to promote tetrahedral occupation. Tuning these parameters together can result in a spinel chemistry that has a smooth energy landscape where tetrahedral and octahedral sites are close in energy allowing for solid solution intercalation behavior and smooth voltage curves.

In chapter 6, we examine the kinetic properties of spinel intercalation compounds using kinetic Monte Carlo methods. We use a parametric analysis to explains Li^{+}, Na^{+}, and Mg^{2+} transport in close-packed anion structures like layered-NaFeO2, spinel LT-LiCoO2, and disordered rocksalts (DRX). Diffusion is dependent on the percolation of precise local environments along an octahedral-tetrahedral-octahedral (o-t-o) interstitial diffusion path. We examine how changes the energy landscape affect the kinetic properties of a generic spinel intercalation compound. We find that the correlation factor and the diffusion coefficient drop dramatically (2-5 orders of magnitude) in cases where there is a large nearest-neighbor repulsion that causes large vacancy environments to dominate diffusion. Although this study focuses on the spinel structure, the conclusions drawn here apply to other close-packed anion hosts used for electrochemical applications such as disordered rocksalt electrodes and layered transition metal oxides.

Appendix A

Crystallographical Appendix

A.1 Generating the library of parent crystals

Two structures should be considered the same if there is a low mapping score between them. This is apparent, for example, in the case of $L1_0$; despite it having a slight tetragonal distortion of the lattice in most chemistries, it should still be considered a chemical ordering on FCC. Using structure comparison metrics we are able to create a cataloging algorithm that groups structures that are close in long range periodicity as well as local atomic environments. While collecting structures into sets, we select a representative in the set to become the fundamental parent crystal. The chosen representative is one from which all other structures in the set could be generated as derivative structures (i.e. if given pure FCC, $L1_2$, and $L1_0$ we wish to select pure FCC). The highest symmetry crystal of the set might not satisfy this criterion without some alteration. We have developed an algorithm that can refine the symmetry of a provided structure. If a structure set was limited to $L1_0$ and $D0_{23}$, the symmetrization algorithm would adjust $L1_0$ to remove its small tetragonal distortion and suggest FCC as the candidate parent crystal to represent both $L1_0$ and $D0_{23}$. This algorithm is described in more detail in the following section.

Once we have obtained a high symmetry representative, we can use that as a reference structure to calculate the mapping scores of all the structures in the set. The reference structures for various sets are kept in a growing list of fundamental parent crystal structures. The generation of these parent crystals is done in an iterative process shown in Figure A.1.

A.1.1 Symmetrization

Symmetrization routines can be helpful when using an observed structure from a database to create a new parent structure. Observed structures can have any amount of displacement or strain relaxations due to the chemistry of the structure. These relaxations can lower the symmetry to various degrees depending on the chemistry. If there are only small relaxations, then it is best to adjust the lattice and basis of the structure to a higher symmetry state before that structure is classified as a parent crystal. A symmetry operation is part of the space group of a crystal if the operation is applied to the lattice and basis of the crystal and the difference between the positions of the transformed atoms and the positions of the original atoms is within a certain distance tolerance. As the distance tolerance increases, more operations become part of the crystalline space group by this criterion. If the space group is calculated with a relaxed distance tolerance, it could have more symmetry operations. Using the new space group, one can apply each operation in the group to the crystal to generate a set of equivalent structures. The average of the lattice and coordinates of all of generated equivalent structures is a higher symmetry version of the original crystal.

In this study, the symmetrization tolerance for constructing new parent prototypes was kept to 0.1 Å. The threshold mapping score for deciding whether or not to add a new prototype parent crystal was 0.1.

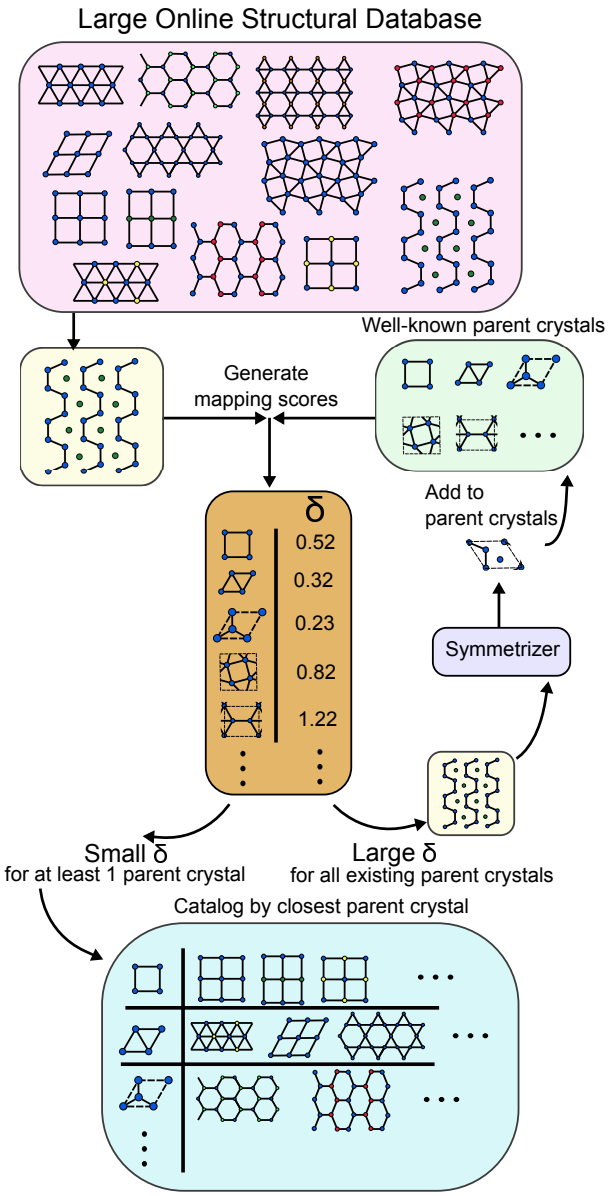

Figure A.1: A schematic of the iterative cataloging algorithm that separates a large amount of chemical compounds into sufficiently distinct fundamental parent crystal structures. New parent crystal structures are created when the mapping score to all existing reference structures is above a certain threshold.

A.2 Parent crystal structures in terms of two-dimensional building blocks

It is often convenient to characterize a particular crystal structure as a stacking of layered motifs. Fifteen of the top twenty parent crystal structures can be described in this manner. This is summarized in Table 1 of the main text, which lists the layer sequence for each of the top twenty parent crystal structures.

Several of the parent crystals consist of triangular, honeycomb and/or kagomé layers as illustrated in Figure A.2. A distinction must be made between close-packed triangular layers, shown in Figure A.2(a), and non-close packed triangular layers, derived by retaining one third of the sites of a close-packed layer that form a $\sqrt{3}a \times \sqrt{3}a$ superlattice as shown in Figure A.2(b) (a is the nearest neighbor distance on the close-packed triangular lattice). Each triangular layer has multiple translational variants, referred to as A, B and C for the close-packed triangular layers and a, b and c for the non-close-packed layers. The honeycomb layer of Figure A.2(c) and the kagomé layer of Figure A.2(d) also have three translational variants. These are referred to as H_a, H_b and H_c for the honeycomb layers and α, β and γ for the kagomé layers.

The FCC, HCP and DHCP (double HCP) crystals are made up of close-packed triangular layers (Figure A.2(a)) having ABC, ABAB and ABAC stacking sequences, respectively. The ω parent crystal structure is slightly more complex. It is made up of honeycomb layers (Figure A.2(c)) interleaved by non-close-packed triangular layers (Figure A.2(b)) with a aH_aaH_a stacking sequence. The parent crystals that belong to the family of Laves phases, including $CaCu_5$, C15, C14, and Be_3Nb, consist of different stacking sequences of close-packed triangular, non-close-packed triangular and kagomé layers (Figure A.2(d)). Their stacking sequences are listed in Table 1 of the main text. Figure A.3 shows the relative alignment of a triangular layer a and honeycomb layer H_a as

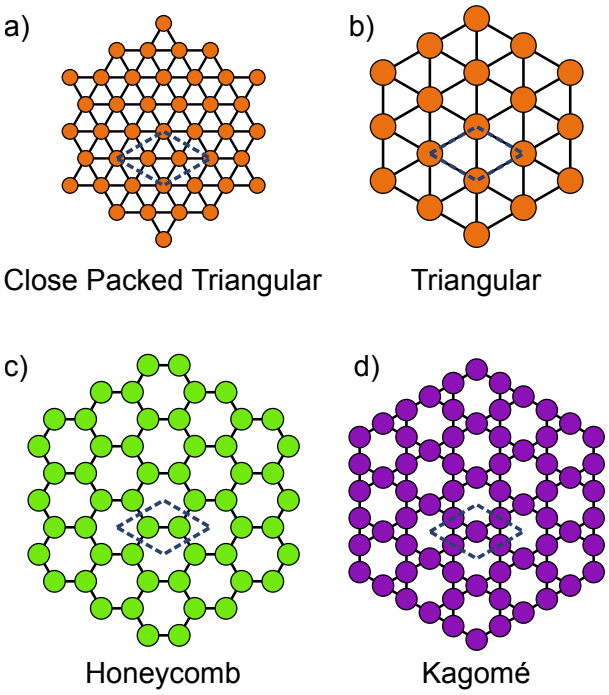

Figure A.2: Depictions of a) close-packed triangular, b) triangular, c) honeycomb and d) kagomé layers as seen from above. There are up to 3 translational variants of each of these layers in each parent crystal that contains them. The variants of close packed triangular layers and sparse triangular layers are denoted A/B/C and a/b/c respectively. Honeycomb variants are labelled H_a, H_b, and H_c while kagomé variants are labelled α, β, and γ.

they appear in the ω crystal, an a triangular and an α kagomé layer as in Laves C15, and an A triangular and an α kagomé layer as in the $CaCu_5$ crystal.

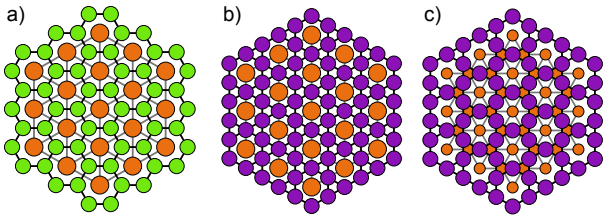

Figure A.3: The alignment of a) a triangular layer with a honeycomb layer, b) a triangular layer with a kagomé layer and c) a close-packed triangular layer with a kagomé layer as they appear in ω, Laves C15, and $CaCu_5$ respectively.

The structures of AlTh, $CeCu_2$, NiY, Cementite, and Co_2Si are also layered, but each are a stacking of a single type of layer that is unique to their structure. Their two-

dimensional layering motifs are illustrated in Figure A.4. Finally, the crystal structures of Al_2Cu and σ both contain the 3-3-4-3-4 Frank-Kasper [157, 158] type layers shown in Figure A.5(b) that are alternated by a square lattice (Figure A.5(a)) in Al_2Cu and the two-dimensional pattern of (Figure A.5(c)) in the σ phase. The relative stacking of the different layers are illustrated in Figure A.6.

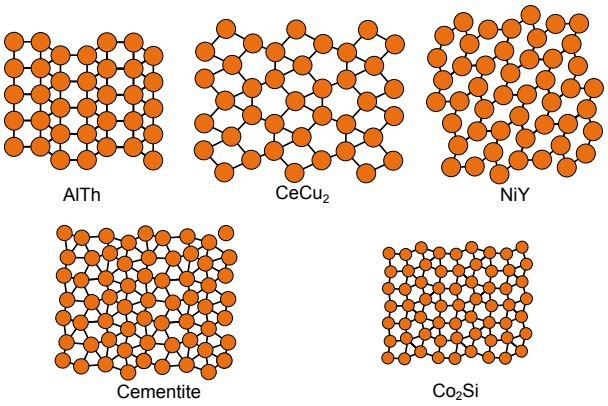

Figure A.4: Depictions of the unique layers within AlTh, $CeCu_2$, NiY, Cementite, and Co_2Si as seen from above. These single layers are staggered along the out of plane direction in each of the representative parent crystals.

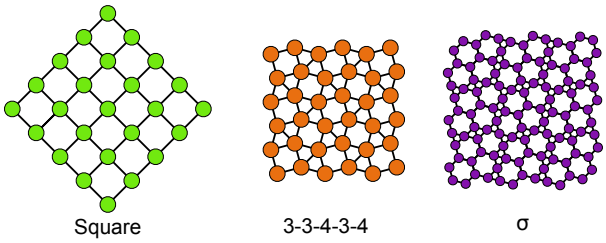

Figure A.5: Depictions of square, Frank-Kasper 3-3-4-3-4 and a layer unique to σ as seen from above. The square layer is denoted with an S in layering schemes. The 3-3-4-3-4 layer has two translational variants that we label θ_a and θ_b. The two 180° rotational variants of the σ layer are marked as σ_0 and σ_π

The remaining crystal structures in the top twenty common are not very well described in terms of layers. BCC at the top of the list is a more open structure when compared to other simple close-packed structures such as FCC and HCP. A15, Yb_6Fe_{23}, $LuBe_{13}$, and Al_8Cr_5 can be viewed as a three dimensional network of connected atoms that can

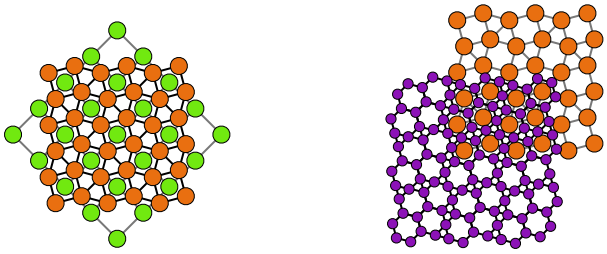

Figure A.6: The alignment of the 3-3-4-3-4 layer with the square layer in Al_2Cu (left) and the σ layer in the σ parent (right). There are two translational variants of 3-3-4-3-4 in Al_2Cu (θ_a and θ_b). There are two rotational variants of the σ layer (σ_0 and σ_π).

be represented by space filling polyhedra.

A.3 $CaCu_5$ Dumbbell Description

Figure A.7 shows the crystal structure of $CaCu_5$ consisting of alternating layers of dense triangular lattices and kagomé layers. The smaller Cu atoms (purple) occupy all the kagomé layer sites and two-thirds of the triangular layer sites, while the larger Ca atoms (orange) occupy the remaining one third of the close-packed triangular layer sites directly above and below the hexagonal openings of the adjacent kagomé layers. Figure A.7 schematically shows how the $Ni_{17}Th_2$, $Mn_{12}Th$, and Th_2Zn_{17} prototypes can be generated from $CaCu_5$ by replacing a subset of the orange sites with dumbbells of the smaller purple atoms oriented perpendicular to the layers. By allowing for this generalization of superstructure ordering, the $CaCu_5$ parent crystal structure becomes an important parent crystal structure since the $Ni_{17}Th_2$, Th_2Zn_{17}, and $Mn_{12}Th$ prototypes each appear with an appreciable frequency when compared to other well-known structures.

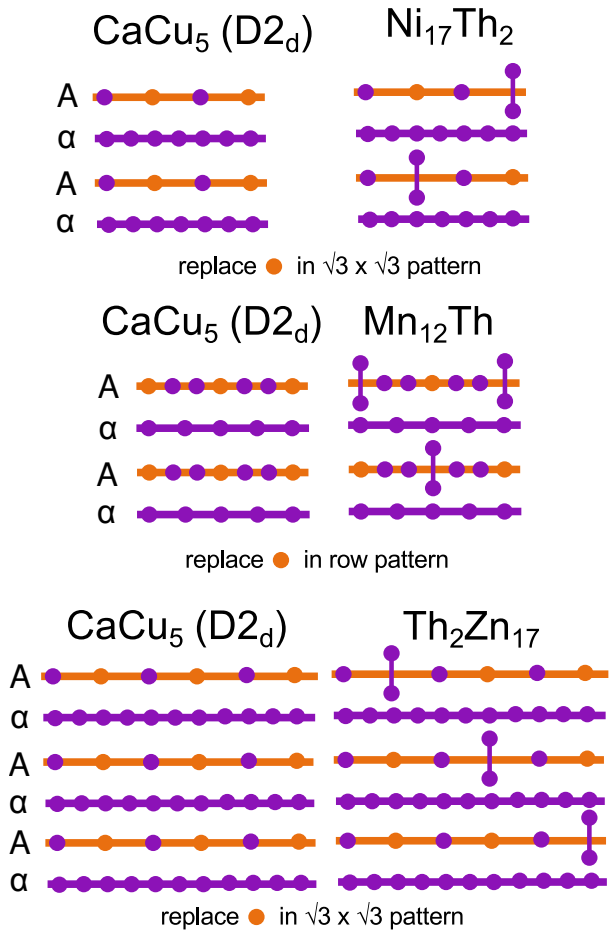

Figure A.7: The relationship between phases we call "dumbbell phases" and the simpler motif, $CaCu_5$. In order to form dumbbell phases, the larger orange atom in the $D2_d$ ordering is periodically replaced with a dumbbell of the smaller atom in the structure that lies out of plane (parallel to c-axis).

A.4 Chemistry Distributions Among Top Twenty Hosts

The top twenty most common parent crystals form for different reasons. It is illustrative to examine the chemistries that adopt these parent crystals to probe the mechanisms upon which they form. We can simplify the chemical trends that are associated with specific parent crystals by reducing the chemical trends to atomic radius ratio and electronegativity difference of the two constituent elements of each binary compound. The distribution of radius ratio and electronegativity difference for each of the top twenty

parent crystals are shown in Figure A.8 - Figure A.27. In each of these figures a reference circle that roughly indicates the location of the distribution of one of the parent crystals is shown. The reference circle is different for each plot. Upon inspection many close-packed parent crystals show distributions that are centered near a radius ratio of 1. In contrast, parent crystals that tend to look like Laves phases show distributions that are centered near radius ratios of 1.3. Parent crystals that show similar distributions may have the same underlying driving forces for their formation.

Figure A.8: Contour plots of the kernel density estimates (KDEs) of the distributions of atomic radius ratio and electronegativity difference for the top twenty parent crystals. The reference circle is for BCC.

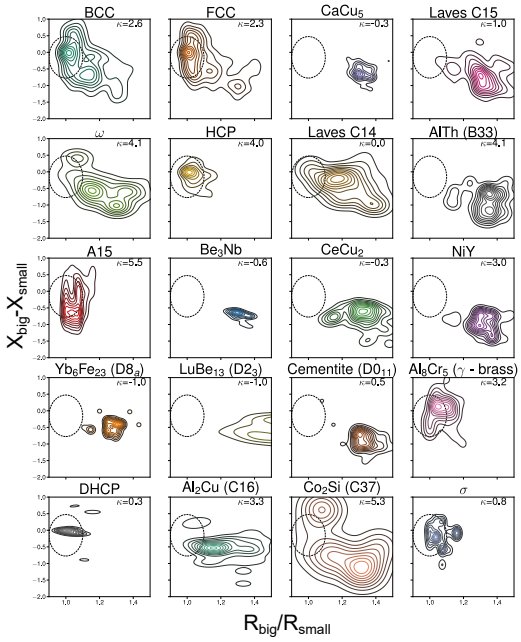

Figure A.9: Contour plots of the kernel density estimates (KDEs) of the distributions of atomic radius ratio and electronegativity difference for the top twenty parent crystals. The reference circle is for FCC.

A.5 Extending to ternary intermetallics

The framework here can be extended to ternary intermetallic categorization to elucidate effect that show up once three types of atoms interact. The hierarchy of parent crystals changes dramatically when considering ternary alloys. Many parent crystals that were fairly common in binary intermetallics are much less common in ternary intermetallics.

Figure A.28 shows a measure of the count of structures that form on the top 11 most common parent crystals for ternary intermetallics. One of notable significance is the emergence of the $InMg_2$-type crystal structure rising to the second most common parent crystal.

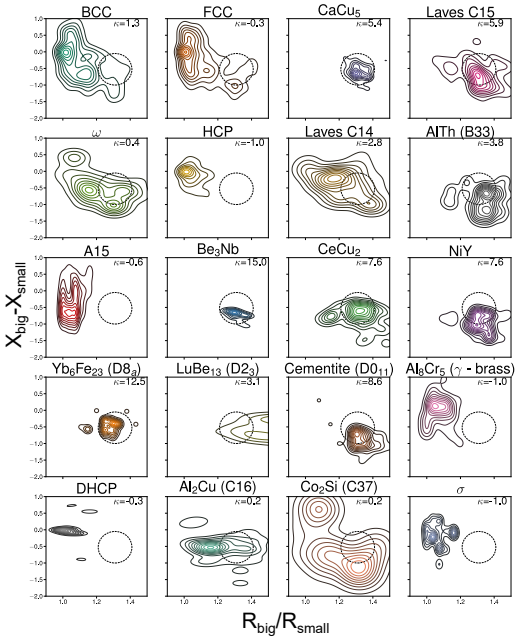

Figure A.10: Contour plots of the kernel density estimates (KDEs) of the distributions of atomic radius ratio and electronegativity difference for the top twenty parent crystals. The reference circle is for $CaCu_5$.

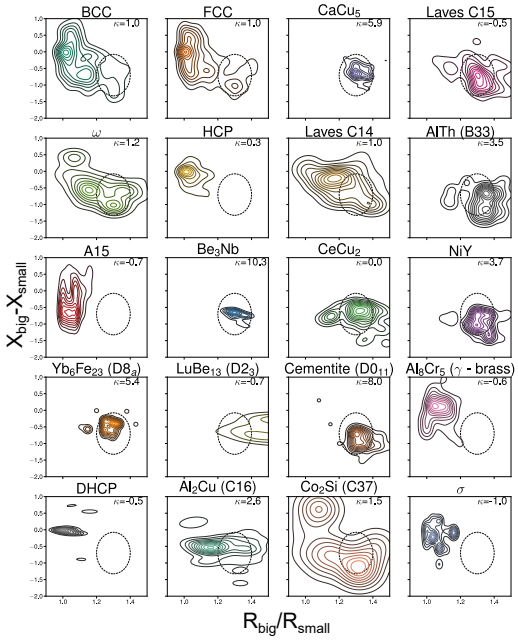

Figure A.11: Contour plots of the kernel density estimates (KDEs) of the distributions of atomic radius ratio and electronegativity difference for the top twenty parent crystals. The reference circle is for Laves C15.

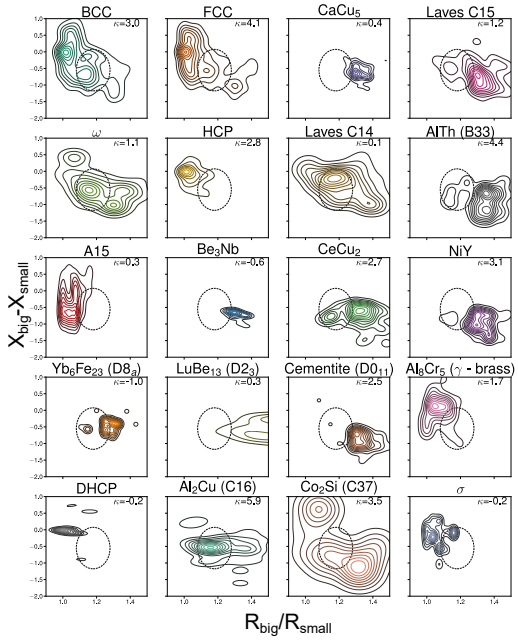

Figure A.12: Contour plots of the kernel density estimates (KDEs) of the distributions of atomic radius ratio and electronegativity difference for the top twenty parent crystals. The reference circle is for ω.

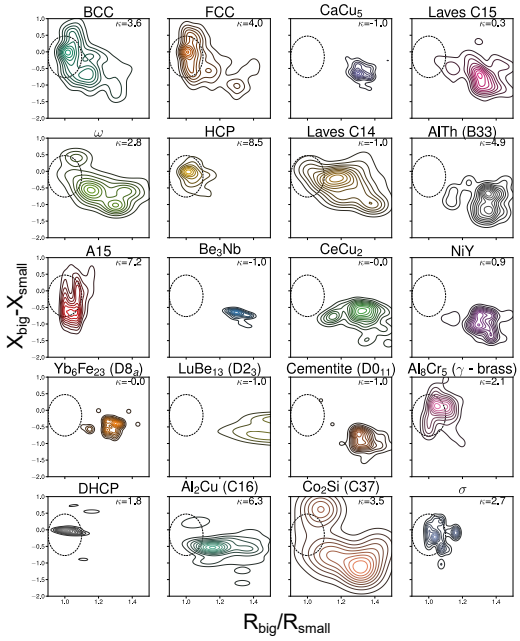

Figure A.13: Contour plots of the kernel density estimates (KDEs) of the distributions of atomic radius ratio and electronegativity difference for the top twenty parent crystals. The reference circle is for HCP.

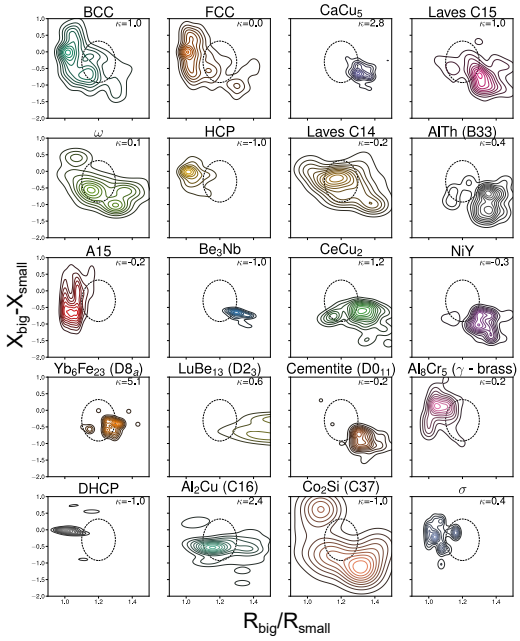

Figure A.14: Contour plots of the kernel density estimates (KDEs) of the distributions of atomic radius ratio and electronegativity difference for the top twenty parent crystals. The reference circle is for Laves C14.

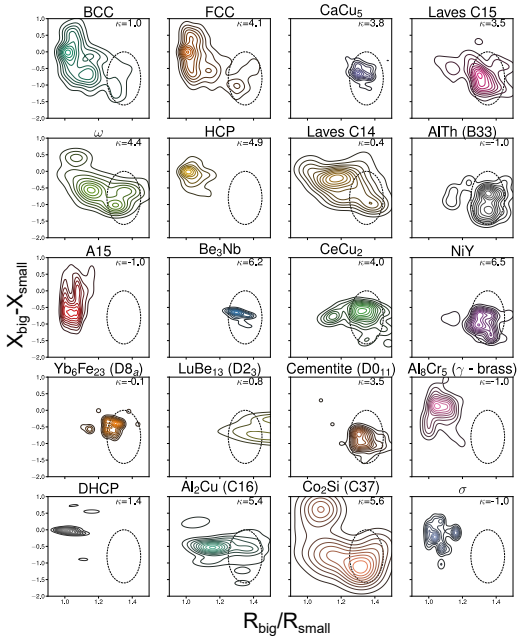

Figure A.15: Contour plots of the kernel density estimates (KDEs) of the distributions of atomic radius ratio and electronegativity difference for the top twenty parent crystals. The reference circle is for AlTh.

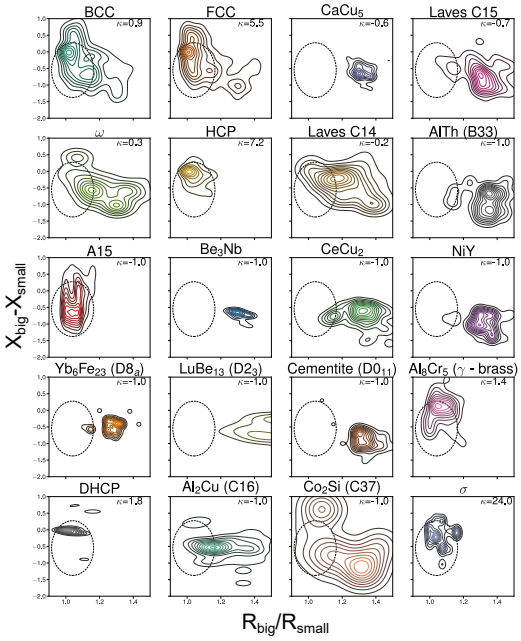

Figure A.16: Contour plots of the kernel density estimates (KDEs) of the distributions of atomic radius ratio and electronegativity difference for the top twenty parent crystals. The reference circle is for A15.

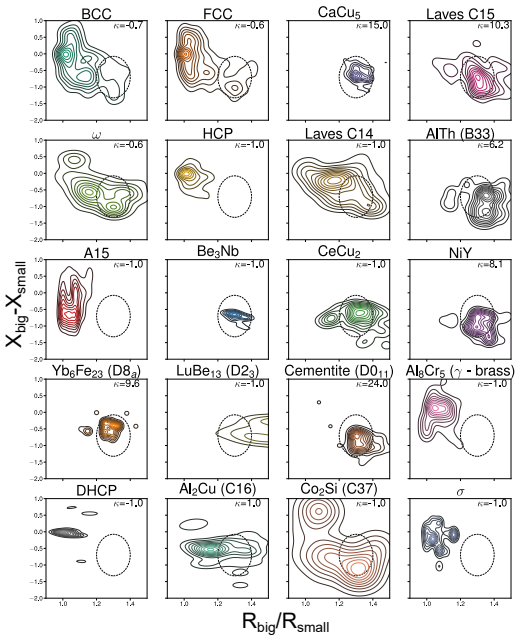

Figure A.17: Contour plots of the kernel density estimates (KDEs) of the distributions of atomic radius ratio and electronegativity difference for the top twenty parent crystals. The reference circle is for Be_3Nb.

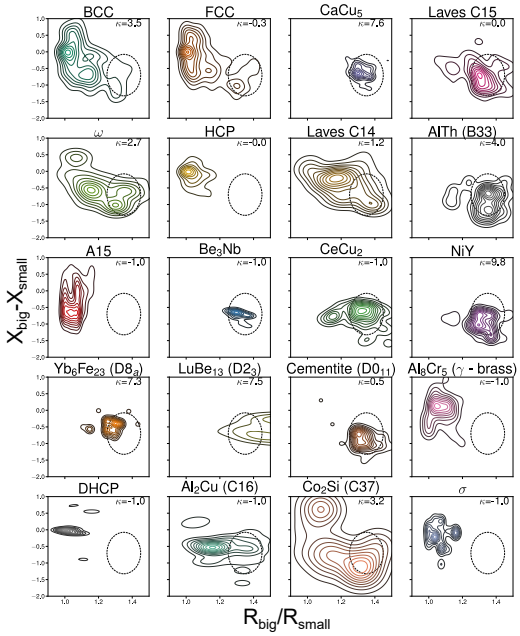

Figure A.18: Contour plots of the kernel density estimates (KDEs) of the distributions of atomic radius ratio and electronegativity difference for the top twenty parent crystals. The reference circle is for $CeCu_2$.

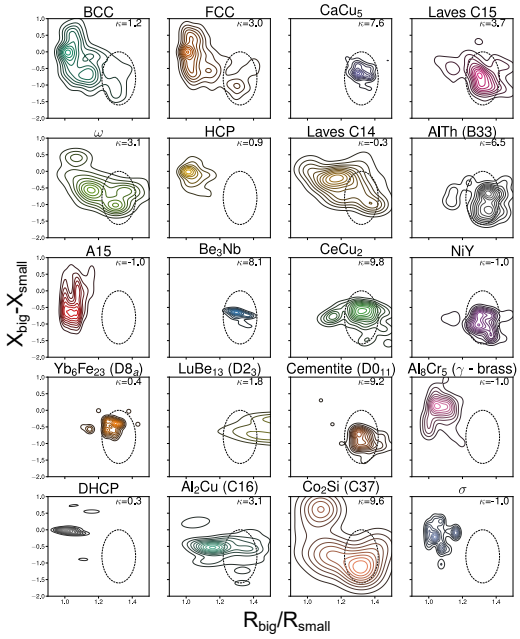

Figure A.19: Contour plots of the kernel density estimates (KDEs) of the distributions of atomic radius ratio and electronegativity difference for the top twenty parent crystals. The reference circle is for NiY.

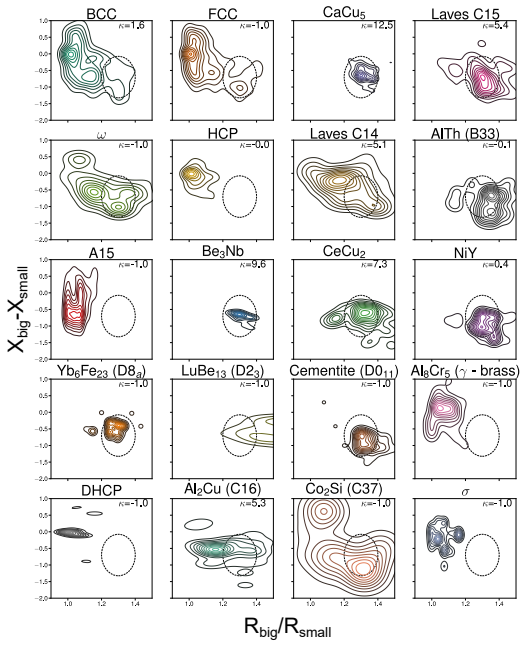

Figure A.20: Contour plots of the kernel density estimates (KDEs) of the distributions of atomic radius ratio and electronegativity difference for the top twenty parent crystals. The reference circle is for Yb_6Fe_{23}.

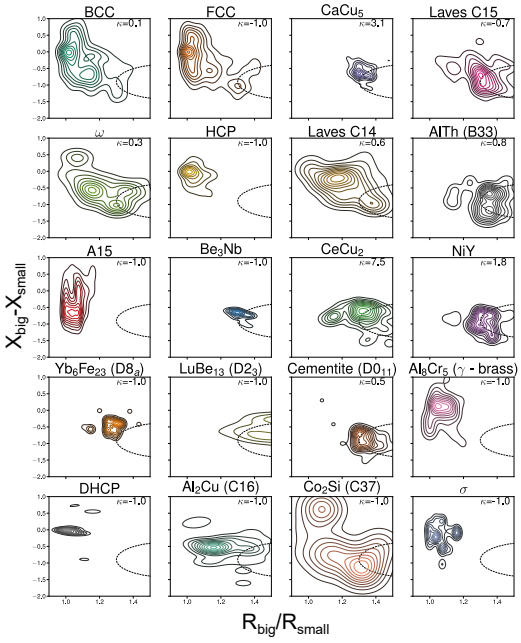

Figure A.21: Contour plots of the kernel density estimates (KDEs) of the distributions of atomic radius ratio and electronegativity difference for the top twenty parent crystals. The reference circle is for $LuBe_{13}$.

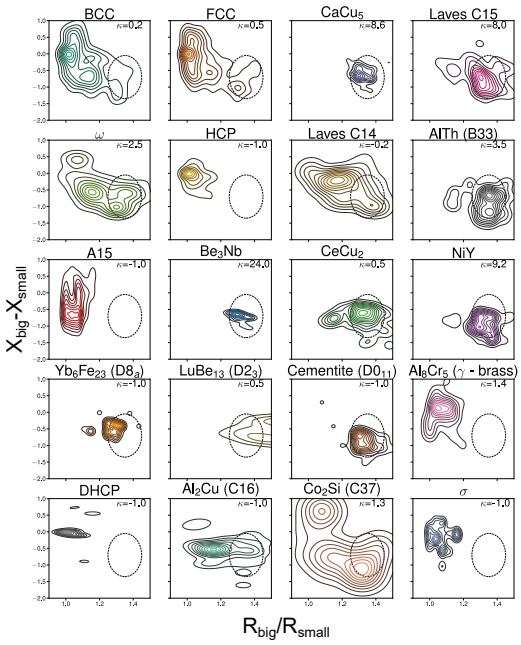

Figure A.22: Contour plots of the kernel density estimates (KDEs) of the distributions of atomic radius ratio and electronegativity difference for the top twenty parent crystals. The reference circle is for Cementite.

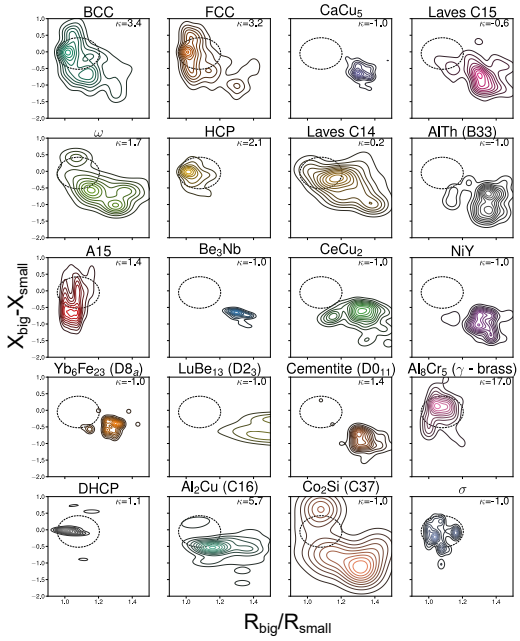

Figure A.23: Contour plots of the kernel density estimates (KDEs) of the distributions of atomic radius ratio and electronegativity difference for the top twenty parent crystals. The reference circle is for Al_8Cr_5.

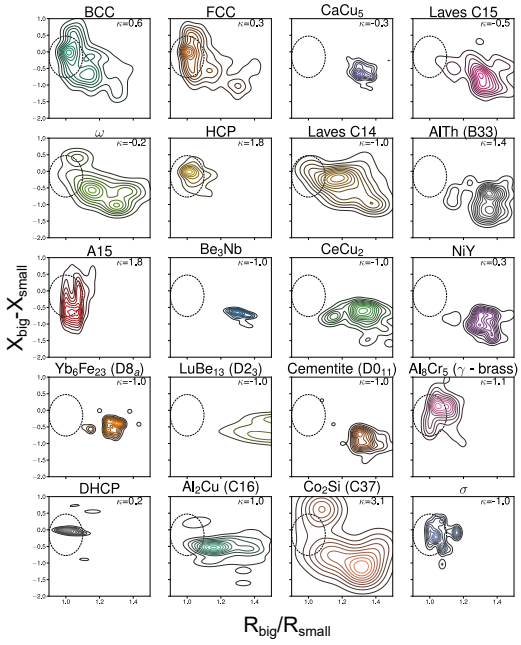

Figure A.24: Contour plots of the kernel density estimates (KDEs) of the distributions of atomic radius ratio and electronegativity difference for the top twenty parent crystals. The reference circle is for DHCP.

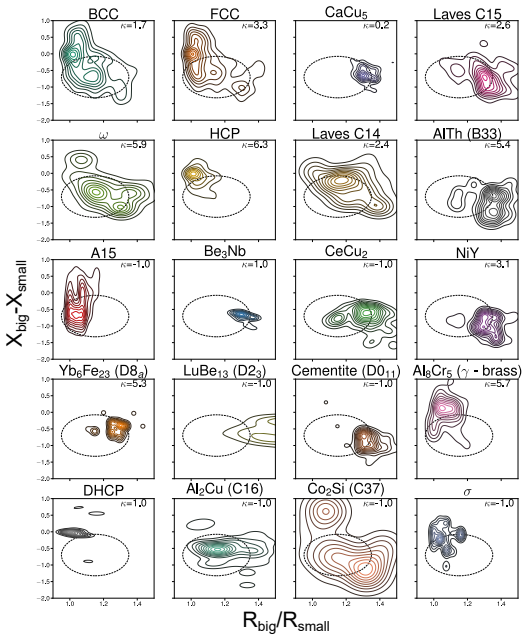

Figure A.25: Contour plots of the kernel density estimates (KDEs) of the distributions of atomic radius ratio and electronegativity difference for the top twenty parent crystals. The reference circle is for Al_2Cu.

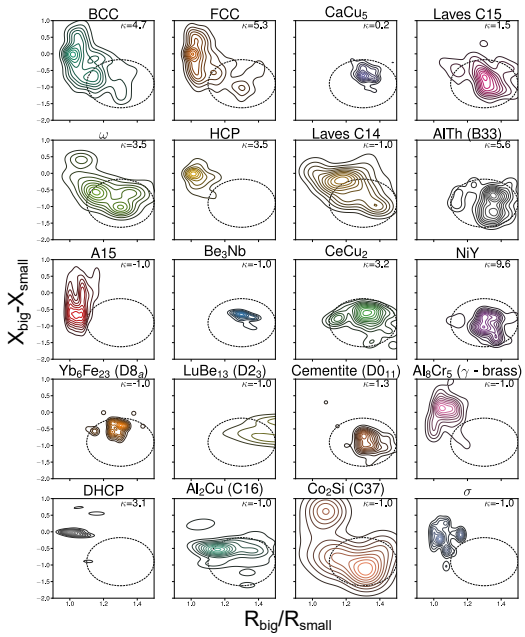

Figure A.26: Contour plots of the kernel density estimates (KDEs) of the distributions of atomic radius ratio and electronegativity difference for the top twenty parent crystals. The reference circle is for Co_2Si.

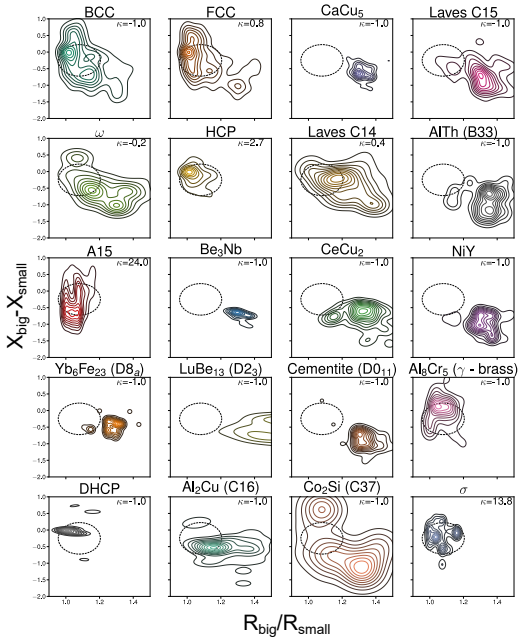

Figure A.27: Contour plots of the kernel density estimates (KDEs) of the distributions of atomic radius ratio and electronegativity difference for the top twenty parent crystals. The reference circle is for σ.

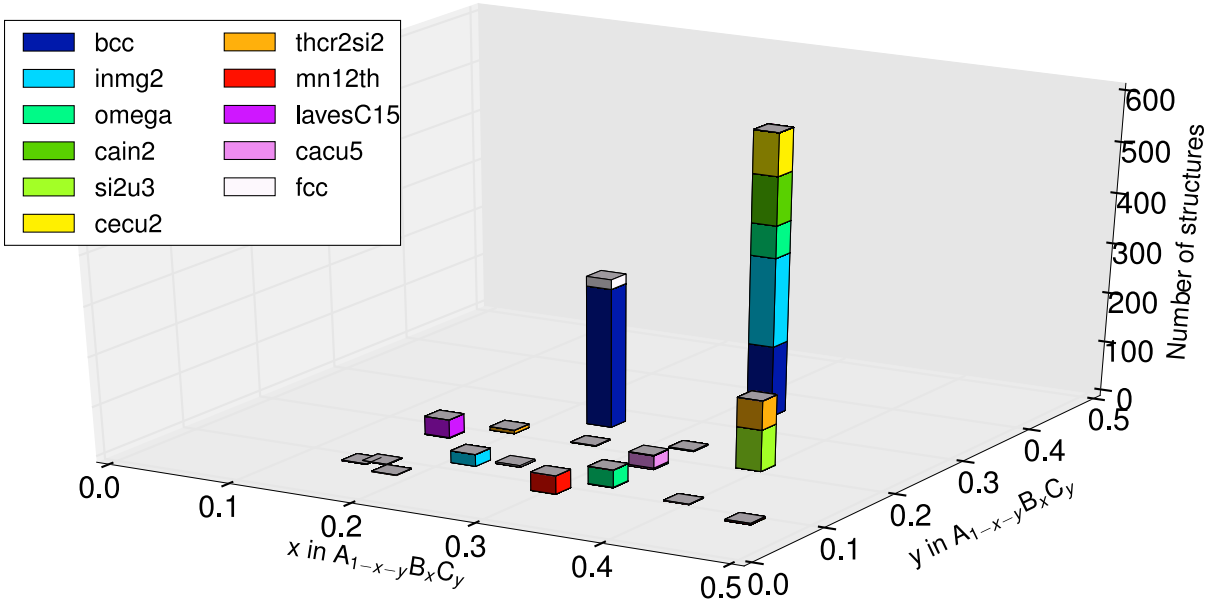

Figure A.28: The amount of structures that form on the top 11 most common parent crystals for ternary intermetallics.

Appendix B

Kinetics Appendix

B.1 Supporting Information for Chapter 6

The model cluster expansion Hamiltonian used in this study can be described by:

$$E = \sum_i V_t \sigma_i + \sum_j V_o \sigma_j + \sum_{i,j} V_{t-o} \sigma_i \sigma_j + \sum_{j,j} V_{o-o} \sigma_j \sigma_j + \sum_{i,i} V_{t-t} \sigma_i \sigma_i + \ldots \qquad \text{(B.1)}$$

The V_{o-o} and V_{t-t} term were only given non-zero values if the V_{t-o} was large enough and, in the case of V_{t-t}, V_{o-o} was non-zero. This model Hamiltonian results in 16 characteristic voltage curves if we allow Δ E_{t-o} to be 4 potential values, and V_{t-o},V_{o-o}, and V_{t-t} to 2 potential values each. Figure B.1 is a schematic decision flow chart representing the aspects of the cluster expansion that help decide the shape of each characteristic voltage curve.

The voltage curves and diffusion quantities of the octahedral rich side of Figure B.1 are shown in Figure B.2

Interestingly, if we load our model spinel systems past y=1.0, we see the correlation factor spike upwards 2 or more orders of magnitude. Figure B.3 shows the correlation

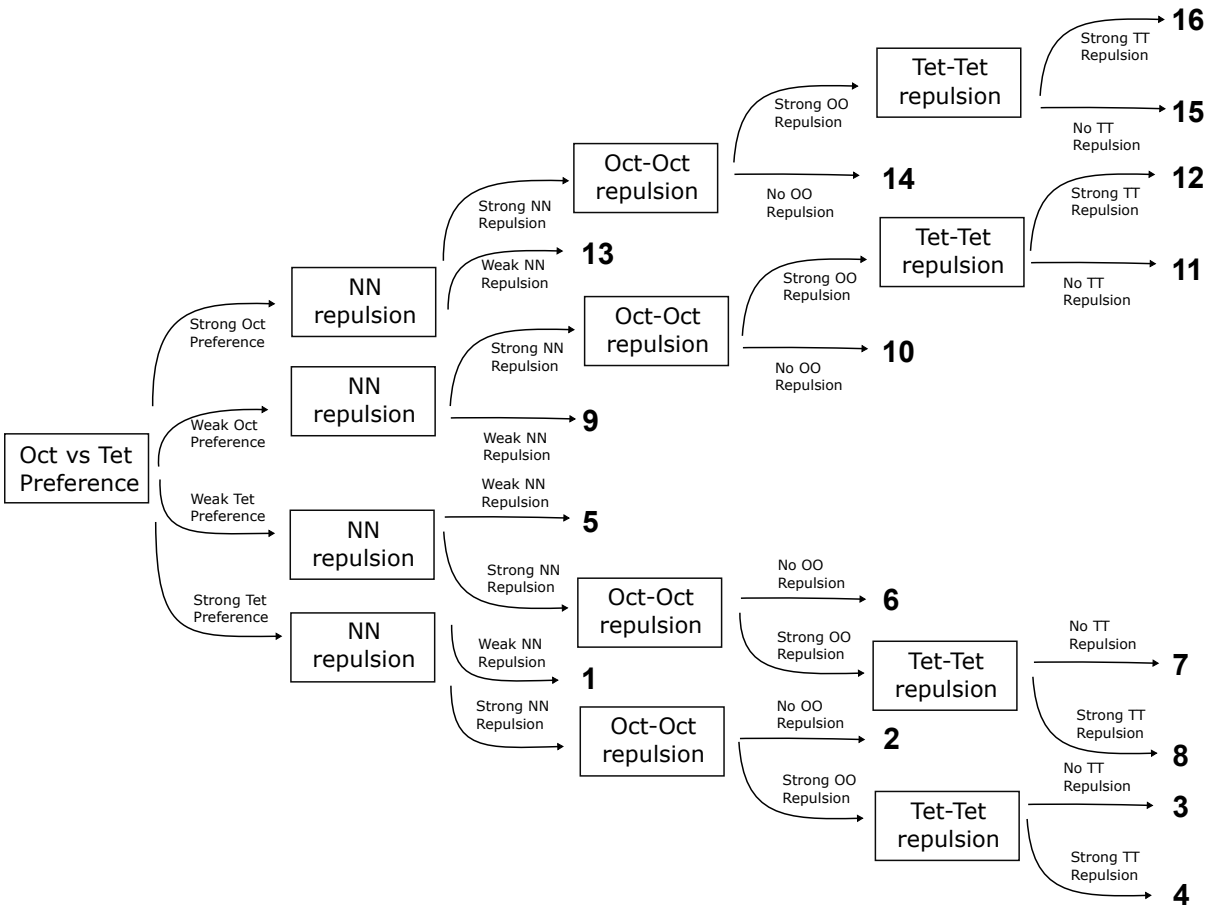

Figure B.1: The decision tree that describes the differences in the values of effective cluster interactions (ECIs) chosen in a model cluster expansion hamiltonian of the octahedral and tetrahedral interstitial sites of the spinel structure. If the empty and octahedral point cluster are fixed to 0, choosing values for the tetrahedral point cluster, the oct-tet nearest neighbor (NN) pair cluster, the oct-oct NN pair cluster, and the tet-tet NN pair cluster results in 16 different cluster expansions. We enforce that longer distance pair clusters are not activated unless all of the shorter distance interactions are activated.

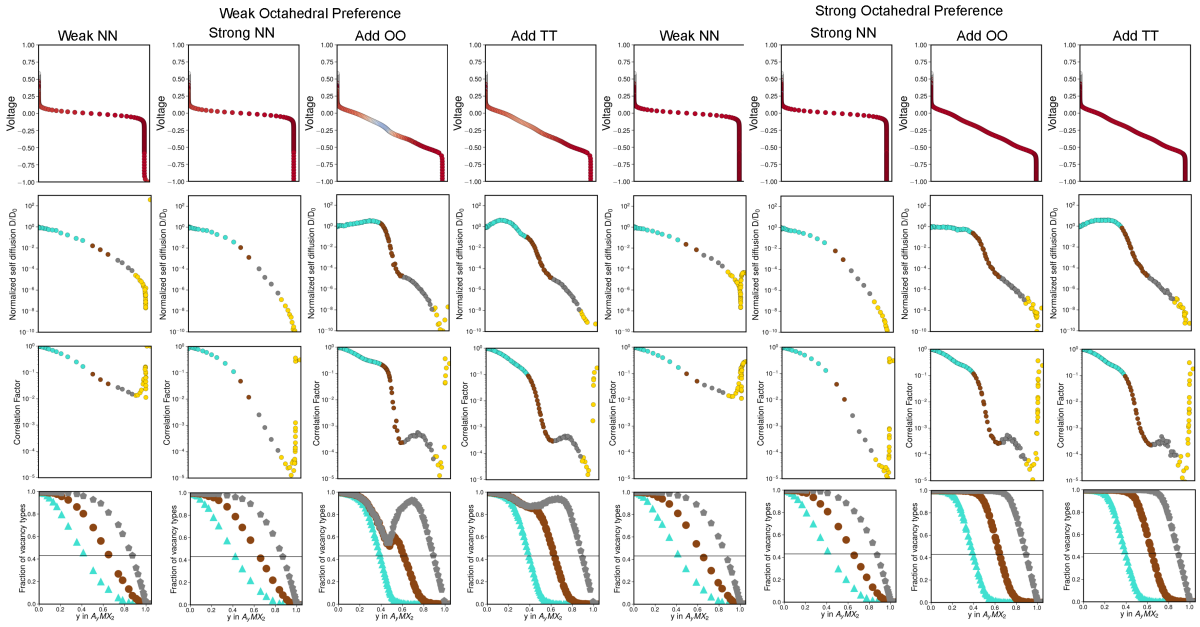

Figure B.2: The voltage curve, self diffusion coefficient, correlation factor, and vacancy fractions as a function of composition for the octahedral rich side of the flow chart in Figure B.1. Each column corresponds to condition 9-16 from Figure B.1 respectively.

factor from y=0 to y=1.5 for the section of the parameter space that slightly prefers octahedral sites. This could be caused by the levelling of the diffusion landscape beyond y=1.0. Beyond y=1.0 nearly every diffusion event has a similarly high energy barrier so backwards hops are not as likely as in a single-mechanism dominated case. The presence of a flatter energy landscape and nearest-neighbor Li-Li interactions has been shown to facilitate fast diffusion in the case of Li-based DRX electrodes [159].

B.2 Computational Methods

Density Functional Theory (DFT) as parametrized by Perdew Burke and Ernzerhof (PBE) [15] was used to calculate formation energies of Mg-vacancy orderings over the interstitial sites of spinel TiS_2. Projector augmented wave (PAW) [16, 92] theory was used to approximate the core electrons. DFT calculations were performed using the Vi-

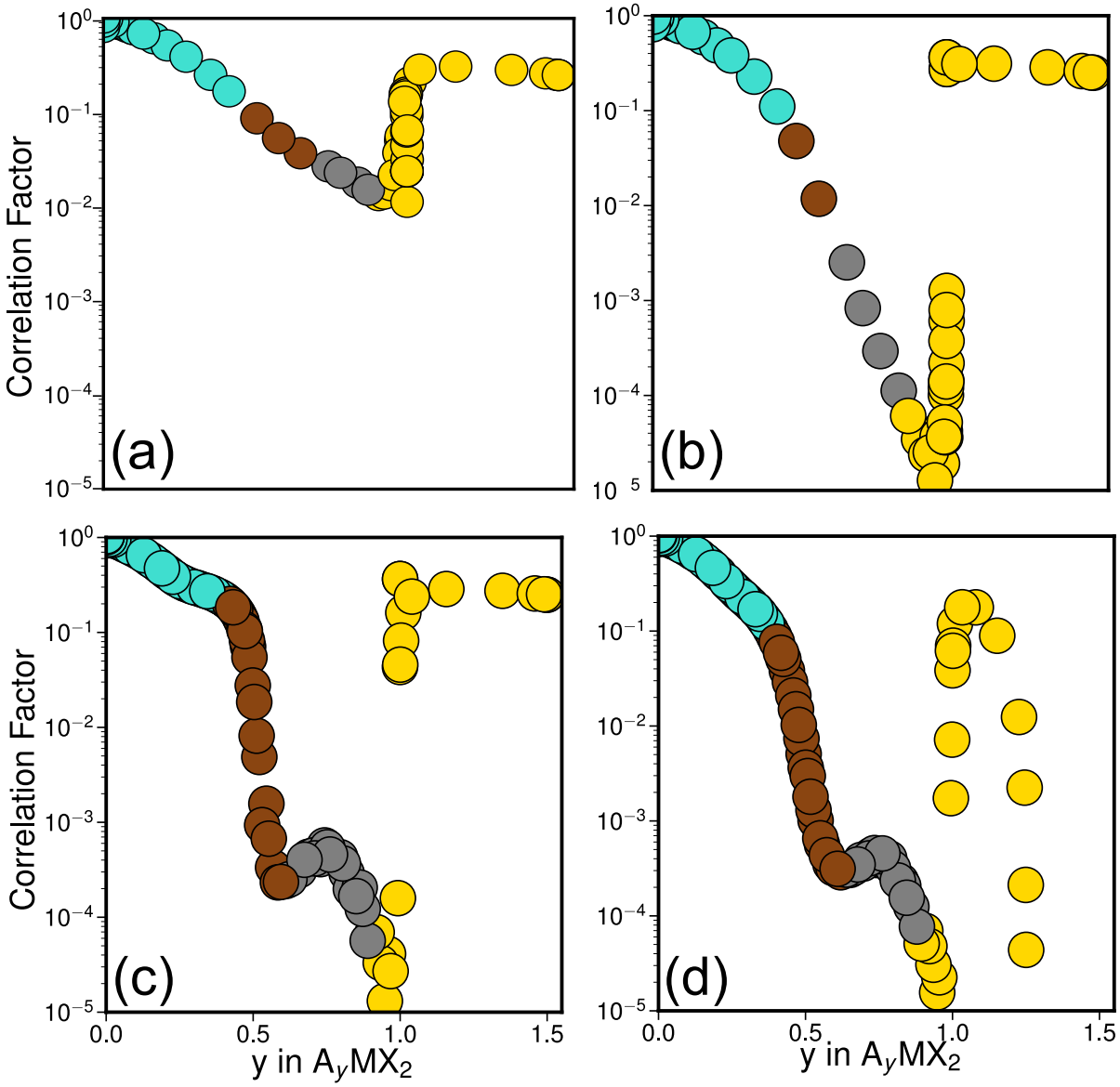

Figure B.3: The correlation factor for conditions 9-12 in Figure B.1. The NN is increased from (a) to (b). The E_{OO} interaction is added in (c), and the E_{TT} interaction is added in (d). Points are colored based on the type of vacancy above the percolation threshold. In all cases, the correlation factor rises dramatically at y=1.

enna ab-initio software package (VASP) [14, 13]. Plane-wave cutoff energies of 450 were used for calculations with a k-point density of 32 Å. Formation energies of Mg-vacancy configurations over the tetrahedral and octahedral sites of spinel TiS_2 were used to train cluster expansion Hamiltonians [17, 114] to predict the energy of arbitrary configurations within spinel TiS_2. The cluster expansion Hamiltonians were used in grand canonical and kinetic Monte Carlo simulations to calculate room temperature electrochemical properties, including open circuit voltage profiles, equilibrium site occupancies, diffusion coefficients and correlation factors. The Clusters Approach to Statistical Mechanics (CASM) software package was used to construct and parametrize the cluster expansions and to perform the grand canonical and kinetic Monte Carlo simulations. Kinetic Monte Carlo simulations were run using a fixed kinetically-resolved activation (KRA) barrier of 0.5 eV for the Mg_yTiS_2 spinel and 0.3 eV for the model Hamiltonians. These KRA barrier heights were chosen by examining the calculated barrier heights of isolated Mg^{2+} ions moving in a 2x2x2 supercell of the primitive spinel-TiS_2 cell. These barriers are shown in Figure B.4.

The vibrational prefactor for determining hop frequency was 5 x 10^{12}. The values for the effective cluster interactions (ECIs) for the model Hamiltonians were ΔE_{t-o}=[-0.1875,-0.0625,0.0625,0.1875],V_{t-o}=[0.25,0.75],V_{o-o}=[0,0.0833], and V_{t-t}=[0,0.125]. These values were chosen to probe small changes in energetics. The kinetic properties that are most relevant in this study are the Onsager transport coefficients, self-diffusion coefficients and the correlation factor. The methods to calculate these quantities are shown in Chapter 2.

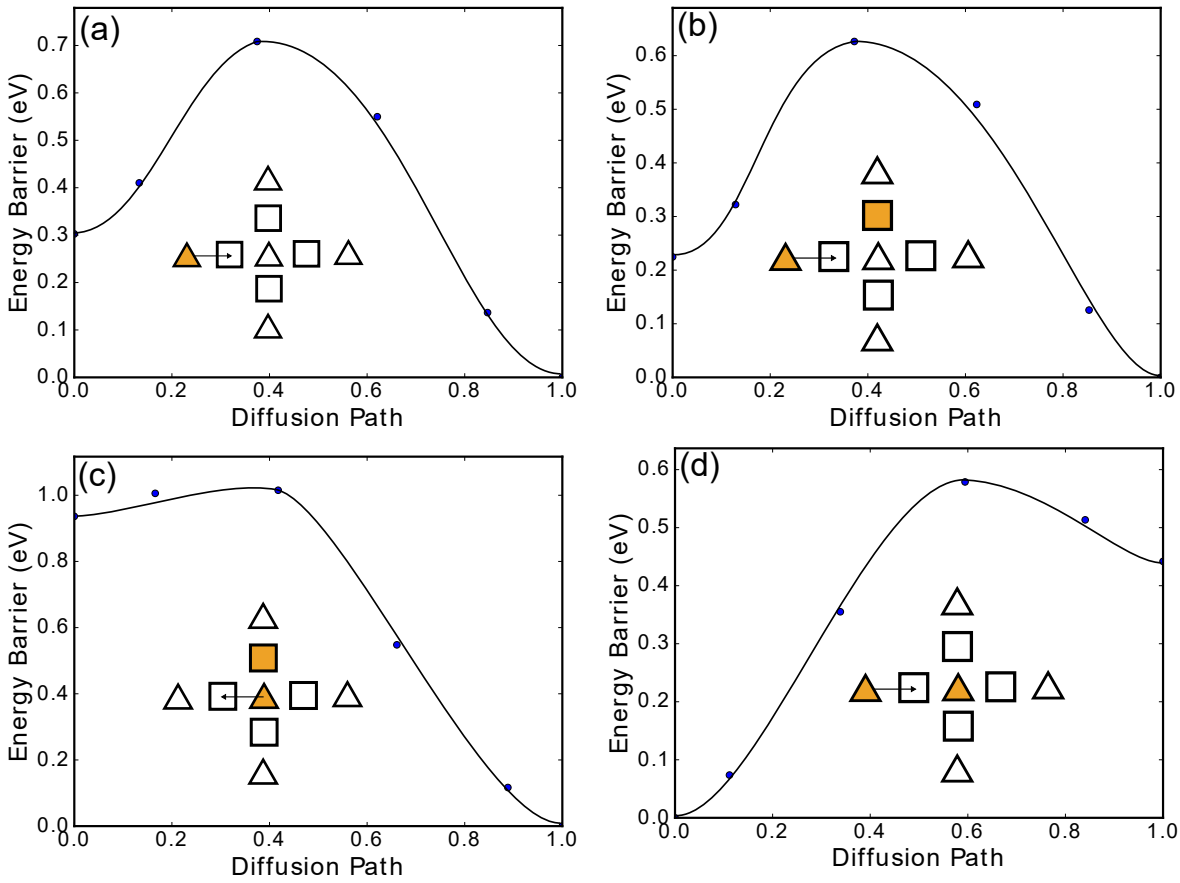

Figure B.4: Diffusion barriers calculated via nudged elastic band (NEB) methods for an (a) octahedral triple vacancy hop with out an octahedral neighbor, (b) an octahedral triple vacancy hop with a neighbor, (c) an octahedral divacancy hop, and a (d) tetrahedral hop into a blocked channel in the dilute limit. The kinetically-resolved activation barriers are 0.557, 0.514, 0.547, and 0.358 eV. respectively. Local environments around a tetrahedral site can be mapped from 3D to 2D schematics as seen in Figure B.5. These schematics are shown in each barrier plot to illustrate the local environment.

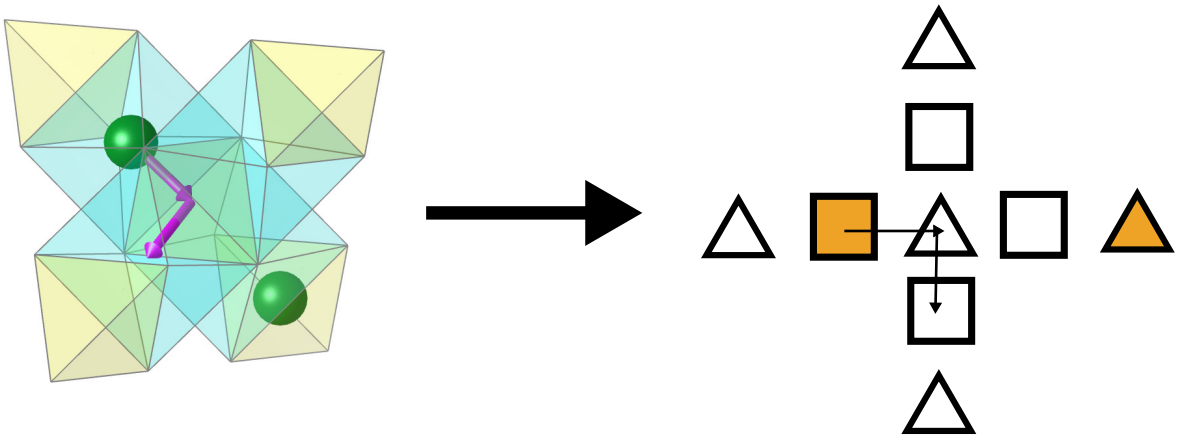

Figure B.5: A comparison of the environment surrounding a tetrahedral interstitial site in spinel in 3D to a 2D schematic of the environment. Tetrahedral sites are drawn as triangles and octahedral sites are drawn as squares.

Bibliography

[1] T. M. Pollock and A. Van Der Ven, *The evolving landscape for alloy design*, *MRS Bulletin* **44** (apr, 2019) 238–246.

[2] R. Allmann and R. Hinek, *The introduction of structure types into the Inorganic Crystal Structure Database ICSD*, *Acta Crystallographica Section A Foundations of Crystallography* **63** (Sept., 2007) 412–417.

[3] A. Jain, S. P. Ong, G. Hautier, W. Chen, W. D. Richards, S. Dacek, S. Cholia, D. Gunter, D. Skinner, and K. a. Ceder, Gerbrand an d Persson, *The Materials Project: A materials genome approach to accelerating materials innovation*, *APL Materials* **1** (2013), no. 1 011002.

[4] J. B. Goodenough and K.-S. Park, *The li-ion rechargeable battery: A perspective*, *Journal of the American Chemical Society* **135** (2013), no. 4 1167–1176, [https://doi.org/10.1021/ja3091438]. PMID: 23294028.

[5] N. Nitta, F. Wu, J. T. Lee, and G. Yushin, *Li-ion battery materials: present and future*, *Materials Today* **18** (2015), no. 5 252–264.

[6] M. D. Radin, S. Hy, M. Sina, C. Fang, H. Liu, J. Vinckeviciute, M. Zhang, M. S. Whittingham, Y. S. Meng, and A. Van der Ven, *Narrowing the gap between theoretical and practical capacities in li-ion layered oxide cathode materials*, *Advanced Energy Materials* jul 1602888.

[7] Z. Lun, B. Ouyang, D. H. Kwon, Y. Ha, E. E. Foley, T. Y. Huang, Z. Cai, H. Kim, M. Balasubramanian, Y. Sun, J. Huang, Y. Tian, H. Kim, B. D. McCloskey, W. Yang, R. J. Clément, H. Ji, and G. Ceder, *Cation-disordered rocksalt-type high-entropy cathodes for Li-ion batteries*, *Nature Materials* **20** (feb, 2021) 214–221.

[8] R. Clément, Z. Lun, and G. Ceder, *Cation-disordered rocksalt transition metal oxides and oxyfluorides for high energy lithium-ion cathodes*, *Energy & Environmental Science* **13** (2020), no. 2 345–373.

[9] H. Ji, A. Urban, D. A. Kitchaev, D.-H. Kwon, N. Artrith, C. Ophus, W. Huang, Z. Cai, T. Shi, J. C. Kim, *et. al.*, *Hidden structural and chemical order controls*

lithium transport in cation-disordered oxides for rechargeable batteries, *Nature communications* **10** (2019), no. 1 1–9.

[10] H. Ji, J. Wu, Z. Cai, J. Liu, D. H. Kwon, H. Kim, A. Urban, J. K. Papp, E. Foley, Y. Tian, M. Balasubramanian, H. Kim, R. J. Clément, B. D. McCloskey, W. Yang, and G. Ceder, *Ultrahigh power and energy density in partially ordered lithium-ion cathode materials*, *Nature Energy* **5** (mar, 2020) 213–221.

[11] H. Liu, Z. Zhu, Q. Yan, S. Yu, X. He, Y. Chen, R. Zhang, L. Ma, T. Liu, M. Li, *et. al.*, *A disordered rock salt anode for fast-charging lithium-ion batteries*, *Nature* **585** (2020), no. 7823 63–67.

[12] J. Lee, A. Urban, X. Li, D. Su, G. Hautier, and G. Ceder, *Unlocking the potential of cation-disordered oxides for rechargeable lithium batteries*, *science* **343** (2014), no. 6170 519–522.

[13] G. Kresse and J. Furthmüller, *Efficiency of ab-initio total energy calculations for metals and semiconductors using a plane-wave basis set*, *Computational Materials Science* jul 15–50.

[14] G. Kresse and J. Furthmüller, *Efficient iterative schemes for\italicsab Initio total-energy calculations using a plane-wave basis set*, *Physical Review B* oct 11169–11186.

[15] J. P. Perdew, K. Burke, and M. Ernzerhof, *Generalized gradient approximation made simple*, *Physical Review Letters* oct 3865–3868.

[16] P. E. Blöchl, *Projector augmented-wave method*, *Physical Review B* dec 17953–17979.

[17] J. Sanchez, F. Ducastelle, and D. Gratias, *Generalized cluster description of multicomponent systems*, *Physica A: Statistical Mechanics and its Applications* nov 334–350.

[18] D. D. Fontaine, *Cluster Approach to Order-Disorder Transformations in Alloys*, *Solid State Physics - Advances in Research and Applications* **47** (jan, 1994) 33–176.

[19] R. Gomer, *Diffusion of adsorbates on metal surfaces*, *Reports on Progress in Physics* **53** (jul, 1990) 917–1002.

[20] A. R. Allnatt and E. L. Allnatt, *Computer simulation of phenomenological coefficients for atom transport in a random alloy*, *Philosophical Magazine A* **49** (1984), no. 5 625–635, [https://doi.org/10.1080/01418618408233291].

[21] G. Murch, *Some tracer correlation factors in the f.c.c. lattice†*, *Journal of Physics and Chemistry of Solids* **45** (1984), no. 4 451–452.

[22] R. W. Balluffi, S. M. Allen, and W. C. Carter, *Kinetics of materials*. John Wiley & Sons, 2005.

[23] D. Trinkle, R. Hennig, S. Srinivasan, D. Hatch, M. Jones, H. Stokes, R. Albers, and J. Wilkins, *New mechanism for the α to ω martensitic transformation in pure titanium*, *Physical review letters* **91** (2003), no. 2 025701.

[24] H. W. Kuhn, *The Hungarian method for the assignment problem*, *Naval Research Logistics Quarterly* **2** (mar, 1955) 83–97.

[25] H. W. Kuhn, *Variants of the hungarian method for assignment problems*, *Naval Research Logistics Quarterly* **3** (dec, 1956) 253–258.

[26] S. K. Kolli, A. R. Natarajan, J. C. Thomas, T. M. Pollock, and A. Van der Ven, *Discovering hierarchies among intermetallic crystal structures*, *Physical Review Materials* **4** (2020), no. 11 113604.

[27] A. Van De Walle and M. Asta, *High-throughput calculations in the context of alloy design*, *MRS Bulletin* **44** (apr, 2019) 252–256.

[28] R. Arróyave and D. L. McDowell, *Systems approaches to materials design: past, present, and future*, *Annual Review of Materials Research* **49** (2019) 103–126.

[29] A. Abu-Odeh, E. Galvan, T. Kirk, H. Mao, Q. Chen, P. Mason, R. Malak, and R. Arróyave, *Efficient exploration of the high entropy alloy composition-phase space*, *Acta Materialia* **152** (2018) 41–57.

[30] M. Asta, V. Ozolins, and C. Woodward, *A first-principles approach to modeling alloy phase equilibria*, *JOM* **53** (2001), no. 9 16–19.

[31] A. Van de Walle and G. Ceder, *The effect of lattice vibrations on substitutional alloy thermodynamics*, *Reviews of Modern Physics* **74** (jan, 2002) 11–45, [0106490].

[32] A. van de Walle and M. Asta, *Self-driven lattice-model monte carlo simulations of alloy thermodynamic properties and phase diagrams*, *Modelling and Simulation in Materials Science and Engineering* **10** (2002), no. 5 521.

[33] D. Alfè, *PHON: A program to calculate phonons using the small displacement method*, *Computer Physics Communications* **180** (dec, 2009) 2622–2633.

[34] A. Van De Walle, *Methods for first-principles alloy thermodynamics*, *JOM* **65** (nov, 2013) 1523–1532.

[35] B. Puchala and A. Van der Ven, *Thermodynamics of the zr-o system from first-principles calculations*, *Physical Review B* sep 094108.

[36] J. C. Thomas and A. Van Der Ven, *Finite-temperature properties of strongly anharmonic and mechanically unstable crystal phases from first principles*, *Physical Review B* dec 214111.

[37] R. K. Rhein, P. C. Dodge, M.-H. Chen, M. S. Titus, T. M. Pollock, and A. Van Der Ven, *Role of vibrational and configurational excitations in stabilizing the L1 2 structure in Co-rich Co-Al-W alloys*, *PHYSICAL REVIEW B* **92** (2015) 174117.

[38] K. Lejaeghere, G. Bihlmayer, T. Björkman, P. Blaha, S. Blügel, V. Blum, D. Caliste, I. E. Castelli, S. J. Clark, A. Dal Corso, *et. al.*, *Reproducibility in density functional theory calculations of solids*, *Science* **351** (2016), no. 6280.

[39] A. Van der Ven, J. Thomas, B. Puchala, and A. Natarajan, *First-principles statistical mechanics of multicomponent crystals*, *Annual Review of Materials Research* jul 27–55.

[40] D. De Fontaine, *k-space symmetry rules for order-disorder reactions*, *Acta Metallurgica* **23** (1975), no. 5 553–571.

[41] A. Khachaturian, *Ordering in substitutional and interstitial solid solutions*, *Progress in Materials Science* (1978).

[42] D. de Fontaine, *Configurational Thermodynamics of Solid Solutions*, *Solid State Physics - Advances in Research and Applications* **34** (jan, 1979) 73–274.

[43] T. Mohri, J. Sanchez, and D. De Fontaine, *Overview no. 43: Binary ordering prototype phase diagrams in the cluster variation approximation*, *Acta Metallurgica* **33** (1985), no. 7 1171–1185.

[44] F. Ducastelle and F. Ducastelle, *Order and phase stability in alloys*, .

[45] G. Inden, *Atomic Ordering*, in *Materials Science and Technology*. Wiley-VCH Verlag GmbH & Co. KGaA, Weinheim, Germany, feb, 2013.

[46] A. G. Khachaturyan, *Theory of structural transformations in solids*. Courier Corporation, 2013.

[47] G. L. Hart and R. W. Forcade, *Generating derivative structures from multilattices: Algorithm and application to hcp alloys*, *Physical Review B* **80** (2009), no. 1 014120.

[48] J. M. Sanchez, F. Ducastelle, and D. Gratias, *Generalized cluster description of multicomponent systems*, *Physica A: Statistical Mechanics and its Applications* **128** (1984), no. 1-2 334–350.

[49] A. R. Natarajan, J. C. Thomas, B. Puchala, and A. Van der Ven, *Symmetry-adapted order parameters and free energies for solids undergoing order-disorder phase transitions*, *Physical Review B* **96** (2017), no. 13 134204.

[50] J. C. Thomas and A. Van der Ven, *Order parameters for symmetry-breaking structural transitions: The tetragonal-monoclinic transition in zro 2*, *Physical Review B* **96** (2017), no. 13 134121.

[51] J. C. Thomas and A. Van der Ven, *The exploration of nonlinear elasticity and its efficient parameterization for crystalline materials*, *Journal of the Mechanics and Physics of Solids* **107** (2017) 76–95.

[52] G. H. Teichert, A. Natarajan, A. Van der Ven, and K. Garikipati, *Machine learning materials physics: Integrable deep neural networks enable scale bridging by learning free energy functions*, *Computer Methods in Applied Mechanics and Engineering* **353** (2019) 201–216.

[53] S. Curtarolo, W. Setyawan, G. L. Hart, M. Jahnatek, R. V. Chepulskii, R. H. Taylor, S. Wang, J. Xue, K. Yang, O. Levy, *et. al.*, *Aflow: an automatic framework for high-throughput materials discovery*, *Computational Materials Science* **58** (2012) 218–226.

[54] J. E. Saal, S. Kirklin, M. Aykol, B. Meredig, and C. Wolverton, *Materials design and discovery with high-throughput density functional theory: The open quantum materials database (OQMD)*, *JOM* **65** (nov, 2013) 1501–1509.

[55] W. Ye, C. Chen, S. Dwaraknath, A. Jain, S. P. Ong, and K. A. Persson, *Harnessing the Materials Project for machine-learning and accelerated discovery*, *MRS Bulletin* **43** (sep, 2018) 664–669.

[56] L. Gelato and E. Parthé, *Structure tidy–a computer program to standardize crystal structure data*, *Journal of Applied Crystallography* **20** (1987), no. 2 139–143.

[57] H. Burzlaff and Y. Malinovsky, *A procedure for the clasification of non-organic crystal structures. i. theoretical background*, *Acta Crystallographica Section A: Foundations of Crystallography* **53** (1997), no. 2 217–224.

[58] A. Dzyabchenko, *Method of crystal-structure similarity searching*, *Acta Crystallographica Section B: Structural Science* **50** (1994), no. 4 414–425.

[59] G. Flor, D. Orobengoa, E. Tasci, J. M. Perez-Mato, and M. I. Aroyo, *Comparison of structures applying the tools available at the bilbao crystallographic server*, *Journal of Applied Crystallography* **49** (2016), no. 2 653–664.

[60] E. Willighagen, R. Wehrens, P. Verwer, R. De Gelder, and L. Buydens, *Method for the computational comparison of crystal structures*, *Acta Crystallographica Section B: Structural Science* **61** (2005), no. 1 29–36.

[61] R. Hundt, J. Schön, and M. Jansen, *Cmpz–an algorithm for the efficient comparison of periodic structures*, *Journal of applied crystallography* **39** (2006), no. 1 6–16.

[62] D. C. Lonie and E. Zurek, *Identifying duplicate crystal structures: Xtalcomp, an open-source solution*, *Computer Physics Communications* **183** (2012), no. 3 690–697.

[63] D. Zagorac, H. Müller, S. Ruehl, J. Zagorac, and S. Rehme, *Recent developments in the Inorganic Crystal Structure Database: Theoretical crystal structure data and related features*, *Journal of Applied Crystallography* **52** (Oct., 2019) 918–925.

[64] S. K. Kolli, *Intermetallic parent and derivative crystal structures*, *https://sites.engineering.ucsb.edu/ skolli/* (2020).

[65] D. Miracle, *Overview no. 104 the physical and mechanical properties of nial*, *Acta metallurgica et materialia* **41** (1993), no. 3 649–684.

[66] J. G. Goiri and A. Van Der Ven, *Phase and structural stability in Ni-Al systems from first principles*, *Physical Review B* **94** (sep, 2016) 094111.

[67] M. J. Murray and J. V. Sanders, *Close-packed structures of spheres of two different sizes II. The packing densities of likely arrangements*, *Philosophical Magazine A: Physics of Condensed Matter, Structure, Defects and Mechanical Properties* **42** (1980), no. 6 721–740.

[68] A. R. Natarajan and A. Van der Ven, *Connecting the Simpler Structures to Topologically Close-Packed Phases*, *Physical Review Letters* **121** (2018) 255701.

[69] C. Developers, *Casmcode: V0.3.0*, .

[70] T. B. Massalski, H. H. Okamoto, and ASM International., *Binary alloy phase diagrams*. ASM International, 1990.

[71] S. M. Allen and J. W. Cahn, *A microscopic theory for antiphase boundary motion and its application to antiphase domain coarsening*, *Acta Metallurgica* **27** (jun, 1979) 1085–1095.

[72] G. Teichert, A. Natarajan, A. Van der Ven, and K. Garikipati, *Scale bridging materials physics: Active learning workflows and integrable deep neural networks for free energy function representations in alloys*, *Computer Methods in Applied Mechanics and Engineering* **371** (2020) 113281.

[73] N. H. Gunda and A. Van der Ven, *First-principles insights on phase stability of titanium interstitial alloys*, *Physical Review Materials* **2** (2018), no. 8 083602.

[74] U. Mizutani, *The hume-rothery rules for structurally complex alloy phases*, in *Surface Properties And Engineering Of Complex Intermetallics*, pp. 323–399. World Scientific, 2010.

[75] N. H. Gunda, B. Puchala, and A. Van der Ven, *Resolving phase stability in the ti-o binary with first-principles statistical mechanics methods*, *Physical Review Materials* **2** (2018), no. 3 033604.

[76] T. M. Pollock, *Weight loss with magnesium alloys*, *Science* **328** (2010), no. 5981 986–987, [https://science.sciencemag.org/content/328/5981/986.full.pdf].

[77] X. Huang, G. J. Ackland, and K. M. Rabe, *Crystal structures and shape-memory behaviour of niti*, *Nature materials* **2** (2003), no. 5 307–311.

[78] Y. Ogawa, D. Ando, Y. Sutou, and J. Koike, *A lightweight shape-memory magnesium alloy*, *Science* **353** (2016), no. 6297 368–370, [https://science.sciencemag.org/content/353/6297/368.full.pdf].

[79] B. Dutta, A. Çak ır, C. Giacobbe, A. Al-Zubi, T. Hickel, M. Acet, and J. Neugebauer, *Ab initio prediction of martensitic and intermartensitic phase boundaries in ni-mn-ga*, *Phys. Rev. Lett.* **116** (Jan, 2016) 025503.

[80] B. Cabane, J. Li, F. Artzner, R. Botet, C. Labbez, G. Bareigts, M. Sztucki, and L. Goehring, *Hiding in Plain View: Colloidal Self-Assembly from Polydisperse Populations*, *Physical Review Letters* **116** (May, 2016).

[81] E. C. Bain and N. Dunkirk, *The nature of martensite*, *trans. AIME* **70** (1924), no. 1 25–47.

[82] W. Burgers, , *Physica1* (1934) 561.

[83] D. R. Trinkle, R. G. Hennig, S. G. Srinivasan, D. M. Hatch, M. D. Jones, H. T. Stokes, R. C. Albers, and J. W. Wilkins, *New mechanism for the α to ω martensitic transformation in pure titanium*, *Phys. Rev. Lett.* **91** (Jul, 2003) 025701.

[84] A. R. Natarajan and A. Van der Ven, *Connecting the simpler structures to topologically close-packed phases*, *Phys. Rev. Lett.* **121** (Dec, 2018) 255701.

[85] A.-P. Hynninen, L. Filion, and M. Dijkstra, *Stability of ls and ls 2 crystal structures in binary mixtures of hard and charged spheres*, *The Journal of chemical physics* **131** (2009), no. 6 064902.

[86] F. Laves, *Kristallographie der Legierungen*, *Die Naturwissenschaften* **27** (feb, 1939) 65–73.

[87] C. Wolverton and V. Ozoliņš, *Entropically favored ordering: The metallurgy of* al_2Cu *revisited*, *Phys. Rev. Lett.* **86** (Jun, 2001) 5518–5521.

[88] X. Meng and D. O. Northwood, *Second phase particles in zircaloy-2*, *Journal of Nuclear Materials* **168** (1989), no. 1 125–136.

[89] P. Chemelle, D. Knorr, J. Van Der Sande, and R. Pelloux, *Morphology and composition of second phase particles in zircaloy-2*, *Journal of Nuclear Materials* **113** (1983), no. 1 58–64.

[90] S. Kirklin, J. E. Saal, B. Meredig, A. Thompson, J. W. Doak, M. Aykol, S. Rühl, and C. Wolverton, *The open quantum materials database (oqmd): assessing the accuracy of dft formation energies*, *npj Computational Materials* **1** (2015), no. 1 1–15.

[91] J. E. Saal, S. Kirklin, M. Aykol, B. Meredig, and C. Wolverton, *Materials design and discovery with high-throughput density functional theory: the open quantum materials database (oqmd)*, *Jom* **65** (2013), no. 11 1501–1509.

[92] G. Kresse and D. Joubert, *From ultrasoft pseudopotentials to the projector augmented-wave method*, *Physical Review B* jan 1758.

[93] S. K. Kolli and A. Van Der Ven, *Controlling the Electrochemical Properties of Spinel Intercalation Compounds*, *ACS Applied Energy Materials* **1** (dec, 2018) 6833–6839.

[94] M. S. Whittingham, *Lithium batteries and cathode materials*, *Chem. Rev.* no. 10 4271–4302.

[95] M. Thackeray, W. David, P. Bruce, and J. Goodenough, *Lithium insertion into manganese spinels*, *Materials Research Bulletin* apr 461–472.

[96] M. Thackeray, P. Johnson, L. de Picciotto, P. Bruce, and J. Goodenough, *Electrochemical extraction of lithium from* $limn_2o_4$, *Materials Research Bulletin* feb 179–187.

[97] M. M. Thackeray, *Manganese oxides for lithium batteries*, *Progress in Solid State Chemistry* jan 1–71.

[98] J. M. Tarascon, E. Wang, F. K. Shokoohi, W. R. McKinnon, and S. Colson, *The spinel phase of* $limn_2o_4$ *as a cathode in secondary lithium cells*, *Journal of The Electrochemical Society* oct 2859.

[99] T. Ohzuku, A. Ueda, and N. Yamamoto, *Zero-strain insertion material of* $li[li_{13}ti_{53}]o_4$ *for rechargeable lithium cells*, *Journal of The Electrochemical Society* may 1431.

[100] T.-F. Yi, L.-J. Jiang, J. Shu, C.-B. Yue, R.-S. Zhu, and H.-B. Qiao, *Recent development and application of $li_4ti_5o_{12}$ as anode material of lithium ion battery*, *Journal of Physics and Chemistry of Solids* sep 1236–1242.

[101] A. S. Prakash, P. Manikandan, K. Ramesha, M. Sathiya, J.-M. Tarascon, and A. K. Shukla, *Solution-combustion synthesized nanocrystalline li_4ti_5 o_{12} as high-rate performance li-ion battery anode*, *Chemistry of Materials* may 2857–2863.

[102] B. Zhao, R. Ran, M. Liu, and Z. Shao, *A comprehensive review of $li_4ti_5o_{12}$-based electrodes for lithium-ion batteries: The latest advancements and future perspectives*, *Materials Science and Engineering: R: Reports* dec 1–71.

[103] X. Sun, P. Bonnick, V. Duffort, M. Liu, Z. Rong, K. A. Persson, G. Ceder, and L. F. Nazar, *A high capacity thiospinel cathode for mg batteries*, *Energy Environ. Sci.* jul 2273–2277.

[104] N. Yabuuchi, M. Yano, S. Kuze, and S. Komaba, *Electrochemical behavior and structural change of spinel-type $li[li_xmn_{2x}]o_4$ ($x = 0$ and 0.2) in sodium cells*, *Electrochimica Acta* nov 296–301.

[105] J. R. Kim and G. G. Amatucci, *Structural and electrochemical investigation of na^+ insertion into high-voltage spinel electrodes*, *Chemistry of Materials* apr 2546–2556.

[106] J. Tarascon, D. Guyomard, B. Wilkens, W. Mc Kinnon, and P. Barboux, *Chemical and electrochemical insertion of na into the spinel λ-mno_2 phase*, *Solid State Ionics* sep 113–120.

[107] G. T.-K. Fey, C.-Z. Lu, and T. Kumar, *Preparation and electrochemical properties of high-voltage cathode materials, $lim_yni_{0.5y}mn_{1.5}o_4$ (m=fe, cu, al, mg; y=0.0–0.4)*, *Journal of Power Sources* apr 332–345.

[108] M. Liu, Z. Rong, R. Malik, P. Canepa, A. Jain, G. Ceder, and K. A. Persson, *Spinel compounds as multivalent battery cathodes: A systematic evaluation based on ab initio calculations*, *Energy & Environmental Science* mar 964–974.

[109] J. Bhattacharya and A. Van der Ven, *Phase stability and nondilute li diffusion in spinel li $_{1+X}$ ti $_2$ o_4*, *Physical Review B* mar 104304.

[110] M. Wagemaker, A. Van Der Ven, D. Morgan, G. Ceder, F. Mulder, and G. Kearley, *Thermodynamics of spinel lixtio2 from first principles*, *Chemical Physics* oct 130–136.

[111] J. Bhattacharya and A. Van der Ven, *First-principles study of competing mechanisms of nondilute li diffusion in spinel li $_x$ tis $_2$*, *Physical Review B* apr 144302.

[112] T. Chen, G. Sai Gautam, W. Huang, and G. Ceder, *First-principles study of the voltage profile and mobility of mg intercalation in a chromium oxide spinel*, *Chemistry of Materials* jan 153–162.

[113] S. K. Kolli and A. Van der Ven, *First-principles study of spinel mgtis$_2$as a cathode material*, *Chemistry of Materials* apr 2436–2442.

[114] D. DeFontaine, *Cluster approach to order-disorder transformations in alloys*, *Solid State Physics* jan 33–176.

[115] A. Van der Ven, J. Bhattacharya, and A. A. Belak, *Understanding li diffusion in li-intercalation compounds*, *Accounts of Chemical Research* may 1216–1225.

[116] A. Emly and A. Van der Ven, *Mg intercalation in layered and spinel host crystal structures for mg batteries*, *Inorganic Chemistry* may 4394–4402.

[117] L. Ahrens, *The use of ionization potentials part 1. ionic radii of the elements*, *Geochimica et Cosmochimica Acta* jan 155–169.

[118] P. Bonnick, X. Sun, K.-C. Lau, C. Liao, and L. F. Nazar, *Monovalent versus divalent cation diffusion in thiospinel ti$_2$s$_4$*, *The Journal of Physical Chemistry Letters* may 2253–2257.

[119] K. Kim, A. Arora, R. M. Lewis, M. Liu, W. Li, A.-C. Shi, K. D. Dorfman, and F. S. Bates, *Origins of low-symmetry phases in asymmetric diblock copolymer melts*, *Proceedings of the National Academy of Sciences* **115** (Jan., 2018) 847–854.

[120] M. D. Radin and A. Van der Ven, *Simulating charge, spin, and orbital ordering: Application to jahn–teller distortions in layered transition-metal oxides*, *Chemistry of Materials* feb 607–618.

[121] M. S. Whittingham, *Electrical energy storage and intercalation chemistry*, *Science* **192** (1976), no. 4244 1126–1127.

[122] K. Mizushima, P. Jones, P. Wiseman, and J. B. Goodenough, *Lixcoo2 (0¡ x¡-1): A new cathode material for batteries of high energy density*, *Materials Research Bulletin* **15** (1980), no. 6 783–789.

[123] J. Goodenough, M. Thackeray, W. David, and P. Bruce, *Lithium insertion into manganese spinels*, *Mater. Res. Bull* **18** (1983) 461–472.

[124] M. Thackeray, P. Johnson, L. De Picciotto, P. Bruce, and J. Goodenough, *Electrochemical extraction of lithium from limn2o4*, *Materials Research Bulletin* **19** (1984), no. 2 179–187.

[125] J. Dahn, *Phase diagram of li x c 6*, *Physical Review B* **44** (1991), no. 17 9170.

[126] J. Tarascon, E. Wang, F. Shokoohi, W. McKinnon, and S. Colson, *The spinel phase of limn2 o 4 as a cathode in secondary lithium cells*, *Journal of the Electrochemical Society* **138** (1991), no. 10 2859.

[127] J. Tarascon and D. Guyomard, *The li1+ xmn2o4/c rocking-chair system: a review*, *Electrochimica Acta* **38** (1993), no. 9 1221–1231.

[128] M. S. Whittingham, *Lithium batteries and cathode materials*, *Chemical reviews* **104** (2004), no. 10 4271–4302.

[129] C. Delmas, J.-J. Braconnier, C. Fouassier, and P. Hagenmuller, *Electrochemical intercalation of sodium in naxcoo2 bronzes*, *Solid State Ionics* **3** (1981) 165–169.

[130] N. Yabuuchi, K. Kubota, M. Dahbi, and S. Komaba, *Research development on sodium-ion batteries*, *Chemical reviews* **114** (2014), no. 23 11636–11682.

[131] C. Delmas, *Sodium and sodium-ion batteries: 50 years of research*, *Advanced Energy Materials* **8** (2018), no. 17 1703137.

[132] H. Kim, J. C. Kim, M. Bianchini, D.-H. Seo, J. Rodriguez-Garcia, and G. Ceder, *Recent progress and perspective in electrode materials for k-ion batteries*, *Advanced Energy Materials* **8** (2018), no. 9 1702384.

[133] T. Hosaka, K. Kubota, A. S. Hameed, and S. Komaba, *Research development on k-ion batteries*, *Chemical reviews* **120** (2020), no. 14 6358–6466.

[134] H. D. Yoo, I. Shterenberg, Y. Gofer, G. Gershinsky, N. Pour, and D. Aurbach, *Mg rechargeable batteries: an on-going challenge*, *Energy & Environmental Science* **6** (2013), no. 8 2265–2279.

[135] P. Canepa, G. Sai Gautam, D. C. Hannah, R. Malik, M. Liu, K. G. Gallagher, K. A. Persson, and G. Ceder, *Odyssey of multivalent cathode materials: open questions and future challenges*, *Chemical reviews* **117** (2017), no. 5 4287–4341.

[136] A. Van der Ven, Z. Deng, S. Banerjee, and S. P. Ong, *Rechargeable alkali-ion battery materials: theory and computation*, *Chemical reviews* **120** (2020), no. 14 6977–7019.

[137] A. Van der Ven, J. Bhattacharya, and A. A. Belak, *Understanding li diffusion in li-intercalation compounds*, *Accounts of Chemical Research* **46** (2013), no. 5 1216–1225, [https://doi.org/10.1021/ar200329r]. PMID: 22584006.

[138] M. D. Radin, S. Hy, M. Sina, C. Fang, H. Liu, J. Vinckeviciute, M. Zhang, M. S. Whittingham, Y. S. Meng, and A. Van der Ven, *Narrowing the gap between theoretical and practical capacities in li-ion layered oxide cathode materials*, *Advanced Energy Materials* **7** (2017), no. 20 1602888.

[139] A. Manthiram, K. Chemelewski, and E.-S. Lee, *A perspective on the high-voltage limn 1.5 ni 0.5 o 4 spinel cathode for lithium-ion batteries*, *Energy & Environmental Science* **7** (2014), no. 4 1339–1350.

[140] N. Yabuuchi, M. Takeuchi, M. Nakayama, H. Shiiba, M. Ogawa, K. Nakayama, T. Ohta, D. Endo, T. Ozaki, T. Inamasu, K. Sato, and S. Komaba, *High-capacity electrode materials for rechargeable lithium batteries: Li3nbo4-based system with cation-disordered rocksalt structure*, *Proceedings of the National Academy of Sciences* **112** (2015), no. 25 7650–7655, [https://www.pnas.org/content/112/25/7650.full.pdf].

[141] J. Lee, D.-H. Seo, M. Balasubramanian, N. Twu, X. Li, and G. Ceder, *A new class of high capacity cation-disordered oxides for rechargeable lithium batteries: Li–ni–ti–mo oxides*, *Energy Environ. Sci.* **8** (2015) 3255–3265.

[142] M. A. Jones, P. J. Reeves, I. D. Seymour, M. J. Cliffe, S. E. Dutton, and C. P. Grey, *Short-range ordering in a battery electrode, the 'cation-disordered' rocksalt li1.25nb0.25mn0.5o2*, *Chem. Commun.* **55** (2019) 9027–9030.

[143] A. Van der Ven and G. Ceder, *Lithium diffusion mechanisms in layered intercalation compounds*, *Journal of power sources* **97** (2001) 529–531.

[144] A. Van der Ven, G. Ceder, M. Asta, and P. Tepesch, *First-principles theory of ionic diffusion with nondilute carriers*, *Physical Review B* **64** (2001), no. 18 184307.

[145] A. Urban, J. Lee, and G. Ceder, *The configurational space of rocksalt-type oxides for high-capacity lithium battery electrodes*, *Advanced Energy Materials* **4** (2014), no. 13 1400478.

[146] X. Sun, P. Bonnick, and L. F. Nazar, *Layered tis2 positive electrode for mg batteries*, *ACS Energy Letters* **1** (2016), no. 1 297–301.

[147] X. Sun, P. Bonnick, V. Duffort, M. Liu, Z. Rong, K. A. Persson, G. Ceder, and L. F. Nazar, *A high capacity thiospinel cathode for mg batteries*, *Energy & Environmental Science* **9** (2016), no. 7 2273–2277.

[148] A. Emly and A. Van der Ven, *Mg intercalation in layered and spinel host crystal structures for mg batteries*, *Inorganic chemistry* **54** (2015), no. 9 4394–4402.

[149] S. K. Kolli and A. Van der Ven, *First-principles study of spinel mgtis2 as a cathode material*, *Chemistry of Materials* **30** (2018), no. 7 2436–2442.

[150] A. Van der Ven and G. Ceder, *First principles calculation of the interdiffusion coefficient in binary alloys*, *Physical review letters* **94** (2005), no. 4 045901.

[151] A. Van der Ven, J. C. Thomas, B. Puchala, and A. R. Natarajan, *First-principles statistical mechanics of multicomponent crystals*, *Annual Review of Materials Research* **48** (2018) 27–55.

[152] J. G. Goiri, S. K. Kolli, and A. Van der Ven, *Role of short- and long-range ordering on diffusion in ni-al alloys*, *Phys. Rev. Materials* **3** (Sep, 2019) 093402.

[153] A. Van der Ven, J. C. Thomas, Q. Xu, B. Swoboda, and D. Morgan, *Nondilute diffusion from first principles: Li diffusion in li x tis 2*, *Physical Review B* **78** (2008), no. 10 104306.

[154] A. Van der Ven, H.-C. Yu, G. Ceder, and K. Thornton, *Vacancy mediated substitutional diffusion in binary crystalline solids*, *Progress in Materials Science* **55** (2010), no. 2 61–105.

[155] M. D. Radin and A. Van der Ven, *Stability of prismatic and octahedral coordination in layered oxides and sulfides intercalated with alkali and alkaline-earth metals*, *Chemistry of Materials* **28** (2016), no. 21 7898–7904.

[156] S. C. van der Marck, *Percolation thresholds and universal formulas*, *Physical Review E - Statistical Physics, Plasmas, Fluids, and Related Interdisciplinary Topics* **55** (feb, 1997) 1514–1517.

[157] F. Frank and J. S. Kasper, *Complex alloy structures regarded as sphere packings. I. Definitions and basic principles*, *Acta Crystallographica* **11** (1958), no. 3 184–190.

[158] F. C. Frank and J. S. Kasper, *Complex alloy structures regarded as sphere packings. II. Analysis and classification of representative structures*, *Acta Crystallographica* **12** (jul, 1959) 483–499.

[159] W. Zhang, D.-H. Seo, T. Chen, L. Wu, M. Topsakal, Y. Zhu, D. Lu, G. Ceder, and F. Wang, *Kinetic pathways of ionic transport in fast-charging lithium titanate*, *Science* **367** (2020), no. 6481 1030–1034, [https://science.sciencemag.org/content/367/6481/1030.full.pdf].